# Autonomous Underwater Vehicle Altitude Keeping to Variable Seabed with a Coupled Variable Ballast and Hydroplane Control System

by

Jesse David

Submitted in partial fulfilment of the requirements
for the degree of Master of Applied Science

at

Dalhousie University
Halifax, Nova Scotia
August 2016

# Table of Contents

# List of Tables

# Abstract

The objective of this thesis is to develop a PID control approach that enables variable ballast systems (VBS) to be used in tandem with hydroplanes (HP) on an autonomous underwater vehicle (AUV). Methods to help reduce the power consumption of VBS are investigated and a AUV computer simulator is developed to explore scenarios where VBS might prove beneficial.

The VBS simulation model includes the capacity for free flow of seawater into and out of the ballast tank. This function combined with the capacity to provide high pressure air support allowed for the exploration of four VBS control modes: static volume, expanded volume, high-pressure air assist and regenerative pressure assisted. For the simulation conditions tested in this research, the regenerative pressure assisted mode required, on average, the least amount of power. This control mode permitted free emptying at higher depths and also returned air back into the charge air tank and ultimately reduced the energy required to operate the pump.

When using pitch and depth feedback as inputs to the HP and VBS PID controllers, the hydroplanes responded before the VBS could react making the VBS ineffective. A new control approach was, therefore, developed that uses HP deflection angle feedback as inputs to the VBS in combination with a low-pass filter. The resulting simulations showed that this control approach performed favorably in multiple scenarios.

# List of Abbreviations and Symbols Used

**Coordinate System**

| | |
|---|---|
| $\eta$ | Position/Attitude Vector of the AUV in the global reference frame |
| x, y, z | Position components of $\eta$ in x, y and z directions |
| $\varphi$, $\theta$, $\psi$ | Rotation component of $\eta$ about x, y and z axes |
| $\nu$ | Velocity Vector of the AUV in the global reference frame |
| u, v, w | Translational Velocity components of $\nu$ in x, y and z directions |
| p, q, r | Rotational Velocity components of $\nu$ about x, y and axes |
| $\tau$ | Vector of applied Forces and Moments of the AUV in the body fixed reference frame |
| X, Y, Z | Force applied in x, y and z directions to the AUV in the body fixed reference frame |
| K, M, N | Moment applied about x, y and z axes to the AUV in the body fixed reference frame |

**AUV Variables**

| | |
|---|---|
| M | Mass and Moments of system |
| C($\nu$) | Coriolis and centripetal terms |
| D($\nu$) | Damping due to hydrodynamic forces |

| | |
|---|---|
| $g(\eta)$ | Hydrostatic forces due to gravity |
| $I_x$, $I_y$, $I_z$ | Moment of Inertia about x, y and z axes |
| | |
| $m_{auv}$ | Mass of the AUV |
| $r_{auv}$ | Radius of AUV hull |
| $L_{auv}$ | Length of AUV from nose to propeller |
| | |
| $F_{am}$ | Added Mass Force |
| $A_x$ | Added Mass in x direction |
| $A_y$ | Added Mass in y direction |
| $A_z$ | Added Mass in z direction |
| | |
| $\rho_{sw}$ | Density of Sea Water |
| $F_g$ | Force of Gravity |
| $F_\Delta$ | Displacement Force |
| $F_L$ | Hydroplane Lift Force |
| $C_{Dx}$, $C_{Dy}$, $C_{Dz}$ | Coefficient of Drag in x, y and z directions |
| $C_{Lhf}$ | Hydroplane Coefficient of Lift |

**Hydroplane Variables**

| | |
|---|---|
| $\alpha$ | Hydroplane Deflection Angle |
| $\alpha_f$ | Fore Hydroplane Deflection Angle |
| $\alpha_{a1}$, $\alpha_{a2}$ | Aft Hydroplane Deflection Angles |
| $\alpha_\theta$ | Heading Deflection Angle Command |
| $\alpha_\psi$ | Pitch Deflection Angle Command |
| $\alpha_y$ | Depth Deflection Angle Command |

**VBS Variables**

| | |
|---|---|
| $Q_p$ | Pump flow (L/min) |
| $Q_{p100}$ | Maximum pump flow (L/min) |
| $\eta_v$ | Pump volumetric efficiency |
| $P_a$ | VBS Tank ① Air Pressure (kPa) |
| $P_c$ | VBS Tank ⑧ Air Pressure (kPa) |
| $P_{sw}$ | Sea Water Pressure (kPa) |
| $m_a$ | Mass of air in VBS Tank |
| $m_c$ | Mass of air in Charge Tank |
| $m_w$ | Mass of water in VBS Tank |
| $V_t$ | Volume of VBS Tank |
| $V_w$ | Volume of Water in VBS Tank |
| $V_c$ | Volume of Charge Tank |
| $\rho_a$ | Density of air in VBS Tank |
| $\rho_c$ | Density of air in Charge Tank |
| | |
| $f_{vbsf}$ | Net Buoyancy Force of Fore Tank |
| $f_{vbsa}$ | Net Buoyancy Force of Aft Tank |
| $l_{fb}$ | Position of Fore VBS along x axis |
| $l_{ab}$ | Position of Aft VBS along x axis |

**Abbreviations**

| | |
|---|---|
| 3D | Three Dimensions |
| AUV | Autonomous Underwater Vehicle |
| CoB | Center of Buoyancy |
| CoG | Center of Gravity |
| HP | Hydroplane |
| ISE | International Submarine Engineering Ltd |
| NACA | National Advisory Committee for Aeronautics |
| PID | Proportion, Integral, Differential Controller |
| ROV | Remotely Operated Vehicle |
| SMC | Sliding Mode Controller |
| VBS | Variable Ballast System |
| | |
| NF | No Flow |
| FF | Free Flow |
| P+ | Pumping into Tank |
| P- | Pumping out of Tank |
| | |
| NA | Null Air |
| VA | Vent Air |
| CA | Charge Air |
| RA | Regen Air |

# Chapter 1: Introduction

An autonomous underwater vehicle (AUV) is a submersible vehicle much like submarines and remotely operated vehicles (ROV). All vehicles described as submersible operate primarily below the water's surface; however, AUVs are distinct in this category in that they are:

- **Unmanned**: Thus they do not need to include the extra measures to ensure the safety of the on-board human operators.
- **Autonomous**: They have no tether.

One example of an AUV is the International Submarine Engineering (ISE) Arctic Explorer shown in Figure 1.1.

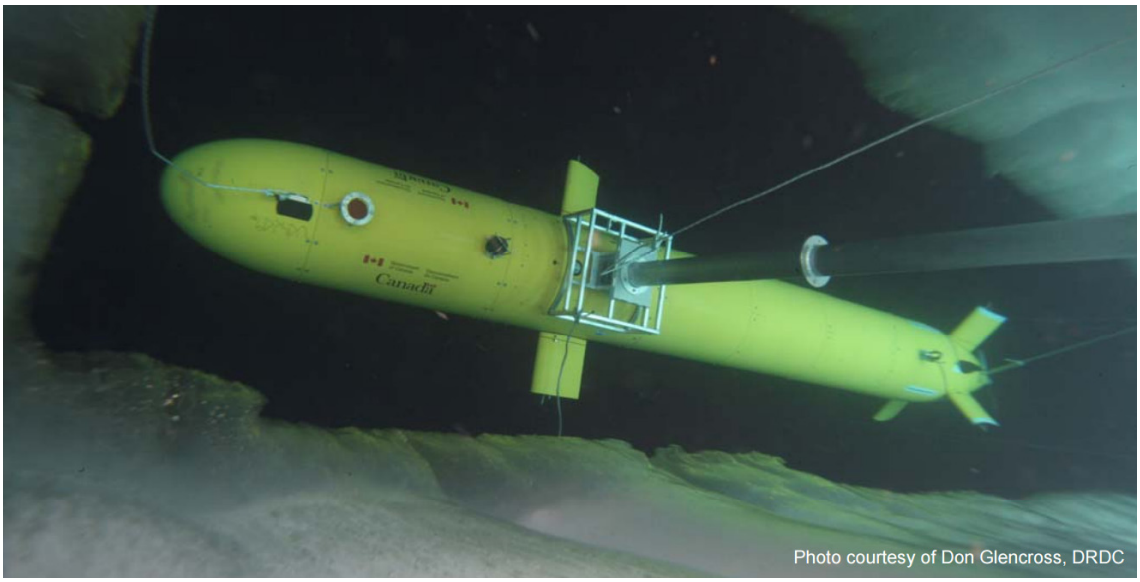


**FIGURE 1.1 - ISE ARCTIC EXPLORER AUV [1]**

AUVs have the ability to explore great depths and travel long distances in a capacity not possible with other technologies. Similarly, these unique abilities bring forth exceptional challenges as the vehicle, once operating beyond the range of high bandwidth communication, must accomplish its programmed mission while independently accounting for:

- **Limited resources**: These vehicles only have the resources that are deployed with them (such as battery capacity and compressed air) thus making judicious use of these resources a necessity.
- **Control capacity**: It is important to ensure that the AUV control system is capable of successfully completing maneuvers that are necessary to achieve its mission objects.

The primary mechanisms for controlling the movement of AUVs are a propeller for thrust and hydroplanes which are used to actuate the heading, depth/altitude, roll, and pitch. Ballasting, an additional control measure, can also be used to actuate depth/altitude and pitch. Traditional ballast control is simply to fix the ballast (e.g. with the attachment of weights) before deployment to achieve neutral buoyancy and trim at a specific depth such as the surface or the mission depth.

## 1.1 Motivation

Systems capable of actively modifying the ballast during operation are currently being researched for AUV applications and are termed variable ballast systems (VBS). Unlike hydroplanes, the use of this form of control is slower making it less useful for quick changes in depth or pitch.

Incorporating VBS into the design of AUVs introduces a new mode of control that enables a persistent vertical force without a continuous energy cost such as the drag loss from utilizing the hydroplanes. Introducing a second tank, locating one at the bow and one at the stern, permits the added ability to adjust the pitch of the vehicle.

## 1.2 Literature Review

The ability of a VBS to reliably and repeatedly respond to commanded changes in the AUV's buoyancy was identified by Carroll (1980) [2]. In the paper the author proposed a seawater hydraulic design for its theoretical efficiency and reliability, but also considered other designs including an expandable oil filled bladder and a seawater hydraulic design with high pressure air regulation. In Defa et al. (2011) [3] a review of

current practices for VBS on manned submersibles was conducted and the author then developed a prototype which was also tested for a seawater ballast system. Kemp et al. (2012) [4] explored the use of an oil bladder system for their experiment using a physical AUV where the oil bladder system was used to help hold the AUV position relative to the ocean floor. As part of their research, Kemp et al. proposed an energy management technique termed 'Sprint-and-Drift' where the vehicle would sprint to a point of interest and enter a low-power drift mode to maintain position in a low-current environment. The VBS was used in this design to establish neutral buoyancy which reduced unwanted changes in depth during the drift phase.

In Motyka and Bergmann (1984) [5] a control concept was introduced for the inclusion of VBS in AUVs. The paper presented a proof of concept using a simple AUV model with a tank at each of the fore and aft of the vehicle to achieve neutral buoyancy and zero pitch while nulling the hydroplane angles. This idea was furthered in DeBitetto (1995) [6] where the author added the simulated utilization of a fuzzy controller in an effort to more readily tune the control loop by controlling just the ballast tanks without any simulation of the hydroplanes. DeBitetto also demonstrated that VBS could be used for a step change in depth of 25 m while maintaining a zero pitch.

Over the years numerous control schemes for AUVs without VBS (ranging from the classical PID loop to more modern neuro-fuzzy controllers) were used and conceptualized, which was the topic of Craven et al. (1998) [7] who compiled and explored their benefits and limitations. These authors found that the AUV's autopilot PID system, not surprisingly, was unable to adapt to the vehicle's non-linear dynamics. Craven et al., therefore, suggested that adaptive control techniques could address these limitations but, in turn, required on-line system identification, and that fuzzy controllers with their rules-based approach may be appropriate for this application having been successfully used in several other similar applications.

Later, Lea et al. (1999) [8] carried out a comparative analysis of control strategies used in AUVs and concluded with a test of classical, fuzzy and sliding mode controllers (SMC)

on the Subzero II which did not have a VBS. They noted that, while a classical controller (such as PI or PD) was simple to implement, it required at least a basic system model for its design. The SMC required a significantly more sophisticated model, and the fuzzy controller required much more tuning resulting in a less robust response.

Tangirala and Dzielski (2007) [9] installed a dual ballast tank system on a large AUV called the Seahorse. The objectives of the paper were to the use VBS for depth and trim control without the input of the AUV's hydroplanes. In both the presented simulation and sea trial the tanks were utilized to individually control the pitch and depth with classical (PD) control loops with the respective parameters as feedback. Water tests showed that, for launching the AUV to depths of up to 10m, their method was adequate to realize step responses in either depth or pitch.

More recently, Woods et al. (2012) [10] proposed a hybrid conditioned-based PD controller for simultaneously controlling both AUV depth and pitch. The potential benefits were demonstrated in a two-dimensional computer simulation of a seawater ballast system using a high pressure air supply. The system utilized the pressure differential where possible to achieve the desired flow by opening a valve to minimize the use of a pump. In addition to this work, the authors included an analysis of resource consumption via an estimate of the amount of compressed air used and the total volume of water that flowed in and out of the tanks. The paper concluded that further work should endeavor to better estimate the VBS air and water flow rates as well as to develop a 3D simulator to study the modeling and control of VBS for AUVs.

Finally Liu et al. (2015) [11] used a lab-simulated environment to control only mass of a VBS independent of an AUV or other submersible. Liu et al. compared PD control and general predictive control (GPC) and concluded that both methods were feasible with GPC displaying better tracking performance in some conditions and PD displaying better energy efficiency.

The use of VBS on unmanned vehicles was first conceptualized in the early 1980s with control schemes following shortly thereafter. Since then, physical designs have

advanced for VBS in the field of AUV control. Despite this development the use of VBS on AUVs is still not common and the few examples where it has been used have been restricted to step changes in depth to typically less than 25m and a zero setting or step change setting in pitch.

As such the question still remains on how VBS can be used in tandem with hydroplanes to control the AUV and how to do so as efficiently as possible.

## 1.3 Objective

The fundamental objectives of this thesis then are to:

- design and implement a corresponding PID control approach for AUVs equipped with VBS
- investigate methods to improve the efficient use of VBS
- simulate specific scenarios where VBS might prove beneficial for AUVs in depths up to 4000 m (as in the case of, for example, the ISE Explorer AUV).

These objectives will be achieved through the following means:

- develop a six degree-of-freedom 3D computer simulator of an AUV in Mathworks' Matlab/Simulink
- develop a free-flow capable seawater hydraulic VBS model with high pressure air support in Mathworks' Matlab/Simulink for the AUV
- estimate power consumption used by VBS, AUV thrust and hydroplanes

## 1.4 Organization of Thesis

The thesis is organized as follows:

Chapter 2: The equations of motion and hydromechanics for AUVs are reviewed and a model is generated and validated.

Chapter 3: A control strategy for AUV motion using hydroplane control is developed.

Chapter 4: The equations governing the flow of air and water within the VBS are reviewed and a model is generated and validated.

Chapter 5: A control strategy for VBS to operate in a complementary fashion with the AUV hydroplanes is developed.

Chapter 6: The VBS and hydroplane control strategies for maneuvering the AUV are merged and tested on scenarios where VBS may be beneficial.

Chapter 7: Conclusions are drawn and recommendations are made.

# Chapter 2: AUV Model

For the purpose of this thesis the AUV coordinate system shall use $y_0$ as the vertical axis with the zero reference at the water's surface and up as positive. The axes $x_0$ and $z_0$ shall be the horizontal directions with $x_0$ being aligned along the length of the AUV as seen in Figure 2.1. This notation complies with the Simulink SimMechanics tool coordinate system used in this thesis which is different than the typical coordinate system used in marine applications.

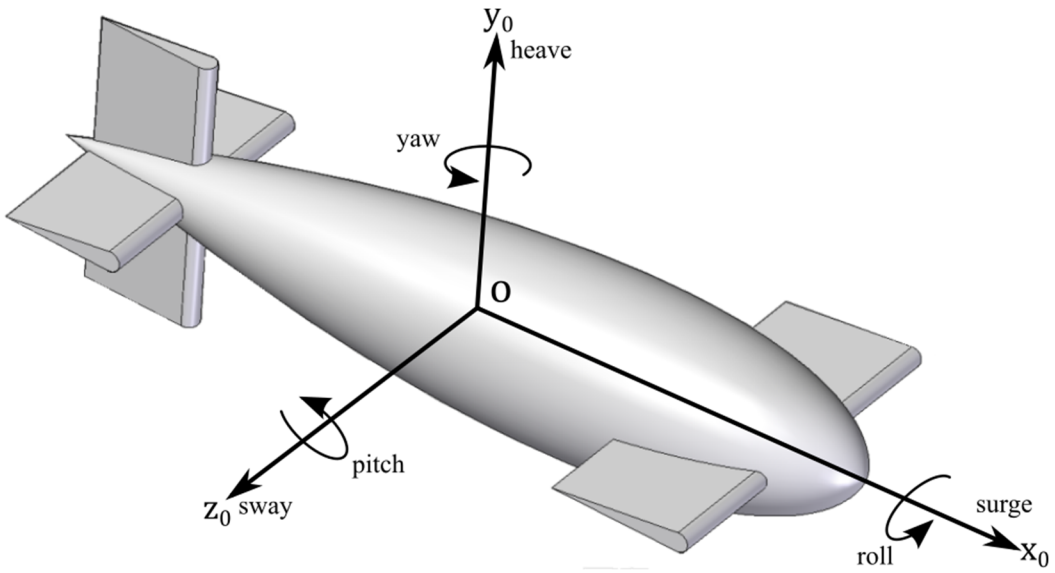


**FIGURE 2.1 - AUV COORDINATE SYSTEM AXES (AUV NOT TO SCALE)**

Using the notation in Table 2.1, the AUV's position and attitudes can then be described as a vector as follows [12]:

$$\eta = \begin{bmatrix} \eta_1 \\ \eta_2 \end{bmatrix}; \quad \eta_1 = \begin{bmatrix} x \\ y \\ z \end{bmatrix}; \quad \eta_2 = \begin{bmatrix} \phi \\ \theta \\ \psi \end{bmatrix} \tag{2.1}$$

Similarly, the velocity vector can be described as:

$$\nu = \begin{bmatrix} \nu_1 \\ \nu_2 \end{bmatrix}; \quad \nu_1 = \begin{bmatrix} u \\ v \\ w \end{bmatrix}; \quad \nu_2 = \begin{bmatrix} p \\ q \\ r \end{bmatrix} \tag{2.2}$$

Finally, the forces and moments from Table 2.1 can be written as:

$$\tau = \begin{bmatrix} \tau_1 \\ \tau_2 \end{bmatrix}; \quad \tau_1 = \begin{bmatrix} X \\ Y \\ Z \end{bmatrix}; \quad \tau_2 = \begin{bmatrix} \mathrm{K} \\ \mathrm{M} \\ \mathrm{N} \end{bmatrix} \tag{2.3}$$

**TABLE 2.1 - COORDINATE SYSTEM NOTATION**

| DOF | | | Force/Moment ( $\tau$ ) | Velocity ( $\nu$ ) | Position ( $\eta$ ) |
|---|---|---|---|---|---|
| **1** | translational | Motions in x (surge) | X | u | x |
| **2** | | Motions in y (heave) | Y | v | y |
| **3** | | Motions in z (sway) | Z | w | z |
| **4** | rotational | Rotation about x (roll) | K | p | ϕ |
| **5** | | Rotation about y (yaw) | M | q | θ |
| **6** | | Rotation about z (pitch) | N | r | ψ |

## 2.1 Equation of Motion

The general non-linear equations of motion for the AUV can be written as [12]:

$$M\dot{\nu} + C(\nu)\,\nu + D(\nu)\,\nu + g(\eta) = \tau \tag{2.4}$$

where:

$M$ = mass and moments of the system

$C(\nu)$ = Coriolis and centripetal term

$D(\nu)$ = damping due to hydrodynamic forces

$g(\eta)$ = hydrostatic forces due to gravity and buoyancy

$\tau$ = applied forces

## 2.2 Mass/Moments

It was assumed that the AUV has a mass $m_{auv}$ and is modeled as a circular cylinder to estimate the moments of inertia. The conceptual diagram of the model can be seen in Figure 2.2.

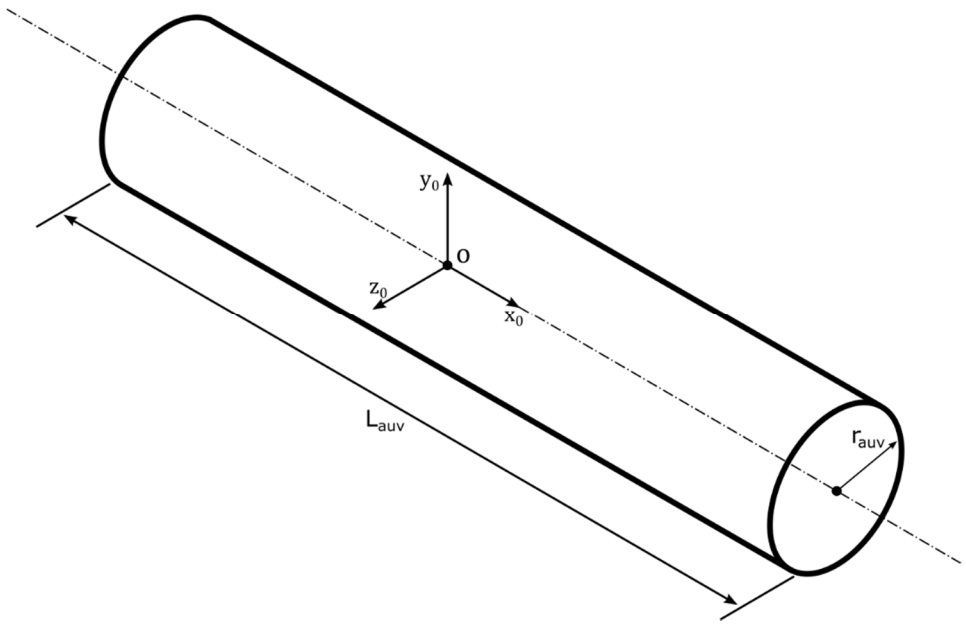


**FIGURE 2.2 - AUV MODELLED AS CYLINDER**

Using the dimensions and coordinate system in Figure 2.2 the moments of inertia could then be calculated as [13]:

$$I_x = \frac{1}{2}\, m_{auv}\, r_{auv}^2 \tag{2.5}$$

$$I_y = \frac{1}{12} m_{auv}\, [3\, r_{auv}^2 + L_{auv}^2] \tag{2.6}$$

$$I_z = I_y \tag{2.7}$$

Because the 3D AUV computer simulator was developed in Matlab and Simulink, the Coriolis and centripetal term $C(\nu)$ were calculated as part of the dynamics engine within the SimMechanics toolbox. Along with the mass and inertia of the AUV there is still an additional mass (which is significant because of the relatively high density of water) which needs to be modelled with submersed vehicles, termed virtual added mass.

### 2.2.1 Virtual Added Mass

For a body moving through water there is a volume of fluid which accelerates with the body and its shape is a function of the AUV's geometry in different directions. As the profile of the AUV is not uniform in all directions, neither is the shape of the water volume entrained with it for each of the six degrees-of-freedom. The result, for the translational degrees-of-freedom, is an added mass force given by:

$$F_{am} = \begin{bmatrix} A_{\mathrm{X}} & 0 & 0 \\ 0 & \mathrm{A_Y} & 0 \\ 0 & 0 & A_{\mathrm{Z}} \end{bmatrix} \begin{bmatrix} \dot{u} \\ \dot{v} \\ \dot{w} \end{bmatrix}. \tag{2.8}$$

Longitudinally the added mass value $A_X$ along the length of the AUV can be estimated as 10% of that of the vehicle [12]; however, the other directions need to be calculated from the AUV profile. Continuing with the AUV cylindrical hull assumption and adding a pair of hydroplanes, the model of the AUV can be split into three sections of different profiles:

A. cylindrical hull of radius $r_{auv}$
B. horizontal set of hydroplanes with span ending at $b$ from center line
C. cross layout of hydroplanes again of length $b$

This division along the length of the vehicle is shown in Figure 2.3.

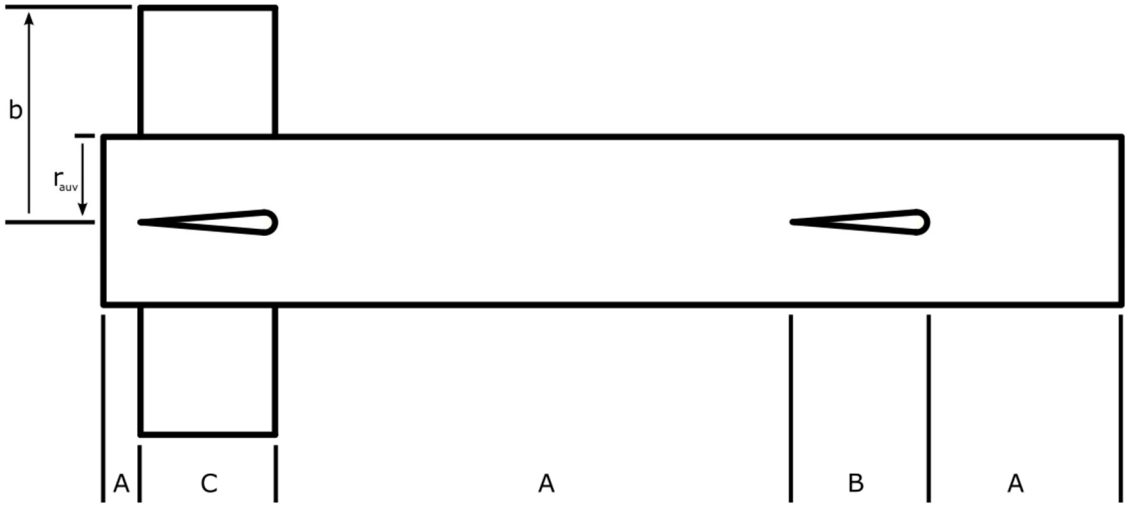


**FIGURE 2.3 - AUV ADDED MASS PROFILE SECTIONS (NOT TO SCALE)**

Note that the AUV is modelled in this instance with the aft hydroplanes in a cruciform configuration which is used for as an approximation for calculating added mass of the AUV as a whole. Later when the hydrodynamic forces are determined this orientation is changed to an X formation to better model these forces separate from the hydrodynamic forces on the AUV hull. This model overlooks some dynamic details such as the end cone and some second order effect as they are not necessary in achieving the objective of this thesis.

Each of these sections contribute to the total added mass in both the Y and Z-directions per unit length as well as the moment K (rolling) about the x axis. The values per section can be seen in Figure 2.4 [14] where $\rho$ refers to the density of the immersed fluid.

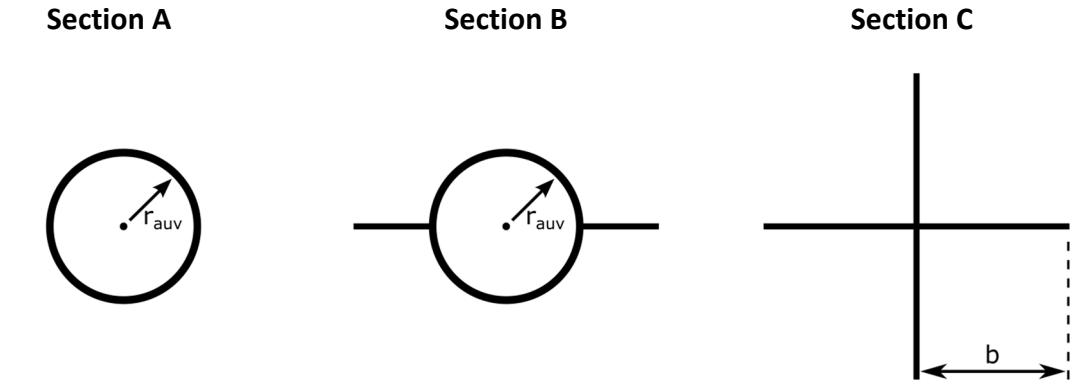


**FIGURE 2.4 - SECTIONAL ADDED MASS VALUES (SUCH THAT ρ = WATER DENSITY)**

Thus the added mass in the Y and Z directions are the sum of the product of the sectional lengths and added mass given as:

$$A_{\mathrm{Y}} = \sum_{i=0}^{n} m_{\mathrm{Y}_i} (L_i - L_{i+1}) \tag{2.9}$$

$$A_{\mathrm{Z}} = \sum_{i=0}^{n} m_{\mathrm{Z}_i} (L_i - L_{i+1}). \tag{2.10}$$

For any particular section of the vehicle, added moment of inertia would be the product of the unit length mass $m_{Y_i}$, length of section $dx$, moment arm $x$ and angular acceleration as follows:

$$dM = m_{\mathrm{Y_i}}\, \dot{q}\, x^2\, dx. \tag{2.11}$$

Integrating along a section (Figure 2.3) gives:

$$A_M = m_{Y_1}\, \dot{q} \int_{L_2}^{L_1} x^2\, dx \tag{2.12}$$

$$= \frac{1}{3}\, m_{Y_1}\, \dot{q}\, (L_1^3 - L_2^3). \tag{2.13}$$

Integrating along the entire length of the vehicle gives:

$$A_M = \frac{1}{3}\, \dot{q} \sum_{i=0}^{n} m_{Y_i} \left(L_i^3 - L_{i+1}^3\right). \tag{2.14}$$

Similarly, about the Z-axis this added moment of inertia would be:

$$A_N = \frac{1}{3} \dot{r} \sum_{i=0}^{n} m_{Z_i} \left(L_i^3 - L_{i+1}^3\right). \tag{2.15}$$

## 2.3 Hydrostatic forces

The two hydrostatic forces on a submerged vehicle are gravity $F_g$ and displacement $F_\Delta$ which are applied at the center of gravity CoG and center of buoyancy CoB respectively. Net buoyancy $F_{buoyancy}$ is the difference between these two forces [15] and can be expressed as:

$$F_g = m_{auv}\, g \tag{2.16}$$

$$F_\Delta = \rho_{sw}\, \overline{V}\, g \tag{2.17}$$

$$F_{buoyancy} = F_\Delta - F_g \tag{2.18}$$

where:

$\rho_{sw}$ = density of the sea water

$\overline{V}$ = wetted volume of the AUV

$g$ = acceleration due to gravity.

The difference between these two forces determines whether the AUV is positively buoyant ($F_\Delta > F_g$) where, in the absence of other forces, the craft will ascend, negatively buoyant ($F_\Delta < F_g$) where the AUV will descend, or neutrally buoyant where the AUV will stay at its current depth.

In addition to magnitude, the relative locations where these forces are applied affects the angle at which the vessel orients itself at rest. As seen in Figure 2.5 the center of buoyancy CoB where the displacement force is applied is initially offset along the length of the craft from the center of gravity CoG where the force of gravity is applied, thus resulting in a moment that tends to pitch it up to the equilibrium orientation where the two vectors are aligned vertically.

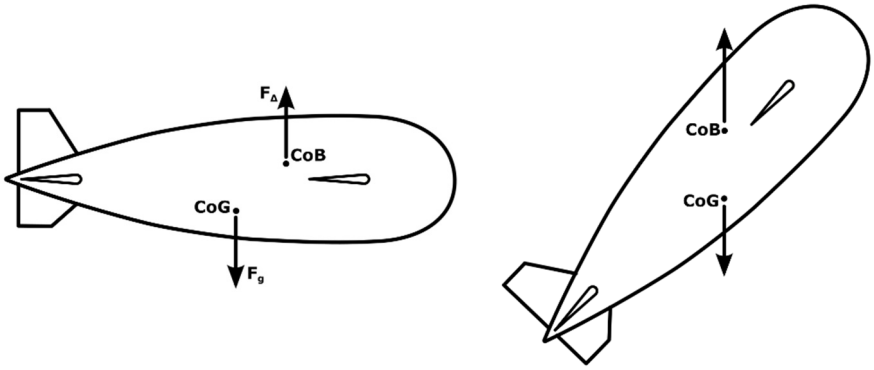


FIGURE 2.5 - EFFECT OF COB AND COG AT OFFSET

### 2.3.1 Static Force Variations

Although described as static, the displacement force $F_\Delta$ is affected by changes in depth. As seen in the profile shown in Figure 2.6, seawater density $\rho_{sw}$ is a function of salinity, temperature and pressure [16] which varies non-linearly with depth [16] and directly affects this force as expressed in Equation (2.17).

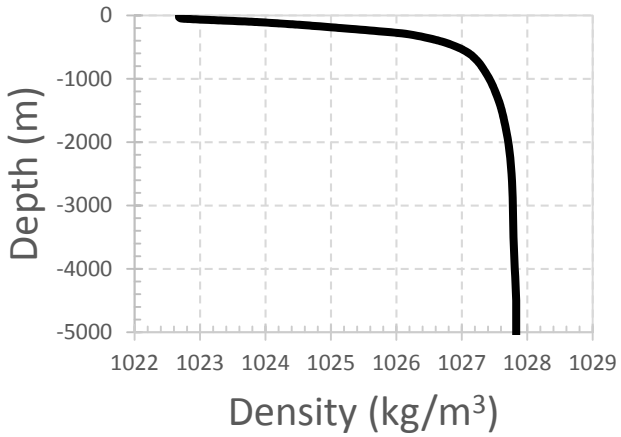


**FIGURE 2.6 - SEAWATER DENSITY TO 5000M MEASURED AT 17°N 162°W**

In addition to changes in seawater density, the hull of the AUV will compress due to the higher hydrostatic pressure at greater depths. For example, the STAR II had a unit compression coefficient of $2.63 \times 10^{-6}$ per meter as a ratio of total volume [15]. These two effects influence the net buoyancy of the AUV. Figure 2.7 plots the percentage change in net buoyancy, hull volume and water density as a function of depth. In this figure, net buoyancy is defined as the combined effect of both the changes in hull volume and water density. It can be seen that initially the net buoyancy increases peaking near 500 m depth. The net buoyancy then reduces and eventually becomes negative around a depth of 2000 m.

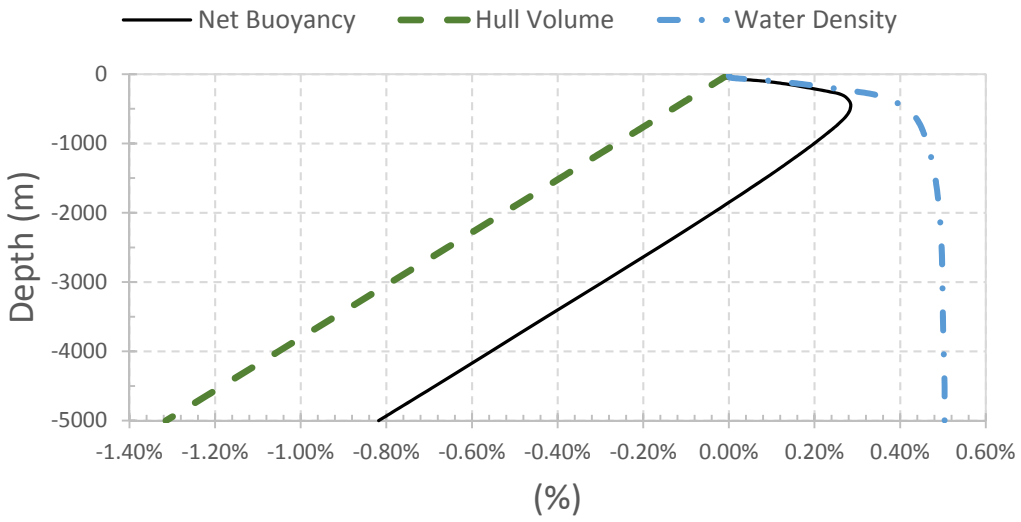


**FIGURE 2.7 - CHANGE IN NET BUOYANCY, HULL VOLUME AND WATER DENSITY AS A FUNCTION OF WATER DEPTH**

## 2.4 Hydrodynamics Forces

Hydrodynamic drag force $F_D$ is proportional to the square of the velocity with the equation given as:

$$F_D = \frac{1}{2}\,\rho\, C_D\, A\, v^2 \tag{2.19}$$

where:

$F_D$ = force of drag

$\rho$ = density of the fluid

$v$ = velocity of fluid relative to AUV

$C_D$ = coefficient of drag

$A$ = characteristic area.

For this thesis the drag force was calculated with each direction of translational motion (x, y and z) having a different drag coefficient and characteristic area. To simplify the model (with no loss of generality), the effects of these forces on the AUV were calculated individually at each reference point on the AUV model. This method works

well with SimMechanics which can provide the velocities in the reference frames of each component where the drag forces can then be calculated. As seen in Table 2.2 the AUV was modelled as a circular cylinder in the x direction with the forces applied at the body frame origin. Further fidelity could be gained by including a more comprehensive model of the AUV's hull (e.g. inclusion of truncated cone as the tail), however, was deemed unnecessary for the research in this thesis.

**TABLE 2.2 - AUV DRAG FORCE PARAMETERS FOR BODY (r = AUV RADIUS AND L = LENGTH FROM NOSE TO PROPELLER)**

| DIRECTION | MODEL CHARACTERISTIC | COEFFICIENT OF DRAG | CHARACTERISTIC AREA | |
|---|---|---|---|---|
| x | Streamlined Body | $C_{D_x} = 0.003$ [14] | Wetted Area | $S_x = 2\pi r_{auv}\,(r_{auv} + L_{auv})$ |
| y | Cylinder | $C_{D_y} = 0.025$ [17] | Frontal Area | $S_y = 2\,r_{auv}\;L_{auv}$ |
| z | Cylinder | $C_{D_z} = 0.025$ [17] | Frontal Area | $S_z = 2\,r_{auv}\,L_{auv}$ |

As the AUV generally moves with six degrees-of-freedom it was necessary to calculate not only the translational drag force but also the drag moment caused by the roll angular velocity $p$. This moment is given as the effective drag force $F_{D_p}$ times the moment arm which is the radius of the vehicle. As such the drag effect on the moment $K_{D_p}$ is calculated as:

$$K_{D_p} = r_{auv}\,F_{D_p} \tag{2.20}$$

The velocity at the surface of the AUV would be the rotational velocity $p$ multiplied by the vehicle's radius r to give:

$$v = r_{auv}\,p. \tag{2.21}$$

The characteristic surface area used to calculate drag of the cylindrical hull is based on a constant radius for the circular cylinder and is thus:

$$A = 2\,\pi\,r_{auv}\,L_{auv}. \tag{2.22}$$

Substituting the area from Equation (2.22) and the velocity from Equation (2.21) into Equation (2.19) gives the drag force as:

$$F_{D_p} = \frac{1}{2}\,\rho\,C_{D_x}\,2\,\pi\,r_{auv}^3\,L_{auv}\,p^2. \tag{2.23}$$

Finally, inserting this result into Equation (2.20) gives the drag moment as:

$$K_{D_p} = \frac{1}{2}\,\rho\,C_{D_x}\,2\,\pi\,r_{auv}^4\,L_{auv}\,p^2. \tag{2.24}$$

It is also necessary to calculate both the drag force and drag moment for translational and rotational motion about the Y and Z axes. To calculate these forces and moments in and around the two axes the translational and rotational effects were calculated separately and then added together.

To obtain the equation for the drag force $Y_{D_v}$, the appropriate terms for motion in the Y direction, as given in Table 2.2, were substituted into Equation (2.19) giving:

$$Y_{D_v} = \frac{1}{2}\,\rho\,C_{D_y}\,S_y\,v^2 \tag{2.25}$$

where:

$S_y$ = characteristic area in the Y-direction (vertical)

There is no moment created by the vertical force as it is applied at the geometric center of the body (assuming a constant radius circular cylinder) leaving the remainder of the drag forces to be calculated from the angular velocity $r$ (pitch). It can be seen in Figure 2.8 that the resultant velocity $xr$ at any point along the length of the AUV varies linearly with distance from the origin.

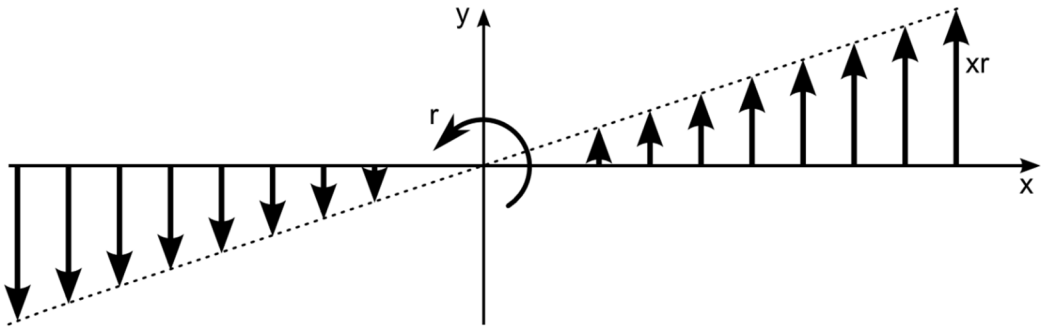


FIGURE 2.8 - LINEAR VELOCITY xr ALONG THE X AXIS DUE TO PITCH ROTATIONAL VELOCITY r

Calculating the drag force using Equation (2.19) results in the magnitude always being positive; however, the direction must change with the velocity as seen in Figure 2.9. It is therefore necessary to evaluate the drag force on either side of the origin separately.

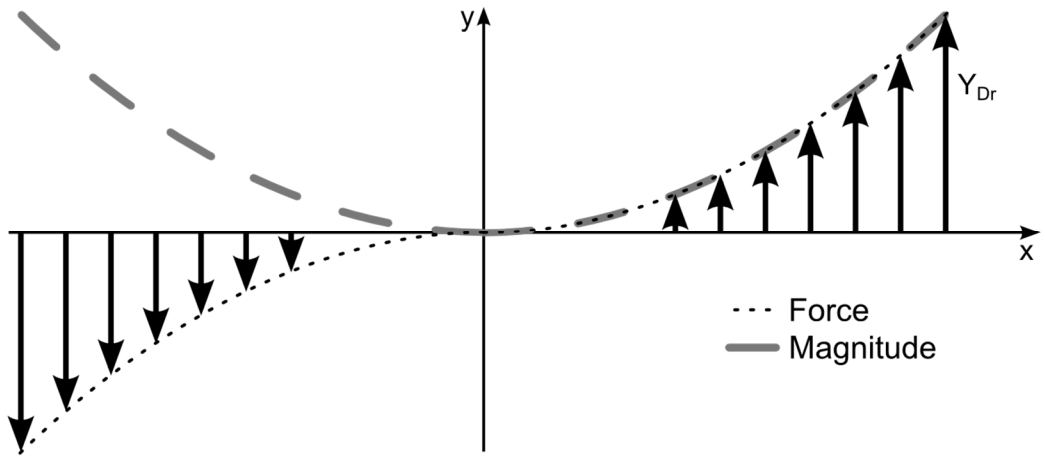


FIGURE 2.9 - DRAG FORCE V MAGNITUDE IN THE Y (VERTICAL) DIRECTION

The drag force $Y_{D_r}$ due to a rotation about the $z_0$ axis can then be calculated using Equation (2.19) and is given as:

$$Y_{D_r}(x) = \begin{cases} -\frac{1}{2}\,\rho\, C_{D_y}\,\frac{S_y}{L_{auv}}\,x^2 r^2, x < 0 \\ \frac{1}{2}\,\rho\, C_{D_y}\,\frac{S_y}{L_{auv}}\,x^2 r^2, x \geq 0. \end{cases} \tag{2.26}$$

Integrating Equation (2.26) gives:

$$Y_{D_r} = \int_0^{L_{auv}/2} \frac{1}{2}\,\rho\, C_{D_y} \frac{S_y}{L_{auv}}\, x^2 r^2 dx \tag{2.27}$$

$$+ \int_{-L_{auv}/2}^{0} -\frac{1}{2}\,\rho\, C_{D_y}\, \frac{S_y}{L_{auv}} x^2 r^2 dx \tag{2.28}$$

$$= \frac{1}{2}\,\rho\, C_{D_y} \frac{S_y}{L_{auv}} \left( \frac{L_{auv}^3 r^2}{24} - \frac{L_{auv}^3 r^2}{24} \right) \tag{2.29}$$

$$= 0.$$

Finally, the moment $N_{D_r}$ due to a rotation about the $z_0$ axis (pitch) is given by:

$$N_{D_r}(x) = x\, Y_{D_r}(x). \tag{2.30}$$

Combining Equations (2.27) and (2.30) yields the moment of this drag which is given as:

$$N_{D_r}(x) = \begin{cases} -\frac{1}{2}\,\rho\, C_{D_y} \frac{S_y}{L_{auv}}\, x^3 r^2, x < 0 \\ \frac{1}{2}\,\rho\, C_{D_y} \frac{S_y}{L_{auv}}\, x^3 r^2, x \geq 0 \end{cases} \tag{2.31}$$

$$N_{D_r} = \int_0^{L_{auv}/2} \frac{1}{2}\,\rho\, C_{D_y} \frac{S_y}{L_{auv}} x^3 r^2 dx \tag{2.32}$$

$$+ \int_{-L_{auv}/2}^{0} -\frac{1}{2}\,\rho\, C_{D_y} \frac{S_y}{L_{auv}} x^3 r^2 dx \tag{2.33}$$

$$= \frac{1}{2}\,\rho\, C_{D_y} \frac{S_y}{L} \left( \frac{L_{auv}^4 r^2}{64} + \frac{L_{auv}^4 r^2}{64} \right) \tag{2.34}$$

$$= \frac{1}{2}\,\rho\, C_{D_y}\, S_y\, \frac{k L_{auv}^3 r^2}{32}.$$

The total vertical drag force $Y_D$ is determined by adding Equations (2.25) and (2.29) to give:

$$Y_D = \frac{1}{2}\rho C_D S_y\, v^2 \tag{2.35}$$

The moment of drag is then given per Equation (2.34) as:

$$N_D = \tfrac{1}{2}\rho C_D S_y \tfrac{L_{auv}^3}{32}\, r^2. \tag{2.36}$$

Similarly, the force and moment equations in the z direction would be given as:

$$Z_D = \frac{1}{2}\rho C_D S_z \, w^2 \tag{2.37}$$

$$M_D = \frac{1}{2}\rho C_D S_z \frac{L_{auv}^3}{32} \, q^2. \tag{2.38}$$

### 2.4.1 Hydroplanes

The hydroplanes generate a drag force $F_D$ in the direction of motion as well as a lift force $F_L$ perpendicular to the direction of motion. The lift force $F_L$ can be calculated similar to that of drag in Equation (2.19) by simply replacing the coefficient of drag with the coefficient of lift as follows:

$$F_L = \frac{1}{2} \, \rho \, v^2 \, C_L \, A \tag{2.39}$$

The hydroplane section selected for this thesis was NACA 0025. The coefficients of drag $C_D$ and lift $C_L$ in relation to the angle-of-attack can be seen in Figure 2.10 [18].

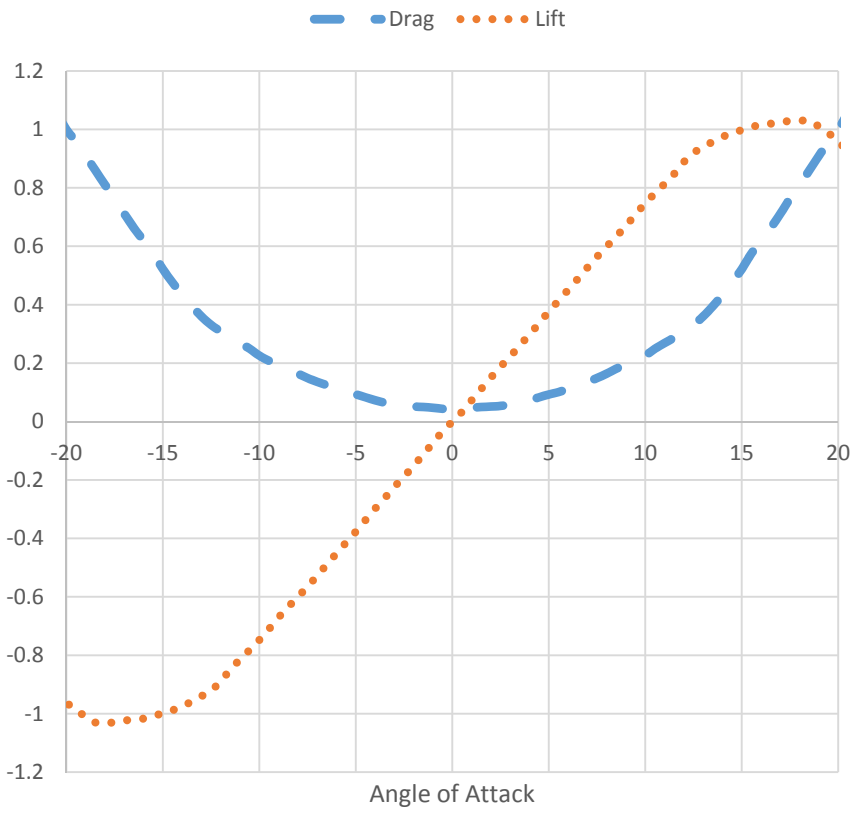


**FIGURE 2.10 - COEFFICIENTS OF LIFT & DRAG FOR NACA 0025 FOIL [18]**

Using a local reference frame on the hydroplane, as seen in Figure 2.11, the angle of attack $\theta$ can be calculated using the $u_{hf}$ (forward) and $v_{hf}$ (vertical) velocities and the controlled rotation angle α to give:

$$\theta = \beta - \alpha \tag{2.40}$$

where:

$$\beta = \text{atan}\frac{v_{hf}}{u_{hf}}. \tag{2.41}$$

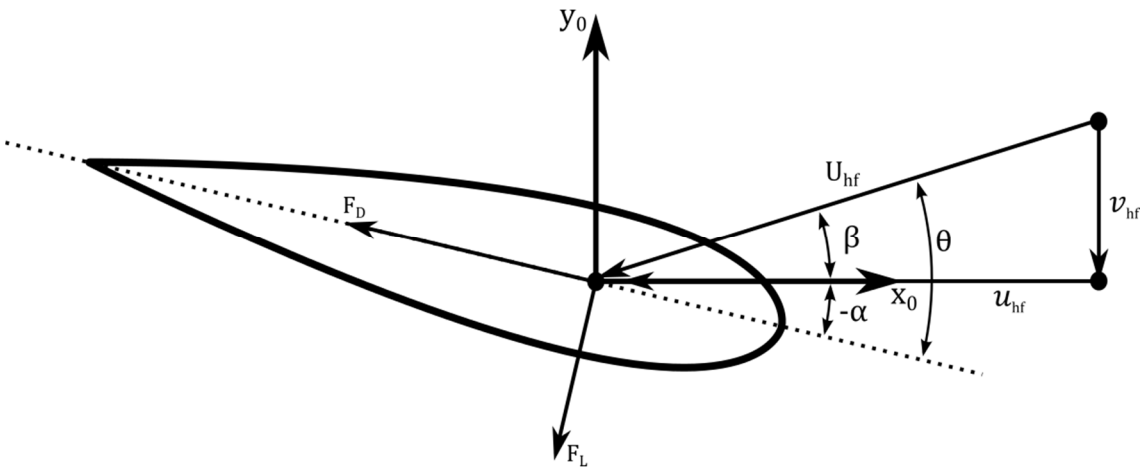


**FIGURE 2.11 - HYDROPLANE ANGLE OF ATTACK AND VELOCITY**

Using the calculated angle-of-attack to determine the coefficients of lift $C_{L_u}$ and drag $C_{D_u}$ and using $S_u$ as the surface area of the hydroplane, the resultant forces of drag $X_u$ and lift $Y_u$ are given as:

$$X_u = \frac{1}{2}\,\rho\, U_{hf}^2\, C_{D_u}\, S_u \tag{2.42}$$

and

$$Y_u = \tfrac{1}{2}\,\rho\, U_{hf}^2\, C_{L_u}\, S_u. \tag{2.43}$$

The effective velocity $U_{hf}$ is calculated as:

$$U_{hf} = \sqrt{u_{hf}^2 + v_{hf}^2}. \tag{2.44}$$

Additionally, the velocity $V_{hf}$ perpendicular to the chord line would be given as:

$$V_{hf} = U_{hf} \sin\theta \tag{2.45}$$

allowing the drag force to be calculated as:

$$Y_v = \frac{1}{2} \rho V_{hf}^2 C_{D_v} S_v \tag{2.46}$$

where:

$C_{D_v}$ = the coefficient of drag for a rectangular plate

$S_v$ = frontal area of the hydroplane in the Y direction.

Adding all of the hydroplane forces $\tau_{hf_\alpha}$ in the α-rotated frame yields:

$$\tau_{hf_\alpha} = \begin{bmatrix} X_u \\ Y_u + Y_v \\ 0 \end{bmatrix} \tag{2.47}$$

To rotate these forces back into the hydroplane local reference frame requires a rotation about the z axis of angle –α. The corresponding transformation matrix is given as:

$$R_\alpha = \begin{bmatrix} \cos\alpha & -\sin\alpha & 0 \\ \sin\alpha & \cos\alpha & 0 \\ 0 & 0 & 1 \end{bmatrix}. \tag{2.48}$$

The forces can then be calculated in the local reference frame and transformed to the global one using:

$$\tau_{hf} = R_\alpha \tau_{hf_\alpha}. \tag{2.49}$$

This approach can be applied at the reference point (quarter cord) for each hydroplane.

## 2.5 Model Implementation in SimMechanics

SimMechanics facilitates modelling the rigid body dynamics and permits the user to define the translations and rotations between key points on the body. In the case of the AUV these points were:

- hydroplane reference points

- vehicle center of buoyancy
- vehicle center of gravity
- origin (arbitrarily assigned)

The ISE Arctic Explorer is the vehicle selected in this thesis to be used as the inspiration for the model and used for establishing an appropriate scale. This craft has a long circular cylindrical body with a set of bow planes at the fore of the craft and a set of hydroplanes configured in an X at the stern. This orientation is different than the cruciform depicted in Figure 2.3 which was used only to approximate the added mass. The model omits the inclusion of the conical tail of the Arctic Explorer for simplicity. The transformations from the origin (geometric centre of the circular cylinder) to the hydroplane reference points is depicted in Figure 2.12.

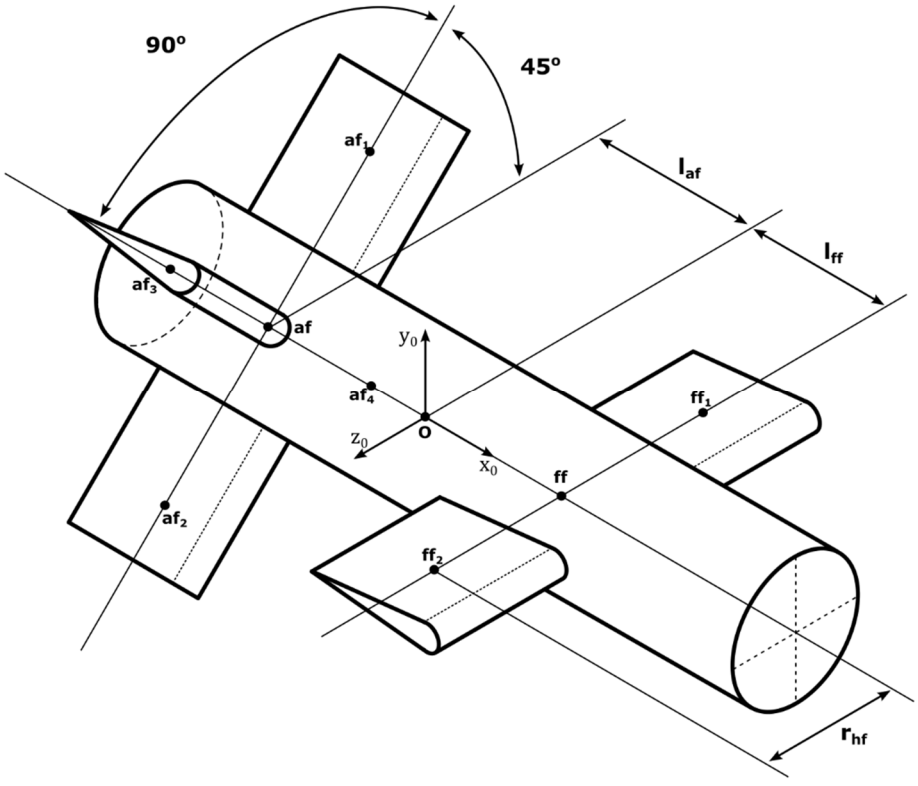


FIGURE 2.12 - AUV SIMMECHANICS TRANSLATIONS AND TRANSFORMATION REFERENCE POINTS

In Table 2.3 the locations of each of these reference points are denoted in relation to either the origin O or another reference point. For each point, a rotation and a translation is then given to define the transformation in its new reference frame. This transformation commences with a rotation about the x-axis as denoted in the third column in Table 2.3. With the new orientation defined, a translation along the axis given in the fourth colum with the amount shown in the fifth column of Table 2.3 gives the position of each point shown in Figure 2.12.

**TABLE 2.3 - AUV REFERENCE POINTS**

| POINT | FROM POINT | ROTATION | TRANSLATE | |
|---|---|---|---|---|
| | | ABOUT X | Axis | Distance |
| **ff** | O | 0° | x | $+l_{ff}$ |
| **$ff_1$** | ff | 0° | z | $-r_{hf}$ |
| **$ff_2$** | ff | 0° | z | $+r_{hf}$ |
| **af** | O | 0° | x | $-l_{af}$ |
| **$af_1$** | af | 45° | z | $-r_{hf}$ |
| **$af_2$** | af | 45° | z | $+r_{hf}$ |
| **$af_3$** | af | 135° | z | $-r_{hf}$ |
| **$af_4$** | af | 135° | z | $+r_{hf}$ |

The center of mass is located at $r_g$ from the origin with the center of buoyancy at $r_b$ where the calculated displacement forces were applied. Both $r_g$ and $r_b$ are defined as vectors with components in the X, Y, and Z directions. All drag forces and moments for the main hull were applied at the geometric center of the cylinder body coinciding with the origin O. The values and descriptions for all the variables are presented in Table 2.4 which is based on the published information on the ISE Arctic Explorer.

TABLE 2.4 - AUV CHARACTERISTICS VALUES

| VARIABLE | DESCRIPTION | VALUE |
|---|---|---|
| **m** | mass of AUV | 2200 kg |
| **$L_{auv}$** | length of AUV | 7.4 m |
| **$r_{auv}$** | radius of AUV | 0.37 m |
| **$r_g$** | position of CoG from origin | [0, -0.0925, 0] m |
| **$r_b$** | position of CoB from origin | [0, 0, 0] m |
| **$l_{ff}$** | distance from origin to ¼ chord of fore hydroplanes | 0.5 m |
| **$l_{af}$** | distance from origin to ¼ chord of aft hydroplanes | -3.2 m |
| **$r_{hf}$** | distance from x axis to center of force on hydroplane | 0.592 m |
| **s** | Hydroplane span | 0.37 m |
| **c** | Hydroplane chord | 0.37 m |

Validation of this model is discussed in Appendix A:.

## 2.6 Power Consumption Considerations

### 2.6.1 Thrust power

As power consumption is of great concern for the AUV (which has limited battery life) the simulation model requires an estimate on the amount of energy used. The main consumer of energy for moving the vessel is the propeller which has an effective power consumption of:

$$P_{out} = u\, F_T \tag{2.50}$$

where:

$u$ = the longitudinal velocity in the local X direction

$F_t$ = the applied thrust force

Output power from the propeller can also be given as:

$$P_{out} = \eta_t \, P_{in} \tag{2.51}$$

where:

$\eta_t$ = total efficiency of the propulsion system

$P_{in}$ = power input to the propulsion system

Therefore, the power required to propel the AUV can be calculated using Equations (2.50) and (2.51) to give:

$$P_{in} = \frac{u \, F_T}{\eta_t} \tag{2.52}$$

Total efficiency $\eta_t$ given by Allemagne [15] varies from 55% up to 85% for a submersible vehicle. For this thesis this efficiency will conservatively be assumed to be 60%.

### 2.6.2 Hydroplane Power

The hydroplane power consumed in operation can be calculated as:

$$P = F_Y \, \dot{\alpha} \, l_{hp} \tag{2.53}$$

where:

$F_Y$ = the sum of hydroplane forces in the hydroplane reference frame Y direction (Equation (2.47) )

$l_{hp}$ = the moment arm of the force which is assumed to be 10 cm

$\dot{\alpha}$ = the rotation speed of the hydroplane

In addition to power consumption when the hydroplanes were in motion, the power required to hold a hydroplane at a fixed angle was selected to be 5W for any hydroplane deflection angle $\alpha$ other than 0°.

# Chapter 3: Hydroplane Control

Movement of the AUV is traditionally controlled by the hydroplanes and the propeller. Using the hydroplanes, the vehicle can adjust its roll φ, heading $\theta$, pitch $\psi$, and depth/altitude $y$. The propeller provides the forward propulsion against a velocity setpoint. The forward speed of the AUV, in turn, determines the lift forces generated by the hydroplanes (see Equation (2.39)) to otherwise change its position and attitude.

## 3.1 Thrust Control

To simulate the effect of a propeller thrust a force $F_T$ was applied to the stern of the vessel (Figure 3.1) along the centerline of the AUV in the X direction.

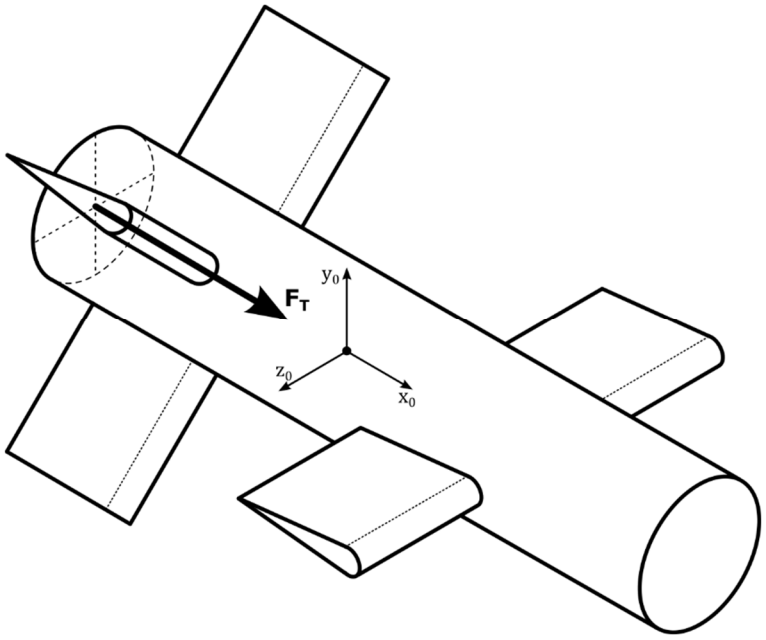


**FIGURE 3.1 - APPLIED THRUST FORCE $F_T$ ON AUV**

Limitations were placed on this thrust force both in its magnitude and in its reaction time. As such, the minimum thrust was assumed to be zero with the maximum selected to coincide with the published top speed of the ISE Arctic Explorer (2.5 m/s). In order to run the model at this velocity the necessary force was found to be 400 N.

To prevent an instantaneous reaction in thrust force, a ramp-up time for the thrust force was set to be approximately 500 milliseconds which was achieved by using the

transfer function 10/(s+10). Figure 3.2 shows a model of the simulated propeller where the thrust controller commands a set thrust force $F_{Tset}$ as an input. The resultant force $F_T$ is produced after being limited in response by the transfer function and also by the saturation limits of 0N as a minimum and 400N as a maximum.

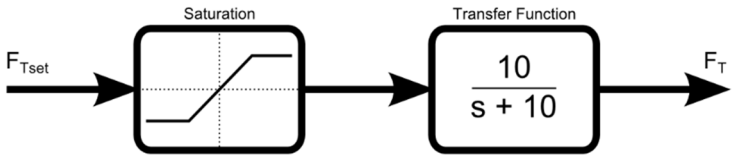


FIGURE 3.2 - THRUST MODEL

The corresponding control loop for thrust is shown in Figure 3.3 where the input to the loop is the body frame (hydrodynamic) velocity $u$ taken directly from the AUV model. This value is compared to the desired velocity $u_{set}$. The resultant error $u_{err}$ is then sent to the PID control which, in turn, sends a signal $F_{Tset}$ to the Thrust Model (Figure 3.2) which regulates the behaviour of the thrust force $F_T$. Finally, this force is then applied to the model of the AUV from Chapter Chapter 2:.

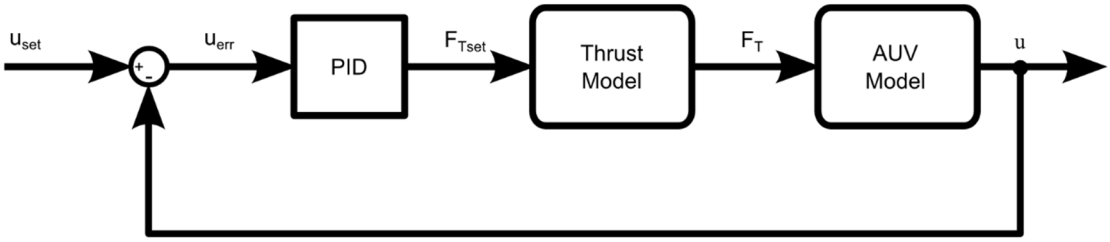


FIGURE 3.3 - THRUST CONTROL

To tune the AUV's thrust controller the system buoyancy was set to neutral and the hydroplane angles were all set to zero. These settings ensured that no outside influences were affecting the velocity of the AUV. The response of the system accelerating from 0 m/s to 2m/s is shown in Figure 3.4. In this figure the dashed line denotes the commanded velocity which is set to 0 for the first 20 seconds at which time there is a step input to 2 m/s. The subsequent dotted, dash-dot and solid lines are the resulting feedback velocity u using different gains of P = 400, P =1000 and P=1000 with I=200. Using only a proportional gain yielded a steady-state error. By including integral

gain, the desired speed was reached in approximately 20 seconds with no overshoot; therefore, the gains of P=1000 and I=200 were selected.

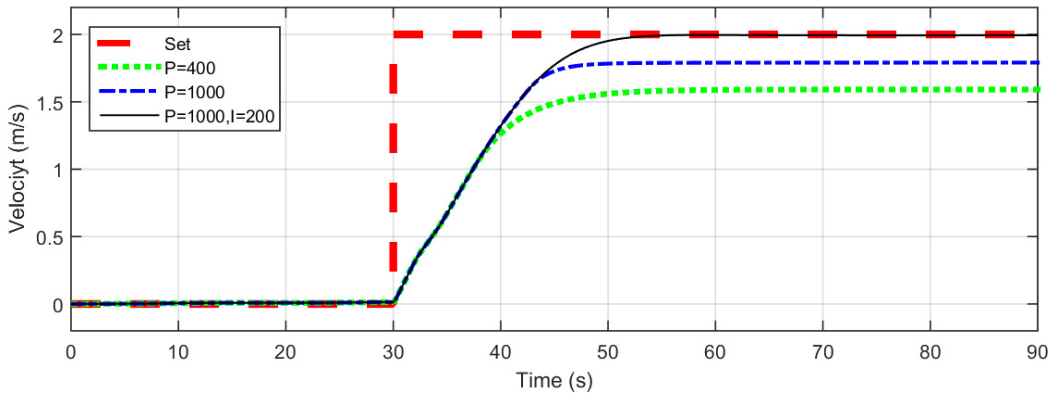


FIGURE 3.4 - VELOCITY STEP RESPONSES FROM 0 TO 2 M/S FOR THRUST CONTROLLER

## 3.2 Depth Control

The forces created by the bow planes are used to control depth as seen in Figure 3.5.

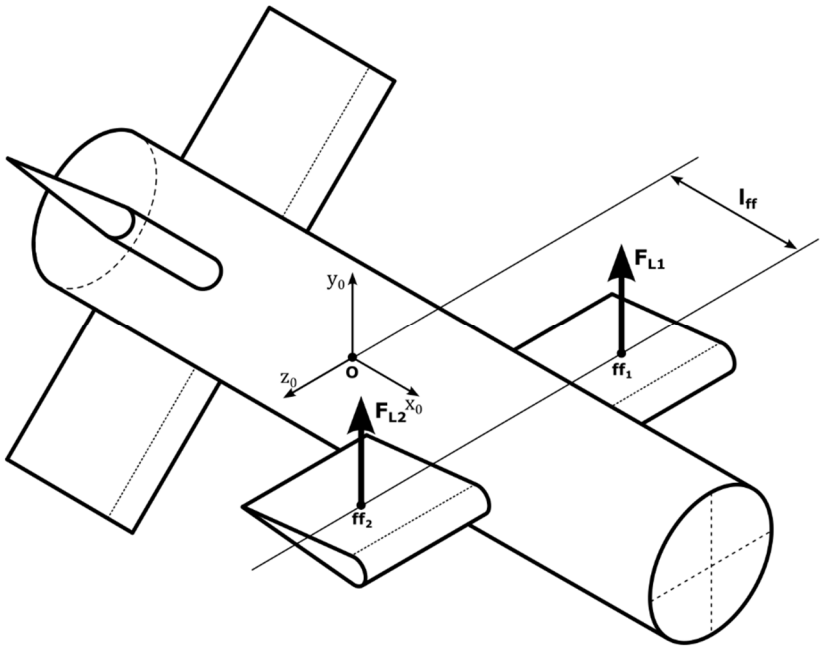


FIGURE 3.5 - APPLICATION OF BOW HYDROPLANE FORCES

Similar to the thrust force, limitations on the hydroplane performance were placed on the magnitude, reaction response, and the rate of change. The maximum deflection angle was selected to be ± 20° which is slightly higher than the critical angle-of-attack where the lift coefficient begins to reduce due to flow separation as seen in Figure 2.10. A rate limit on the angle was selected to be one degree per second and a transfer function 2/(s+2) was applied to prevent the hydroplanes from instantaneously changing from one angle to another. The constructed model which implements these limitations can be seen in Figure 3.6.

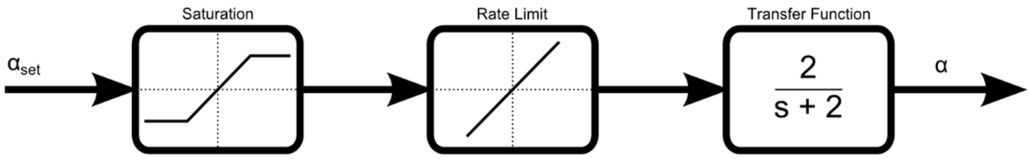


FIGURE 3.6 - HYDROPLANE MODEL

Bow plane control is shown in Figure 3.7. The input to this loop is the actual depth value $y$ which is subtracted from the setpoint depth $y_{set}$ to give the error value $y_{err}$ on which the PID controller acts. From there, a command signal $\alpha_{f_{set}}$ is delivered to the hydroplane model (Figure 3.6) which derives the deflection angle $\alpha_f$. This angle is then given to the AUV model where the effects of the hydrodynamic forces and rigid body dynamics are calculated.

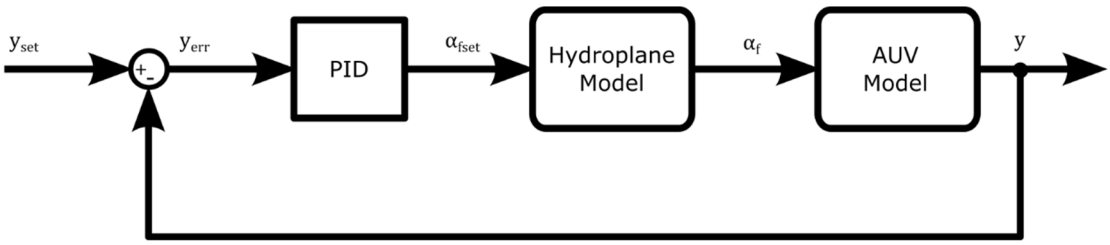


FIGURE 3.7 - BOW PLANE CONTROL

For tuning the depth controller, the velocity was set to 2 m/s and the AUV was again set to neutral buoyancy. The response of the tuned system can be seen in Figure 3.8 where the AUV dives from the surface to a depth of 20 m. Once more, the dashed line denotes the step command signal which changes from the surface to the set depth at 30 seconds. The subsequent dotted, dash-dot and solid lines are the feedback depth using the gains of P = 4, I = 0.05 and D = 4 where each gain term was added in consecutive tests. These gains, as well as all subsequent PID gains, were selected through an iterative process of adjusting the gains then running the step response as well as many of the other test runs used later in this thesis. All sets of gains achieved the set depth within 60 seconds of the step input; however, the PID controller was found to have the best response and was selected.

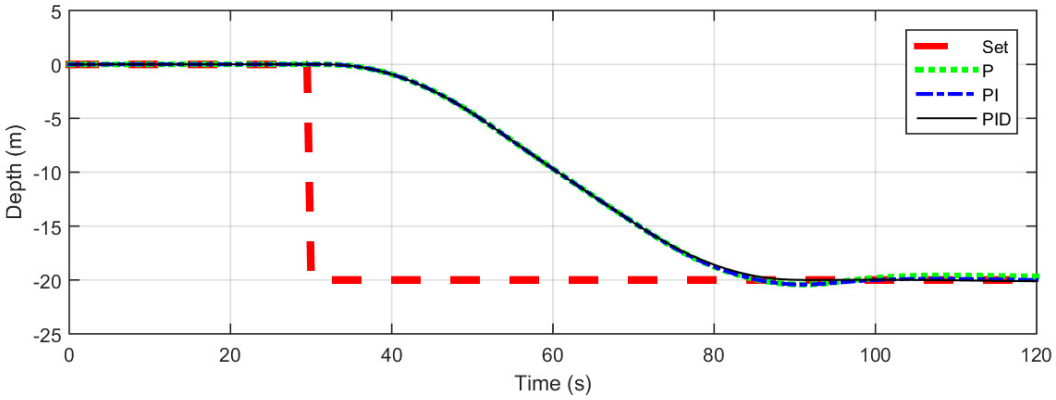


**FIGURE 3.8 - DEPTH STEP RESPONSES FROM 0 TO 20 M FOR FORE PLANE CONTROLLER**

## 3.3 Heading and Pitch Control

Heading and pitch control for the AUV are coupled requiring the two parameters to be controlled simultaneously. Shown in Figure 3.9, the stern hydroplanes are configured in an X formation and apply forces at 45 degrees to the lateral Z and vertical Y directions. In this way a deflected plane controls horizontal and vertical degrees of freedom. When combined these hydroplanes can create the forces needed to attain the desired heading $\theta$ and pitch $\psi$ values.

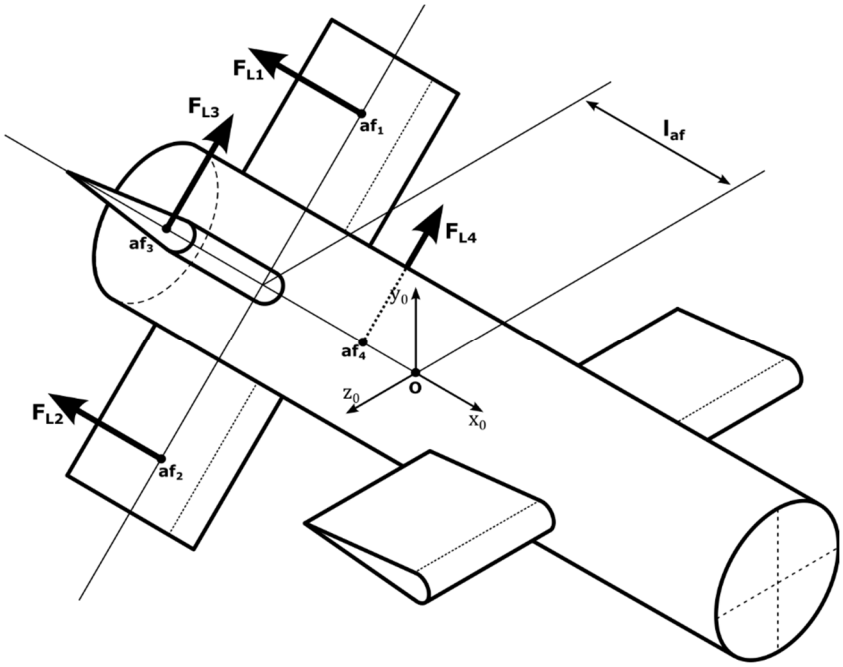


FIGURE 3.9 - APPLICATION OF STERN HYDROPLANE FORCES

For the purpose of this thesis the hydroplanes on opposite sides of the AUV stern were controlled to the same deflection angle $\alpha$ (see Figure 2.11). Assuming a deflection angle $\alpha_{a_1}$, the lift forces $F_{L1}$ and $F_{L2}$ would be equal. Similarly, for an angle $\alpha_{a_2}$ the forces $F_{L3}$ and $F_{L4}$ would correspond.

A view of the hydroplanes from the stern of the AUV is depicted in Figure 3.10. In this diagram the four forces are all oriented upward with the same magnitude. For the model, this orientation would be due to the rotation angles of each pair of hydroplanes being equal to $\alpha_\psi$. Hence the set angles would be given for this case as:

$$\alpha_\psi = \alpha_{a_1} = \alpha_{a_2} \tag{3.1}$$

The resulting sum of the forces can be seen in Figure 3.10 on the right where the horizontal components cancel leaving only the net vertical force $Y_{Lnet}$. This force, with the moment arm $l_{af}$, creates a torque on the AUV about its Z axis permitting the control of the pitch angle $\psi$.

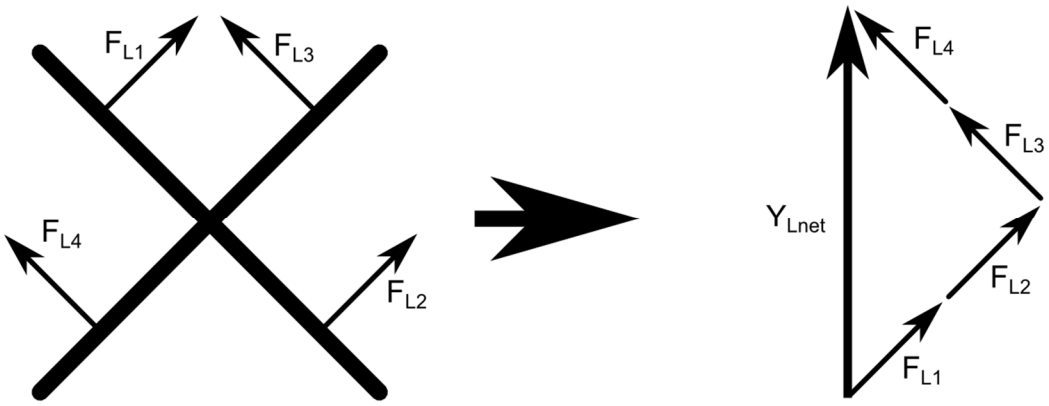


FIGURE 3.10 - X CONFIGURATION HYDROPLANES WITH NET VERTICAL FORCE

The same view can be seen in Figure 3.11 however, in this case, the rotation angles are now in opposite directions with an equal angle magnitude of $\alpha_\theta$. The rotation angles for this case would be given as:

$$\alpha_\theta = \alpha_{a_1} = -\alpha_{a_2} \tag{3.2}$$

These angles result in the forces being collectively oriented in the same horizontal direction. In this instance the vertical components of the forces cancel leaving a net force $Z_{Lnet}$. This force, with the moment arm $l_{af}$, permits the AUV to control its heading angle θ by creating a torque about the Y axis.

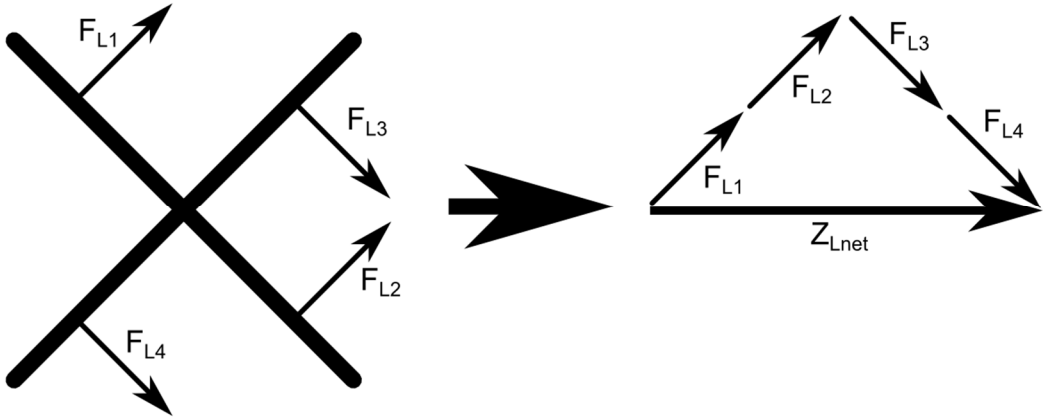


FIGURE 3.11 - X CONFIGURATION HYDROPLANES WITH NET HORIZONTAL FORCE

The stern planes were modelled using the same base dynamic model as the bow planes shown in Figure 3.9. However, unlike the bow planes, there are two sets of hydroplanes controlling three degrees-of-freedom which requires additional considerations. Assuming a separate control setpoint for both the pitch and the heading, a method to combine them was necessary. Mathematically, from Equation (3.1), the pitch command $\alpha_\psi$ should be added to both sets of hydroplane signals while, from Equation (3.2), the heading signal $\alpha_\theta$ should be added to one hydroplane signal and subtracted from the other. As such the equations for the signals to eachm of the hydroplanes would be:

$$\alpha_{a_1} = \alpha_\psi + \alpha_\theta \tag{3.3}$$

$$\alpha_{a_2} = \alpha_\psi - \alpha_\theta. \tag{3.4}$$

Using Equations (3.3) and (3.4), the model for the AUV stern planes is shown in Figure 3.12.

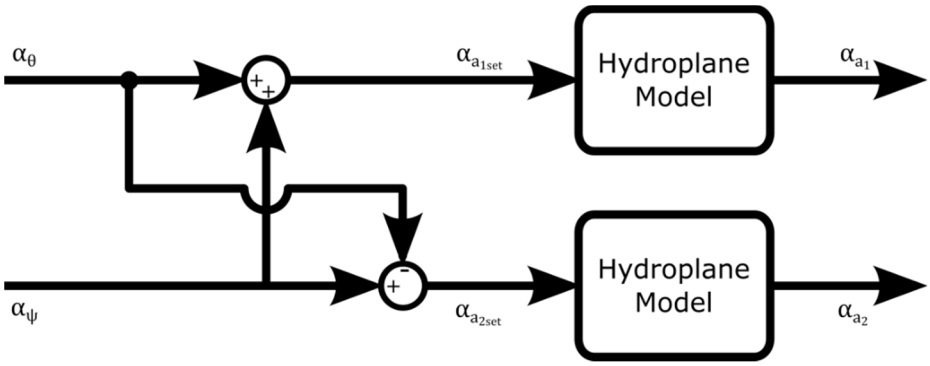


FIGURE 3.12 - STERN PLANE MODEL

It was assumed that perfect knowledge of pitch and heading is known to the AUV; however, a limitation of the SimMechanics toolbox is that attitude is only provided as a rotation matrix. For this model the Euler angles are required and must be calculated from the rotation matrix $R$. Defining the order of rotations to be yaw $R_\theta$, pitch $R_\psi$ then roll $R_\phi$ the combined rotation matrix would be defined as:

$$R = R_\theta R_\psi R_\phi. \tag{3.5}$$

Note that the following notation is used to simplify the equations in this section:

$$c* = \cos* \tag{3.6}$$

$$s* = \sin* \tag{3.7}$$

These rotation matrices in Equation (3.5) are then given as:

$$R_\theta = \begin{bmatrix} c\theta & 0 & s\theta \\ 0 & 1 & 0 \\ -s\theta & 0 & c\theta \end{bmatrix} \tag{3.8}$$

$$R_\psi = \begin{bmatrix} c\psi & -s\psi & 0 \\ s\psi & c\psi & 0 \\ 0 & 0 & 1 \end{bmatrix} \tag{3.9}$$

$$R_\phi = \begin{bmatrix} 1 & 0 & 0 \\ 0 & c\phi & -s\phi \\ 0 & s\phi & c\phi \end{bmatrix}. \tag{3.10}$$

Multiplying these three matrices in order gives:

$$R = \begin{bmatrix} c\psi c\theta & s\phi s\theta - c\phi c\theta s\psi & c\theta s\phi s\psi + c\phi s\theta \\ s\psi & c\phi c\psi & -c\psi s\phi \\ -c\psi s\theta & c\phi s\psi s\theta + c\theta s\phi & c\phi c\theta - s\phi s\psi s\theta \end{bmatrix} \tag{3.11}$$

From this resultant $R$ matrix the Euler angles can be calculated as:

$$\phi = -\tan^{-1}\frac{r_{23}}{r_{22}} \tag{3.12}$$

$$\theta = -\tan^{-1}\frac{r_{31}}{r_{11}} \tag{3.13}$$

$$\psi = \sin^{-1} r_{21} \tag{3.14}$$

where each "r" variable corresponds to an element in the $R$ matrix with the subscript denoting the row followed by the column number.

The control loop for the stern planes can be seen in Figure 3.13. The input to the controller are the heading $\theta$ and pitch $\psi$ which are taken from the AUV's rotation matrix $R$ using Equations (3.13) and (3.14). The value $\theta$ is deducted from the set value $\theta_{set}$ to give the error value $\theta_{err}$. This error is then given to the PID controller

which generates the desired deflection angle $\alpha_\theta$. Similarly, the $\psi$ value is subtracted from the command value $\psi_{set}$ to give the error value $\psi_{err}$. This value is then sent to the pitch PID controller to give the deflection angle $\alpha_\psi$. Within the hydroplane model these command signals are combined in the stern hydroplane model (Figure 3.12) at which point the deflection angles $\alpha_1$ and $\alpha_2$ are finally delivered to the AUV model.

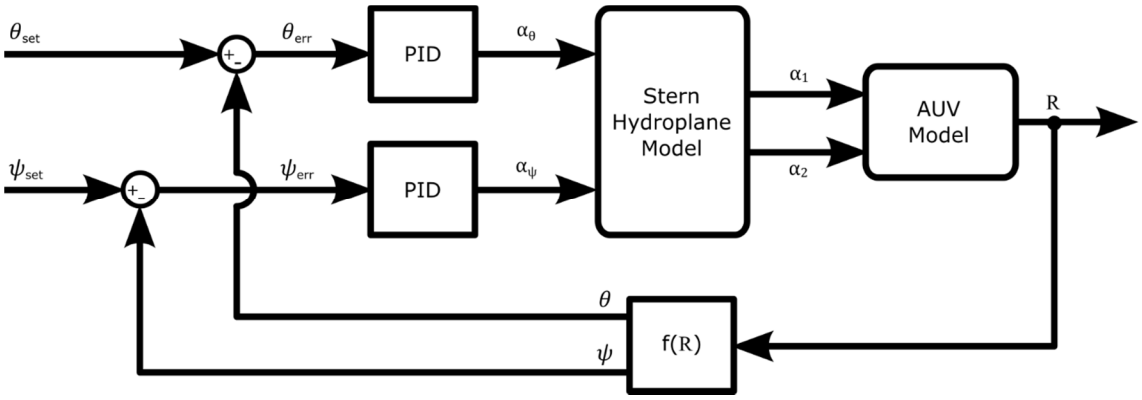


**FIGURE 3.13 - AFT HYDROPLANE CONTROL**

Use of the aft hydroplane controller can be seen individually controlling for a step input in the pitch in Figure 3.14 and the heading in Figure 3.15 in separate simulations.

The result of a step input for only the pitch command can be seen in Figure 3.14. Initially the command (dashed line) is set to neutral 0° and then is changed to 10° at 30 seconds and held. The subsequent dotted, dash-dot and solid lines are the responses of the P, PI and PID controllers, respectively, with the corresponding selected gains of P=1.5, I=0.05 and D = 4. Using just a proportional gain alone resulted in a steady-state error with overshoot. The addition of an integral term is seen to eliminate the steady state error and the derivative term is then seen to remove the overshoot. Selection of the PID controller with these gains resulted in achieving the desired set point within 20 seconds.

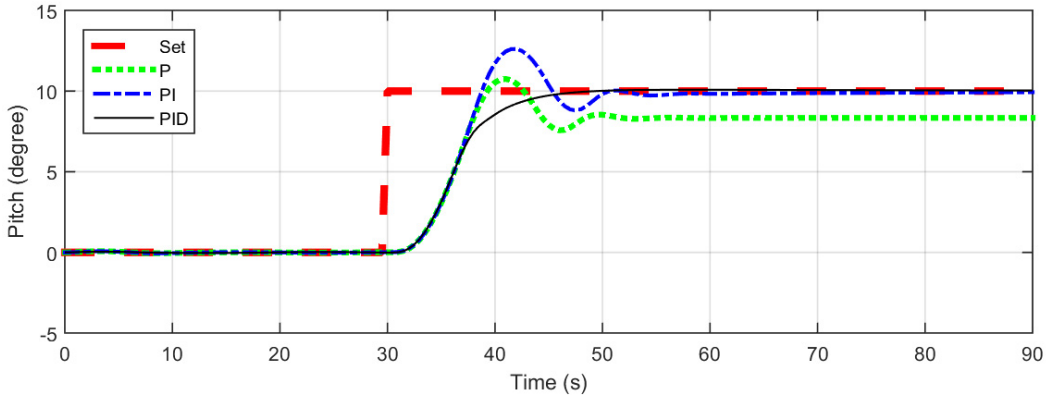


FIGURE 3.14 – AFT HYDROPLANE CONTROLLER PITCH STEP RESPONSES FROM 0 TO 10 DEGREES

The result of a step input to for a heading command from 0° to 10° at 30 seconds can be seen in Figure 3.15. Initially the command (dashed line) is set to 0° and then changes to 10° at 30 seconds. The subsequent dotted, dash-dot and solid lines are the responses of the P, PI and PID controllers, respectively, with the corresponding selected gains of P=3, I=0.1 and D = 3. Using just a proportional gain alone again resulted in a steady-state error with overshoot. Similar to the pitch step response, the addition of an integral term is seen to reduce the steady state error while the derivative term removes the overshoot resulting in the desired set point being achieved within 20 seconds.

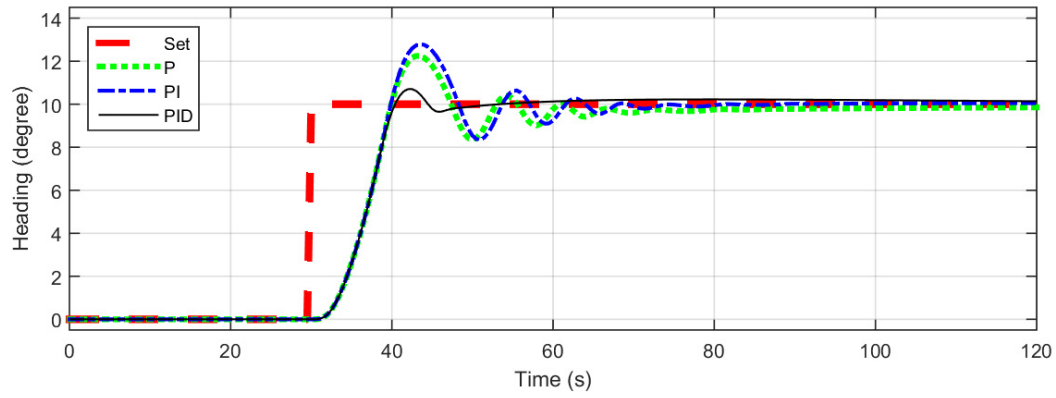


FIGURE 3.15 - AFT HYDROPLANE CONTROLLER HEADING STEP RESPONSES FROM 0 TO 10 DEGREES

## 3.4 Large Depth Change Control Strategy

The control strategy presented so far is acceptable for relatively small changes in AUV depth; however, for larger changes a different approach is typically required. For large changes it would be better to point the AUV toward the desired depth and use thrust to perform the bulk of the work.

Using this strategy, the use of bow planes is no longer required and they can simply be rotated to neutral. The set pitch angle $\psi_{set}$ would then be set either +45° to ascend -45° to descend. This fixed pitch angle was selected based on the typical limits that the AUV would be operated.

The transition depth threshold for switching between this control method and the previous was selected to be 50 m. Figure 3.16 shows the response of the AUV using this two-part control strategy to dive to 1000m. In this figure the feedback depth response of the AUV is shown as a solid line with the desired (set point) shown as a dashed line. With the step change in depth commanded at 30 seconds the AUV arrives at the new desired depth in less than 1100 seconds moving at a velocity $u$ of 1.5 m/s.

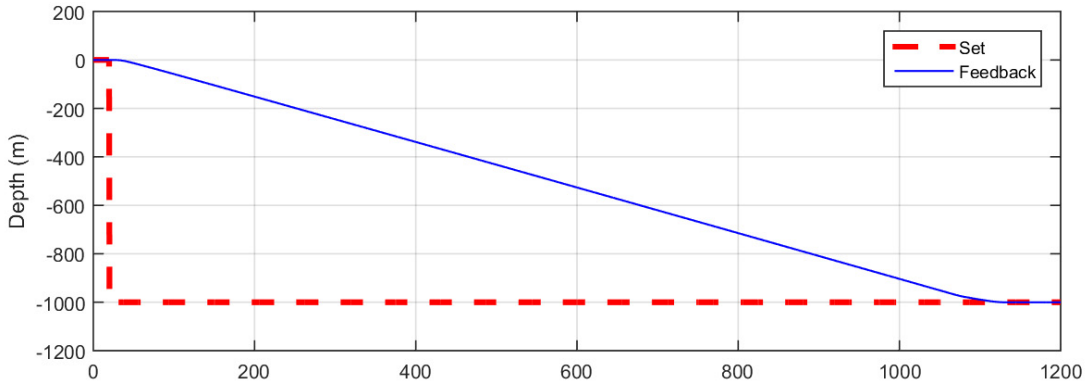


**FIGURE 3.16 - 1000M DEPTH STEP RESPONSE OVER TIME (S)**

The simulation results of this spiral dive can be seen in three dimensions in Figure 3.17. The top down view of the circular spiral descent can be seen in Figure 3.17 a) where X and Z represent the horizontal axes. Figure 3.17 b) and c) show the corresponding side

and front views, respectively, while the isometric view of the descent can be seen in Figure 3.17 d).

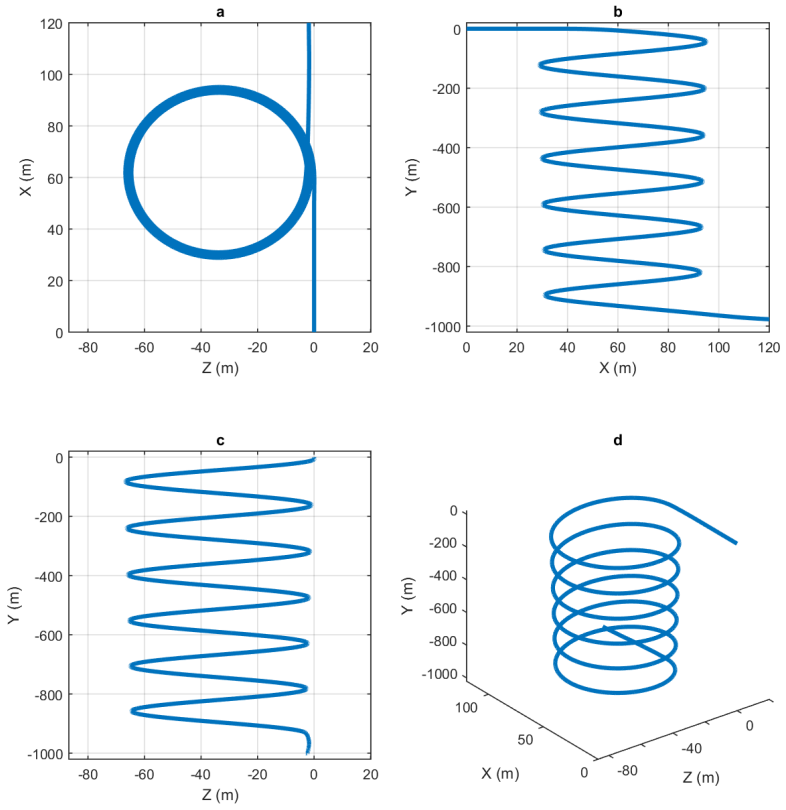


FIGURE 3.17 - 1000M DEPTH STEP RESPONSE IN 3D

## 3.5 Waypoint Following

Finally, a waypoint-following algorithm [19] was implemented to enable the AUV to traverse a series of waypoints. The algorithm selects the next waypoint when the AUV has either arrived at the desired location or has come to within a threshold of the waypoint.

The first calculation in this algorithm determines the desired heading angle $\theta$. Referring to Figure 3.18, this angle can be calculated from the difference in the AUV's position $(x, z)$ and the next waypoint location $(x_i, z_i)$. The equation for $\theta$ would be given as:

$$\theta = \text{atan}\left(\frac{\Delta Z}{\Delta X}\right) \tag{3.15}$$

where:

$$\Delta X = x_i - x \tag{3.16}$$

$$\Delta Z = z_i - z \tag{3.17}$$

and:

$x$ = x position of AUV

$z$ = z position of AUV

$x_i$ = x position of i[th] waypoint

$z_i$ = z position of i[th] waypoint

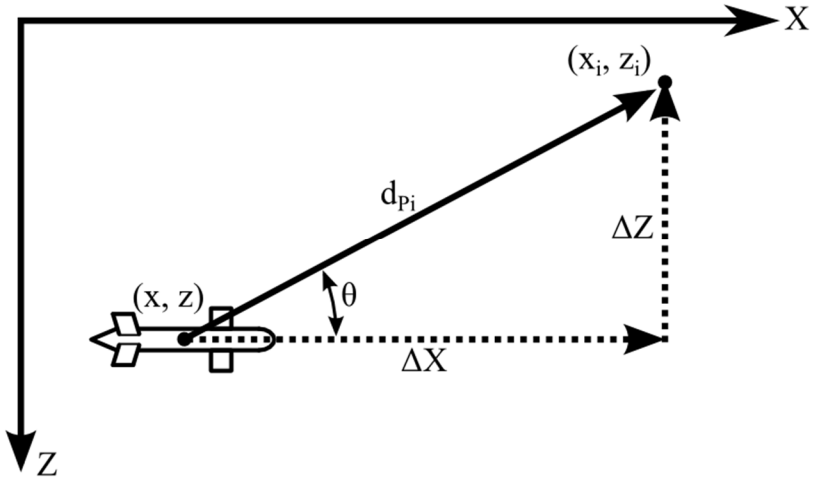


**FIGURE 3.18 - DEFINITION OF WAYPOINT COORDINATES**

With this algorithm there are two different conditions which permit the heading control to switch to the next waypoint. The first condition corresponds to when the AUV has achieved a minimum distance threshold $r_0$ of twice the vehicle length from the waypoint, as suggested in Bakaric et al. [19], and is considered to have hit or 'acquired' the waypoint when:

$$d_{P_i} \leq r_0 \tag{3.18}$$

where the distance $d_{P_i}$ to the i[th] waypoint is calculated as:

$$d_{P_i} = \sqrt{\Delta X^2 + \Delta Z^2}. \tag{3.19}$$

The second condition which enables the AUV to switch to the next waypoint occurs when the AUV has come as close as it will and is within a maximum acceptable distance $r_1$. This situation occurs when both Equations (3.20) and (3.21) are satisfied.

$$d_{P_i} > d_{min} \tag{3.20}$$

$$d_{P_i} \leq r_1 \tag{3.21}$$

where:

$d_{min}$ = closest distance the AUV came to the current waypoint.

An example of acquiring a waypoint is shown in Figure 3.19. In this figure the outer dashed circle shows the radius $r_1$ which defines the "close enough" zone and the inner dotted circle or radius $r_0$ represents the hit zone. The small circle in Figure 3.19 (labelled "Waypoint Achieved") corresponds to where the AUV direction vector intersects the dotted $r_0$ circle and indicates the point at which the algorithm considers the waypoint to have been achieved or acquired.

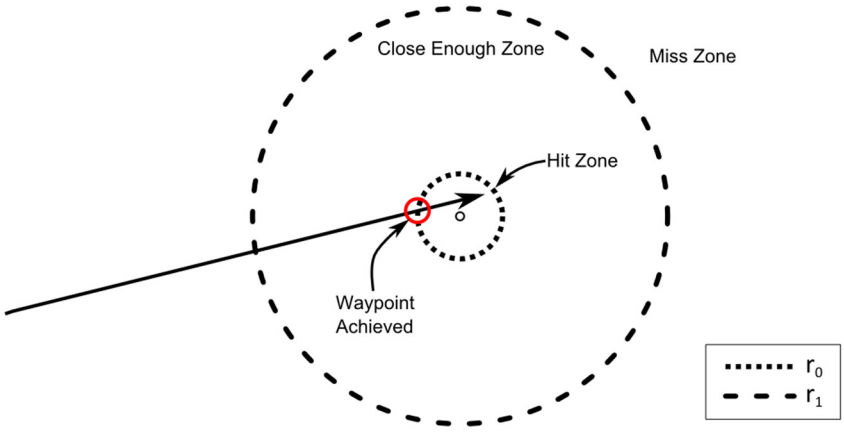


FIGURE 3.19 - ACHIEVING WAYPOINT

When the AUV arrives within the radius $r_1$ of the current waypoint the algorithm checks to see whether or not the AUV is now moving away – indicating that the waypoint will not be achieved. If true, the algorithm would then select the next waypoint rather than guiding the AUV to attempt a second pass. An example of coming "close enough" to a waypoint is observed in Figure 3.20. The inner and outer circles once more indicate the hit and miss radius as seen in Figure 3.19. In this case the small circle intersecting the AUV direction vector in Figure 3.20 indicates where the AUV achieved its minimal distance to the waypoint and began to move way. Since this point was within the radius $r_1$ the next way point would be selected rather than making the AUV circle back to try again – a maneuver which would be limited by the minimum turn diameter possible with the AUV at-speed.

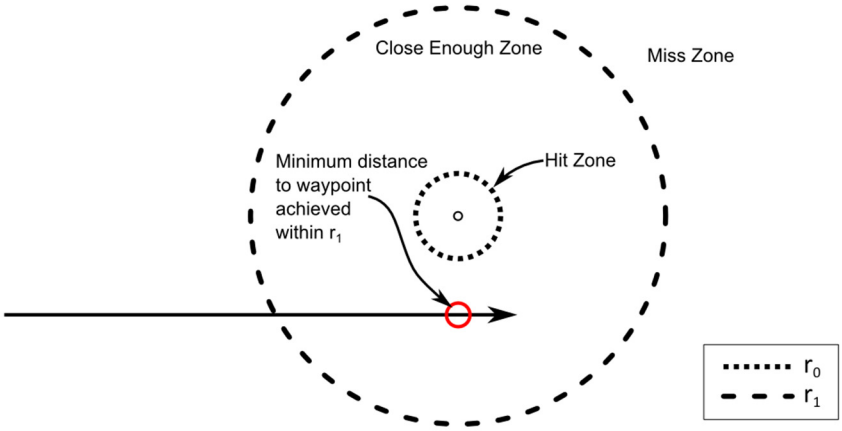


FIGURE 3.20 - CLOSE ENOUGH TO WAYPOINT

A typical route for an AUV is to follow a grid search pattern which tracks a series of parallel lines much like a lawnmower path. One simulation example of such a path can be seen in Figure 3.21 where the vessel travels at velocity $u$ = 2m/s. In the figure the path followed by the AUV is shown as a solid line while the individual waypoints are indicated by the double circle. These circles indicate the hit (inner circle) and miss

(outer red circle) regions for each of the waypoints. As can be seen in the figure the AUV manages to enter the hit region for each waypoint in every case.

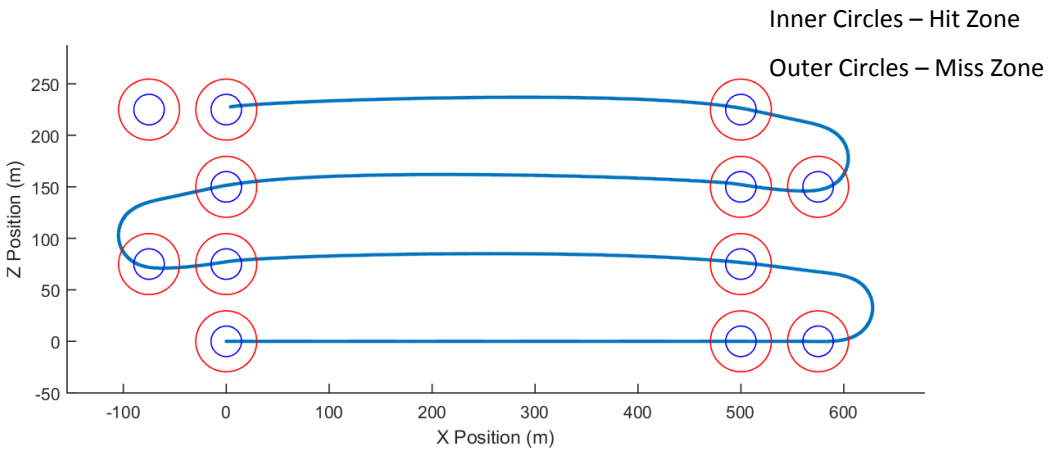


**FIGURE 3.21 - AUV FOLLOWING LAWNMOWER PATTERN SERIES OF WAYPOINTS**

# Chapter 4: VBS Model

Having successfully developed a 3D simulator of an AUV with hydroplane control, a variable ballast system (VBS) was then developed. A VBS differentiates itself from other forms of ballast control in that it has the ability to actively and reversibly change the vehicle's buoyancy. Other forms of ballast control include fixed ballast where weights are added to adjust towards neutral buoyancy and level trim at launch – which still leaves the AUV susceptible to underway buoyancy variations due to hull compression and water density. Another ballast system is the drop weight which can actively make the vehicle positively buoyant by releasing a mass – but such a ballast system is irreversible[15]. The benefit of including a VBS in the design of a submerged vehicle is that VBS permits the AUV to overcome the limitations of fixed and irreversible ballast schemes with the additional benefit of potentially setting non-neutral buoyancy and non-zero trim as needed.

There are a many potential configurations for VBS. Examples range from movable piston systems, oil-filled expandable bladder systems and seawater ballast systems as discussed in Carroll [2]. For the purpose of this thesis, a seawater Variable Ballast System with a regulated high pressure air supply shall be the assumed configuration – similar to that used by Woods [10].

A schematic of the VBS design used for this thesis is shown in Figure 4.1. Items numbered ① to ⑤ operate on the water (wet) side having direct contact with, and control of, the amount of seawater in the VBS system. The balance of components numbered ⑥ to ⑨ operate on the air (dry) side, with VBS tank number ① being the junction between the air side and the water side where the tank pressure is controlled. Referring to Figure 4.1, the complete list and description of each of the VBS system components are as follows:

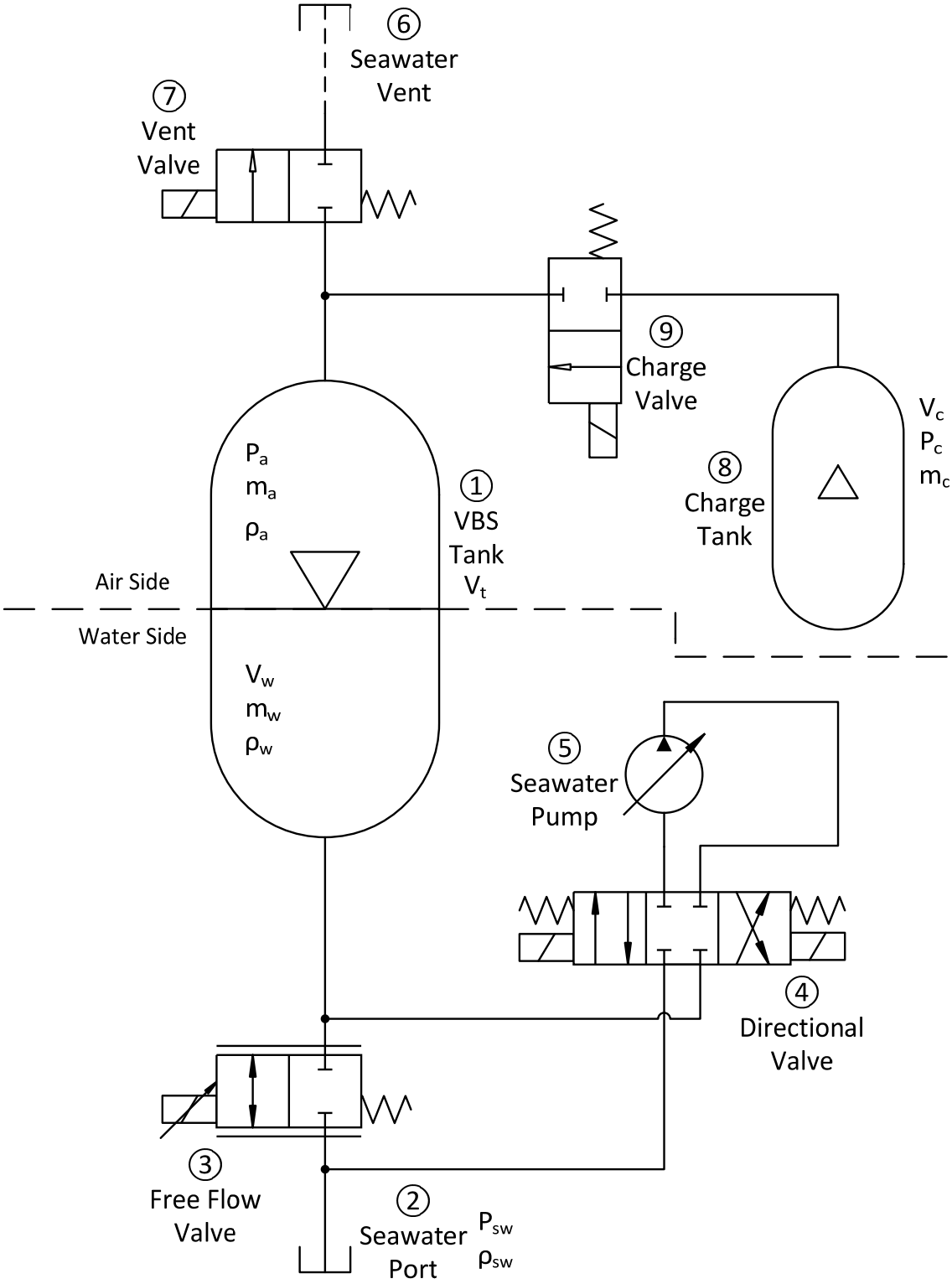


FIGURE 4.1 - VBS SCHEMATIC OF SYSTEM USED FOR THIS THESIS

1. **VBS Tank**

   This tank of volume $V_t$ is the junction between the air and water sides of the VBS. Water volume $V_w$ is controlled by other system components with their mass and density being denoted as $m_w$ and $\rho_w$, respectively. Pressure in the tank is regulated by the air pressure $P_a$ which has a mass $m_a$ and density $\rho_a$.

2. **Sea Water Port**

   This port is the access point for seawater to enter or exit the system. Seawater pressure $P_{sw}$ and density $\rho_{sw}$ are functions of the current AUV depth.

3. **Free Flow Valve**

   This valve facilitates the connection between seawater port ② and VBS tank ①. Proportional control permits water to freely flow amongst the two locations at varying rates between the fully-closed and fully-opened states.

4. **Directional Valve**

   This valve connects pump ⑤ to the rest of the system. When disabled in the center position, the valve is closed permitting no flow. Shifted to the right, the valve would permit the pump to draw from the seawater port into VBS tank ①, while shifting the valve to the left would reverse this process allowing flow in the opposite direction into seawater port ②.

5. **Seawater Pump**

   This pump is used to direct flow of water into or out of VBS tank ① with the direction determined by Directional Valve ④.

6. **Seawater Vent**

   This vent is used to purge excess air out of the system when vent valve ⑦ is opened.

7. **Vent Valve**

This valve is used to release air out of the system through seawater vent ⑥ when pressure in VBS tank ① is too high.

8. **Charge Tank**

   This tank of volume $V_c$ is filled with a mass of air $m_c$ of pressure $P_c$ which is used to increase the pressure in VBS tank ① as necessary.

9. **Charge Valve**

   When open, this valve permits flow of air from charge tank ⑧ to VBS tank ①.

There being two sides (air and water) for control of this VBS configuration, each side has its own control system. On the seawater side there are two modes for moving the liquid into and out of the VBS tank:

1. **Pump assisted flow**

   In this mode, the direction of flow is controlled by directional valve ④ and the flow itself is based on the displacement and speed of pump ⑤.

2. **Free Flow**

   This mode is reliant entirely on the differential pressure between the air pressure $P_a$ in tank ① and the seawater pressure $P_w$ at seawater port ②. This difference in pressure determines both the direction and rate of flow when the free flow valve is opened.

On the air side of the system there are again two more functions:

1. **Tank Air Charging**

   This function releases the high pressure air $P_c$ in charge tank ⑧ to pressurize the main VBS tank ① by opening charge valve ⑨.

2. **Venting Tank Air**

   This function releases air from VBS tank ① out of the system reducing the tank pressure $P_a$ by opening vent valve ⑦.

## 4.1 Elements of a VBS Model

In developing a computer model of this VBS it is important to first address its primary purpose in an AUV is to change the net buoyancy. There being two ways to affect buoyancy changes (either through the volume of displaced water or the system mass) the latter was selected. The total mass can be modified by the flow of air and water in or out of the system. These flows are, in turn, affected by the volume, pressure and density of the fluids in motion; therefore, to model the VBS it is necessary to calculate the following characteristics:

- Volume
- Flow Rates
- Mass
- Pressure

### 4.1.1 Volumes

The volume of VBS tank ① was assumed to be 60L. This volume was selected as it corresponds to the highest lift force of one set of hydroplanes where the Arctic Explorer AUV is moving at its published cruising speed of 2 m/s. Additionally, this volume also equates to a sphere of radius 0.25 m which is less than the radius of the AUV body making it a feasible size. Thus the VBS tank volume is given as:

$$V_t = 60\ L. \tag{4.1}$$

The corresponding charge tank volume was simply assumed to be 50% the size of the main tank as follows:

$$V_c = 30\ L. \tag{4.2}$$

The limits now established for the tank size and instantaneous volume of water can then be calculated as the initial amount plus the sum of the flow into the tank minus the flow out. As such, the volume of water $V_w$ in the tank is given as:

$$V_w = V_{w_0} + \int Q_{in} - \int Q_{out} \tag{4.3}$$

where:

$Q_{in}$ = flow of water going into the VBS Tank ①

$Q_{out}$ = flow of water going out of the VBS Tank ①.

The corresponding volume of the air in the tank $V_a$ would then be the remaining space in the tank calculated as:

$$V_a = V_t - V_w. \tag{4.4}$$

### 4.1.2 Pump Flow

The traditional mechanism for VBS water flow is to use positive displacement axial piston pumps [3], [11], [20]. The pump flow rate $Q_p$ can be calculated as:

$$Q_p = \eta_v \, Q_{p_{100}} \, n \tag{4.5}$$

where:

$\eta_v$ = volumetric efficiency as a function of the pressure difference between pump inlet and outlet

$Q_{p_{100}}$ = full capacity 100% efficiency flow rate

$n$ = load level (0-100%).

In Liu et al. [11] it was shown that volumetric efficiency at zero load for the pump is approximately 80% and decreased by 10% at 5 MPa. Assuming a linear relationship for the pressure range the AUV is operated in, this relationship would result in the volumetric efficiency being calculated as:

$$\eta_v(P) = 80 - 10(P/5\ MPa)\ \%. \tag{4.6}$$

The operating flow rate for the pump varies in the literature from Woods [10] at V = 3 L/min up to Liu et al. [11] at V = 25 L/min. The selected rate $Q_{p_{100}}$ for this thesis was 5 L/min permitting the VBS tank to be completely filled or emptied in 15 minutes at the surface with a 80% volumetric efficiency.

### 4.1.3 Pressures

The pressures of note for the VBS are:

- VBS tank pressure $P_a$
- Charge tank pressure $P_c$
- Seawater pressure $P_{sw}$

The first two pressures generated by air can be determined from the ideal gas law [21]:

$$P = \frac{mRT}{V} \tag{4.7}$$

where:

$R$ = Specific gas constant for air 286.9 J/kgK

$T$ = Assumed constant temperature (5 C or 278 K).

Substituting the appropriate volume $V_c$ and mass $m_c$ into Equation (4.7), the charge pressure becomes:

$$P_c = \frac{m_c RT}{V_c} \tag{4.8}$$

and substituting $V_a$ and $m_a$, the air pressure in the VBS tank is given as:

$$P_a = \frac{m_a RT}{V_a}. \tag{4.9}$$

Finally, the seawater pressure $P_{sw}$ which is calculated based on density, depth and gravity can be given as:

$$P_{sw} = -\rho_{sw}\, y\, g \tag{4.10}$$

where:

$\rho_{sw}$ = density of seawater [kg/m$^3$]

$y$ = depth [m]

$g$ = acceleration due to gravity (9.81 m/s$^2$)

### 4.1.4 Free flow

Flow due to differences in pressure can be calculated using Bernoulli's equation given as:

$$Q = C\ Y\ A_2 \sqrt{\frac{2\Delta P}{\rho_1}}\ [22] \tag{4.11}$$

where:

$Q$ = flow rate

$C$ = orifice coefficient

$A_2$ = cross sectional area of downstream orifice hole

$\Delta P$ = pressure across orifice

$\rho_1$ = upstream fluid density

$Y$ = 1 for water and 3.5 for air.

For incompressible fluids such as water, Y=1; however, for compressible fluids like air Y is defined as:

$$Y = \frac{k}{k-1} \tag{4.12}$$

where k is the specific heat ratio $C_p/C_v$ for the fluid. For air, k=1.4 resulting in a value of Y=3.5 [22].

For a compressible fluid like air, mass rather than volume is more important to track since volume can vary with both pressure and temperature. To calculate mass flow rate $\dot{m}$ the volumetric flow can be multiplied by the upstream fluid density $\rho_1$ giving:

$$\dot{m} = C\ Y\ A_2 \sqrt{2\ \rho_1\ \Delta P}. \tag{4.13}$$

With pump flow as defined in Equation (4.5) there are still three of the four flow modes left to define. However, since the free-flow mode can occur in two directions, Equation (4.11) must be evaluated separately for the fill and empty conditions. Thus, referring to the schematic of the system shown in Table 4.1, there are four pressure-related flow modes as follows:

**Free Fill** The flow rate $Q_{in}$ adds to the volume of water in VBS tank ① and is only possible when $P_{sw} > P_a$ and free flow valve ③ is open.

**Free Empty** The flow rate $Q_{out}$ reduces the volume of water in VBS tank ① and is only possible when $P_{sw} < P_a$ and free flow valve ③ is open.

**Charge Air** The mass flow rate of air $\dot{m}_c$ flows from the charge air tank and into the VBS tank and it only works when $P_c > P_a$

**Vent Air** The mass flow rate of air $\dot{m}_a$ exits the VBS tank

The values and variables used to calculate flow for each of these states using Equations (4.11) and (4.13) can be seen in Figure 4.1.

**TABLE 4.1 - FLOW RATE VARIABLES**

| STATE | C | $A_2$ | Y | DENSITY $\rho_1$ | PRESSURE DIFFERENCE |
|---|---|---|---|---|---|
| **FREE FILL** | 0.6 | 1.5E-4 $m^2$ | 1 | $\rho_{sw}$ | $P_w - P_a$ |
| **FREE EMPTY** | 0.6 | 1.5E-4 $m^2$ | 1 | $\rho_t$ | $P_a - P_w$ |
| **CHARGE AIR** | 0.6 | 3.0E-5 $m^2$ | 3.5 | $\rho_c$ | $P_c - P_a$ |
| **VENT AIR** | 0.6 | 3.0E-5 $m^2$ | 3.5 | $\rho_a$ | $P_a - P_w$ |

where:

$\rho_{sw}$ = sea water density at current depth

$\rho_t$ = water density in the VBS tank

$\rho_c$ = density of air in charge tank

$\rho_a$ = density of air in VBS tank

Substituting the variables from Table 4.1 for the water flow modes into Equation (4.11) gives:

$$Q_{in} = CA_2\sqrt{2\ (P_{sw} - P_a)/\rho_{sw}} \tag{4.14}$$

$$Q_{out} = CA_2\sqrt{2\ (P_a - P_{sw})/\rho_t}. \tag{4.15}$$

Similarly, substituting the variables from Table 4.1 for the air mass flow into Equation (4.13) gives:

$$\dot{m}_c = CYA_2\sqrt{2\,\rho_c\,(P_c - P_a)} \tag{4.16}$$

$$\dot{m}_a = CYA_2\sqrt{2\,\rho_a\,(P_a - P_{sw})}. \tag{4.17}$$

In the case of venting there is an interaction between air and seawater which is not fully modelled by these calculations. However, as this function is not a major feature in operation of the VBS this simplification was acceptable for the purpose of this research.

### 4.1.5 Mass

Similar to volume, the mass of air can be determined with the mass flow rates defined in Equations (4.16) and (4.17). Mass of air in the VBS tank $m_a$ will always be the initial amount plus the sum of the mass flow into the tank from the charge tank $\dot{m}_c$ minus the sum of the flow vented out $\dot{m}_v$ which gives:

$$m_a = m_{a_0} + \int \dot{m}_c - \int \dot{m}_v. \tag{4.18}$$

The charge tank, only having flow out $\dot{m}_c$, would then be given as:

$$m_c = m_{c_0} - \int \dot{m}_c. \tag{4.19}$$

Mass of water $m_w$ can similarly be calculated; however, the density of the source of flow must be used to calculate the mass flow rate; therefore, the calculation for water mass would be given as:

$$m_w = m_{w_0} + \int \rho_{sw}\,Q_{in} - \int \rho_w\,Q_{out}. \tag{4.20}$$

Finally, the total of these three values would account for the total variable mass of the VBS $m_t$ given as:

$$m_t = m_w + m_a + m_c. \tag{4.21}$$

Knowing both the mass and volume it is possible to then calculate pressure with the ideal gas law.

## 4.2 Integration with AUV model

With the model determined for the VBS it was still necessary to integrate this into the AUV model. This integration was facilitated by physically modelling two separate VBS as variable point masses in SimMechanics. The locations where these masses were applied in the AUV are show in Figure 4.2 as points **ab** and **fb** which are located at distances $l_{ab}$ and $l_{fb}$ from the origin O (located at the geometric centre of the assumed circular cylinder AUV), respectively.

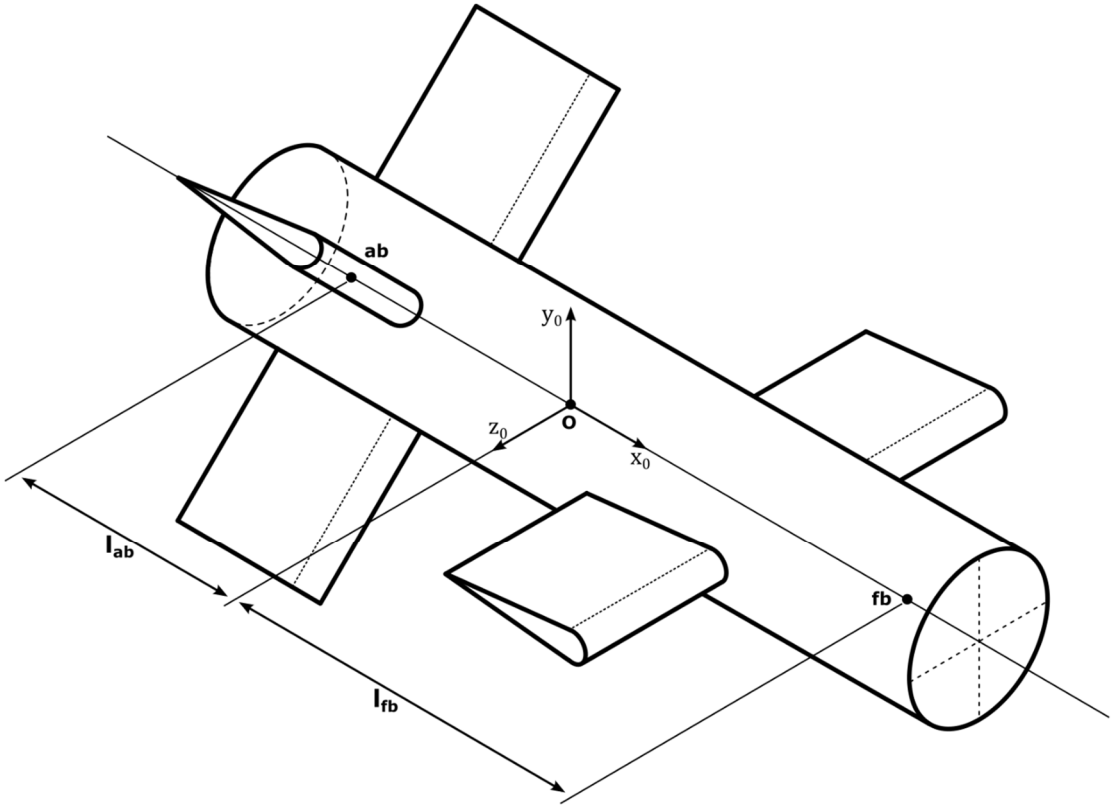


**FIGURE 4.2 - LOCATION OF BOW AND STERN VBS**

Validation of the VBS model is discussed in Appendix B:. With a model of the AUV system complete it is now necessary to develop a corresponding VBS power consumption model and control scheme.

## 4.3 VBS Power Consumption

There are two main consumers of power in the VBS – the pump and the valves.

The power output of the pump in terms of the power required for the pumped water can be calculated as:

$$P_{out} = Q\ \Delta P\ n \tag{4.22}$$

where:

$Q$ = the full flow rate

$\Delta P$ = the pressure gradient across the pump

$n$ = the load level of the pump

In terms of the power being put into the pump from the AUV the output power can be given as:

$$P_{out} = \eta_t\ P_{in} \tag{4.23}$$

where:

$\eta_t$ = total efficiency of the propulsion system

$P_{in}$ = power input to the propulsion system

Equating the two equations (4.22) and (4.23) gives the input power from the AUV as:

$$P_{in} = \frac{Q\ \Delta P\ n}{\eta_t} \tag{4.24}$$

Power consumption of the valves was simply assumed to be 25 W when in operation. This value corresponds to the power consumption of typical submersible solenoid valves (e.g. Hydracon subsea valves [23]). If any of the free-flow valves, directional valves, charge valves or vent valves were in operation, 25 W of power would be added for each.

Additionally, it was assumed that the minimum power consumed by the pump would be 25 W when it is operating. This value was selected to be an appropriate minimum coinciding with the valve power ultimately requiring twice as much power to be used

when the pump is enabled as a valve ④ needs to be enabled with the pump ⑤ to provide direction.

# Chapter 5: VBS Control

This chapter discusses the control of the VBS including:

1) Internal control of the water side and air side of the VBS
2) Control of the VBS mass using these internal controls
3) Depth control of the AUV using only VBS control
4) Pitch control of the AUV using only VBS control

The purpose of the internal controls is to regulate the volume of water in the VBS tank. In turn the mass can be set and the resulting VBS force $F_{vbs}$ is applied to the AUV. This VBS force is the net buoyancy force which is the upward displacement force $F_\Delta$ less the gravity force $F_g$, which can be calculated as:

$$F_{vbs} = F_\Delta - F_g \tag{5.1}$$

$$F_\Delta = \rho\, g\, V_{vbs} \tag{5.2}$$

$$F_g = (m_{vbs} + m_w + m_c)g. \tag{5.3}$$

Recalling the schematic of the system shown in Figure 4.1 these values are given as:

$\rho$ = density of water (kg/m$^3$)

$g$ = acceleration due to gravity (9.81 m/s$^2$)

$V_{vbs}$ = volume of water displaced by the VBS

$m_{vbs}$ = mass of the VBS without air or water

$m_w$ = mass of water in VBS tank ① (see Equation (4.21))

$m_c$ = mass of air in VBS charge tank ⑧

A demonstration of the net buoyancy force $F_{vbs}$ at different levels of water in the VBS tank is illustrated in Figure 5.1. The VBS, for example, can be set to neutral buoyancy when it is filled to 50% with water as shown in Figure 5.1 a), where the forces of gravity $F_g$ and displacement $F_\Delta$ are equal resulting in a buoyancy force $F_{vbs}$ of zero. Increasing the volume of water in the tank, as in Figure 5.1 b), results in an increase in the mass and the force of gravity $F_g$ which exceeds the displacement force $F_\Delta$. This larger force $F_g$ consequentially causes the net buoyancy force $F_{vbs}$ to be negative. Conversely, reducing

the volume of water in the tank results in a smaller gravity force and a net positive buoyancy force $F_{vbs}$ as seen in Figure 5.1 c).

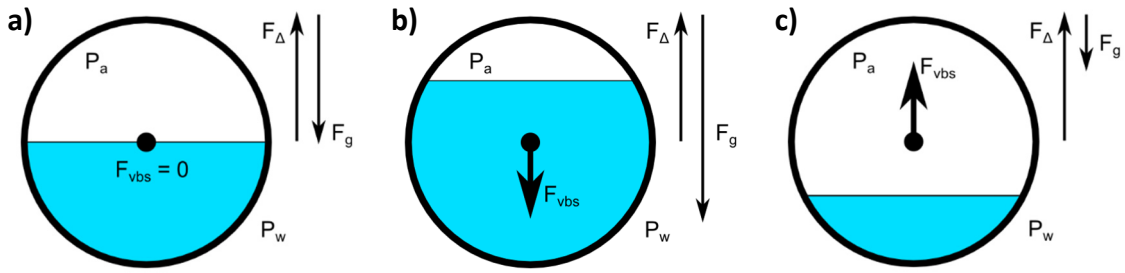


**FIGURE 5.1 - VBS NET BUOYANCY FORCE WITH TANK FILLED TO a) 50%, b) 75%, AND c) 25%**

## 5.1 Water Control

For this thesis the displacement force $F_\Delta$ and the effect of the VBS system mass $m_{vbs}$ are incorporated into the AUV model. Additionally, to simplify notation, the mass of air $m_a$ in the VBS is omitted as it is assumed to be insignificant in relation to the mass of water. The result is that the applied force can be given as:

$$F_{vbs} = m_w\, g. \tag{5.4}$$

From the VBS model in Chapter 4 (Figure 4.1) there are two methods to directly control its mass. These are:

- **Pump Control**: Enable Pump ⑤ (from Figure 4.1) and shift Directional Valve ④ to permit the water to flow in the desired direction at a fixed rate.
- **Free Flow**: Open Free Flow Valve ③ to permit water to flow as determined by the difference between the pressures $P_a$ and $P_w$.

The actions that can be taken with these functions are:

1) **No Flow (NF)**: Both valves (Directional ④ and Free Flow ③) are closed and Pump ⑤ is disabled.
2) **Open Free Flow Valve (FF)**: Free Flow Valve ③ is shifted between partially and fully open permitting flow between VBS Tank ① and Seawater Port ②. The

proportional amount this valve is opened depends on the magnitude of the command signal **sig** having a value from 0% to 100% open.

3) **Pump into Tank (P+)**: Directional Valve ④ is shifted to permit flow into Tank ① from Seawater Port ② and Pump ⑤ is enabled. The command signal **sig** is used by this function to determine the output level of the pump as a percentage of maximum output.
4) **Pump Out of Tank (P-)**: Same as state P+, however, position of Directional Valve ④ is shifted to the opposite side permitting the pump to drive flow out of the tank

The free flow **FF** function, unlike the other three, results in a variable flow rate and direction dependant on the relationship between water pressure $P_{sw}$ and air pressure in the tank $P_a$. This pressure difference can be given as:

$$\Delta P = P_{sw} - P_a. \tag{5.5}$$

When this pressure difference is positive, water would naturally flow into the lower pressure tank and, when negative, water would flow out of it.

Figure 5.2 compares the results of using free flow vs the pump to try to fill the ballast tank in the presence of a pressure difference ΔP varying from -10 MPa to 10 MPa. It can be seen from this figure that, over the entire range of pressures, the pump flow direction, shown as a solid line, is always positive and relatively constant. The free flow rate, given as a dotted line, varies greatly with pressure ΔP. At large values of ΔP the free flow rate becomes greater than when pumping; however, for smaller positive values the flow rates drop below that of the pump and eventually reach zero. Additionally, when the pressure difference reverses (i.e. $\Delta P < 0$) the flow direction also reverses.

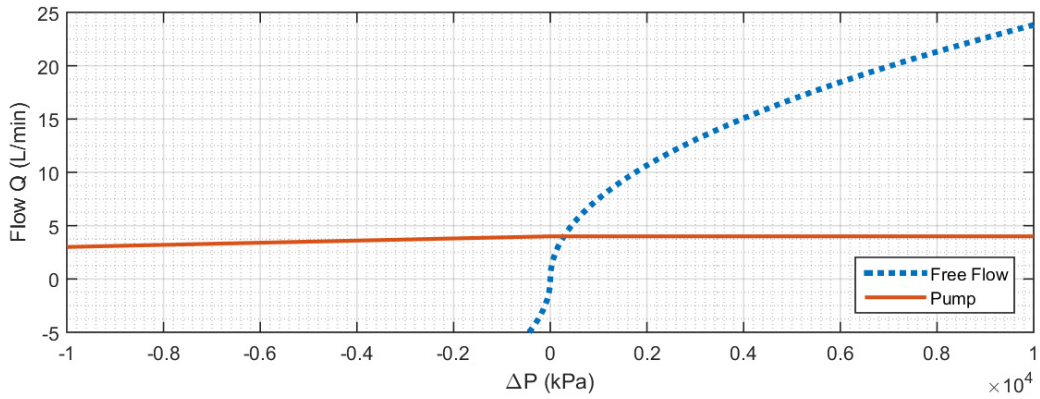


**FIGURE 5.2 - VBS FLOW RATES FOR PUMPED AND FREE FLOW STATES FOR PRESSURES FROM -10 MPA TO 10 MPA**

Figure 5.3 shows the flow rates for both pumping and free flow at a smaller range of pressures ΔP between 0 and 500 kPa. The pump flow rate can be seen to remain at 4 L/min while the rate for free flow is shown to vary from zero up to just over 5 L/min crossing the pump rate around ΔP = 275 kPa.

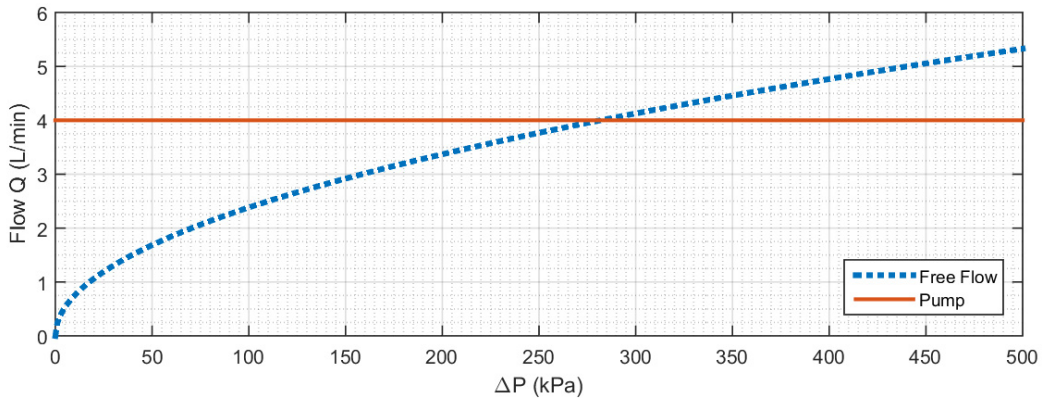


**FIGURE 5.3 - VBS POWER AND FLOW FROM PUMPED AND FREE FLOW AT ΔP PRESSURES FROM 0 TO 500 kPa**

From these observations it can then be understood that:

- Pumping is the only solution when a positive signal **sig+** is given to the VBS and the pressure in the tank $P_a$ is greater than the water pressure $P_{sw}$

- Free flow provides a higher flow rates than pumping when the system is commanded to fill the tank and a large positive pressure difference is present (e.g $\Delta P \geq 275$ kPa)
- Pumping provides better performance when the pressure difference is too small to yield large flow rates from free flow (e.g. $\Delta P < 275$ kPa).

The same pattern can be observed, not surprisingly, when reversing the direction of flow and these observations are summarized in Table 5.1. The left column of the table indicates the command signal **sig**. When **sig** is a positive value **sig+** it commands water to flow into the tank. When **sig** is a negative value **sig-** it commands water to flow out of the tank. The top two rows indicate the magnitude and direction of the differential pressure $\Delta P$ as one of largely positive ++ ($\Delta P > 275$ kPa), positive +, negative -, and largely negative -- ($\Delta P < 275$ kPa). In the table **FF** denotes free flow, **P+** corresponds to positive pumping while **P-** indicates negative pumping.

**TABLE 5.1 - WATER FLOW CONTROL SELECTION**

| | | ΔP | | | |
|---|---|---|---|---|---|
| | | **++** | **+** | **-** | **--** |
| sig | **+** | FF | P+ | P+ | P+ |
| | **-** | P- | P- | P- | FF |

The corresponding waterside control flow chart is show in Figure 5.4. Assuming an input signal **sig** with a value between positive and negative 100%, the first step determines if the command signal **sig** exceeds a minimum threshold appropriate for the system to react and, if not, then the no flow **NF** action is selected. Otherwise, the desired direction of the flow is then assessed; if the signal is positive **sig+** then the desired direction is to fill the tank, otherwise the signal would be negative **sig-** with the corresponding desired result being to empty the VBS Tank. If the direction is determined to be filling and if $\Delta P$ is largely positive then **FF** is selected. If this is not the case then the VBS is set to **P+**. If, rather, the direction selected is emptying and $\Delta P$ is

largely negative then **FF** is set, otherwise it is set to **P-**. In each case where an action other than no flow **NF** is selected, the magnitude of the command signal **sig** is used to establish the corresponding magnitude of the response whether it be to pump water in (**P+**), pump water out (**P-**), or open the valve (**FF**) in proportion to **sig**.

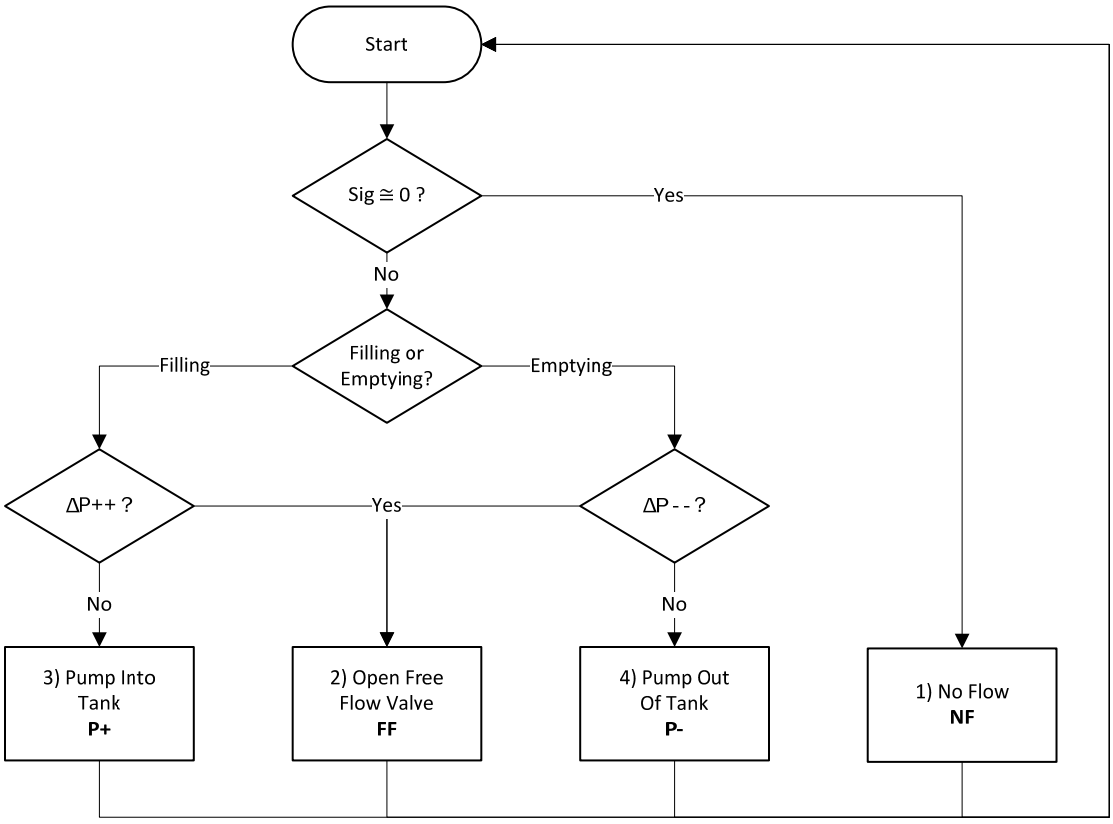


**FIGURE 5.4 - WATER FLOW CONTROL**

## 5.2 Air Pressure Control

An additional function included in the VBS is air pressure control as previously discussed in Chapter Chapter 4:. Although this function has a minimal effect on the overall mass of the system, it can be used to reduce the power required for water to be added or removed. This reduction in energy consumption is achieved by increasing the tank pressure so that free flow is possible or by venting high pressures acting against the pump. The available functions to control air pressure are (Figure 4.1):

1) **Null Air (NA):** No valves are activated.

2) **Vent Air (VA)**: Reduce the pressure in Tank ① by opening Vent Valve ⑦
3) **Charge Air (CA)**: Increase the pressure in the tank by opening Charge Valve ⑨ releasing air into the VBS tank from Charge Tank ⑧.
4) **Regen Air (RA)**: Increase charge pressure $P_c$ by opening Charge Valve ⑨ allowing high pressure air from VBS Tank ① to flow into Charge Tank ⑧.

Four modes where these functions are used include:

1) **Static Volume**: Disable Charge Valve ⑨ and Vent Valve ⑦ resulting in the VBS operating as it would without the Charge Tank ⑧.
2) **Expanded Volume**: Open Charge Valve ⑨ permitting the VBS to use Charge Tank ⑧ as extra volume in which air can compress and expand.
3) **High Pressure Air Assist**: Charge air is used to maintain an air pressure slightly higher than the water pressure to minimize power consumption.
4) **Regenerative Pressure Air Assisted**: Operates similar to the High Pressure Air Assist mode but includes the capacity to regenerate charge air pressure $P_c$ when the tank air pressure $P_a$ is higher.

The static volume mode was selected as a baseline against which the benefits of the other three modes could be compared. There is no direct cost for operating in static mode; however, tank air pressure can vary greatly with the volume of water in it. Figure 5.5 shows three potential volume levels for water in the VBS all assuming the same mass of air in the tank. Referring to Figure 5.5 a), the tank is half full of water leaving 50% of the volume $V_1$ filled with air. In Figure 5.5 b), the tank is 75% full of water with 25% remaining as volume for air $V_2$ which can be given as:

$$V_2 = 0.5\, V_1 \tag{5.6}$$

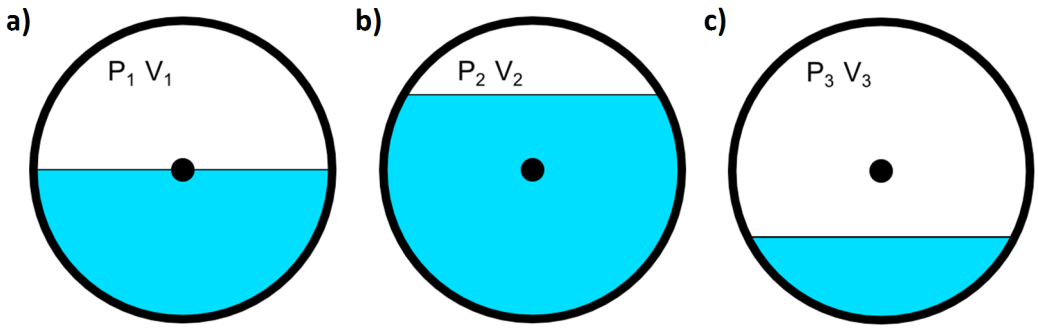


FIGURE 5.5 - STATIC MODE AIR PRESSURES WITH TANK a) 50%, b) 75% AND c) 25% FULL OF WATER

Finally, in Figure 5.5 c), only 25% of the tank is full of water with the remaining 75% left for air volume $V_3$ which is given as:

$$V_3 = 1.5\, V_1. \tag{5.7}$$

Using State 1, shown in Figure 5.5 a), as the initial condition the pressures $P_2$ and $P_3$ can be calculated from Equation (B.1) as:

$$P_2 = P_1 \frac{V_1}{0.5\, V_1} = 2\, P_1 \tag{5.8}$$

$$P_3 = P_1 \frac{V_1}{1.5\, V_1} = \frac{2}{3} P_1. \tag{5.9}$$

It can be seen from Equations (5.8) and (5.9) that a large range in pressure (from 66% to 200% the initial pressure) exists when just using the VBS tank.

An Expanded Volume mode was investigated as an alternative to reduce this large range of pressures. Figure 5.6 a) shows the expanded tank equivalent to the case shown in Figure 5.5 a) where the pressure $P_1$ and volume $V_1$ of air in the tank are equal. The expanded tank mode includes the additional volume of air in the charge tank $V_c$ which is equalized to the same pressure as the VBS tank $P_1$. The equivalent to Figure 5.5 b) is shown in Figure 5.6 b) which results in a different final pressure $P_4$ due to the larger total air volume in the expanded mode.

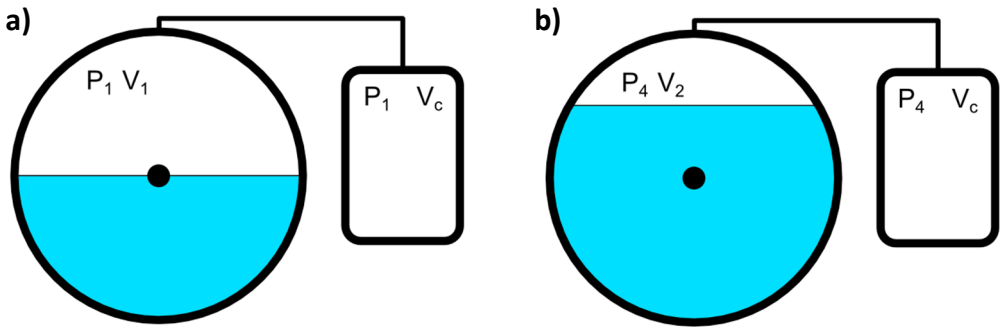


FIGURE 5.6 - EXPANDED MODE AIR PRESSURES WITH TANK 50% AND 75% FULL OF WATER

Assuming the volume of the charge tank $V_c$ to be equal to the initial volume of air $V_1$:

$$V_c = V_1 \tag{5.10}$$

then the pressure $P_4$, with the tank filled to 75%, would be given as:

$$P_4 = P_1 \frac{V_1 + V_c}{0.5\,V_1 + V_c} = \frac{4}{3} P_1. \tag{5.11}$$

Adding the equivalent of Figure 5.5 c) for the expanded tank, where the tank is only filled to 25%, the final pressure $P_5$ would be given as:

$$P_5 = P_1 \frac{V_1 + V_c}{1.5\,V_1 + V_c} = \frac{4}{5} P_1. \tag{5.12}$$

In both these cases, for the same volumes of water in the tank, the air pressure has changed less than the static mode. A summary of these differences is listed in Table 5.2 where the pressure is listed as a percentage of the original $P_1$ at the final VBS Tank ① air volumes $V_2$ and $V_3$ for both the static and expanded modes. It can be seen from these results that the Expanded Mode experiences a smaller change in the tank air pressure $P_a$ than the Static mode for the same changes in water volume $V_w$.

TABLE 5.2 - STATIC VS EXPANDED MODE PRESSURE CHANGE

| | STATIC | EXPANDED |
|---|---|---|
| **$V_2$** | 200% | 133.3% |
| **$V_3$** | 66.6% | 80% |

### 5.2.1 High Pressure Air Assisted Mode

The High Pressure Air Assisted mode proposed by Woods et al. [10] performed two functions:

1) **Air Vent Support**: Purge air from the system when the pressure in the tank $P_a$ reaches higher pressures.
2) **Compressed Air Support**: Increase the pressure in the tank to permit continued free emptying of the tank.

One of the primary assumptions for this method was an available charge air pressure $P_c$ of 100 MPa. While this pressure would permit compressed air support to be of use at depths up to 10 km, the possibility of attaining a charge tank with air at this pressure may not be practical. For example, industrial gas cylinders more commonly have working pressures in the range of 15-18 MPa (e.g. Praxair K and T type cylinders [24]) although there are some available rated as high as 46 MPa (e.g. Praxair 6K [24]). Even if a cylinder rated to 100 MPa were available it must be charged to this pressure. The typical air compressor is only rated for 1MPa (e.g. Ingersol Rand PB3-270-3 [25]) with high pressure models going only as high as 34.5 MPa (e.g. Ingersol Rand H15T4X200 [25]).

As such, the assumed initial pressure $P_c$ in Charge Tank ⑧ (Figure 4.1) for this thesis will be 30 MPa and the maximum pressure for the tank will be 10% higher than the working pressure. Therefore, to prevent the system from operating above the maximum load the Vent Air (**VA**) function would be activated to open Vent Valve ⑦ and relieve the air pressure $P_a$ when it is higher than the water pressure $P_{sw}$ by at most 33 MPa.

From Woods et al. [10] the compressed air support was used to increase the pressure $P_a$ in the VBS tank to permit continuous free emptying rather than requiring pumping in the interest in saving energy. Using this concept, the air pressure $P_a$ would need to be sustained above the water pressure by at least 275 kPa (the pressure where the system switches to pumping out **P-** instead of free flow **FF**). This sustained air pressure $P_{sustained}$ could be any value that complies with:

$$P_{sustained} - P_{sw} > 275\ kPa. \quad (5.13)$$

However, if this value were too high (e.g. $P_{sustained}$ = 1 MPa) it would cause the pump to work harder when increasing the water volume in the tank, resulting in more power consumption and releasing more pressurized air into VBS Tank ① from Charge Tank ⑧ than necessary. If too low (e.g. $P_{sustained}$ = 280 kPa) the system may drop past the 275 kPa mark while operating causing both the Pump Out **P-** and Charge Air **CA** to operate rather than the more efficient Free Flow **FF** and Charge Air **CA**. For this thesis, 400 kPa was selected as the sustained air pressure $P_{sustained}$ which would be maintained by activating the Charge Air **CA** function when commanded to empty the tank.

The ensuing High Pressure Air Assisted control logic can be seen in Figure 5.7. The logic first assesses whether the tank is being filled or emptied. If the system is filling and the pressure in the tank is more than 33 MPa above water pressure the Vent Air **VA** will be activated. Alternatively, if emptying and the air pressure is less than 400 kPa above water pressure (i.e. $\Delta P > -400\ kPa$) then the Charge Air **CA** function will engage. Otherwise, the system will be set to Null Air **NA** and both the vent and charge valves will be closed.

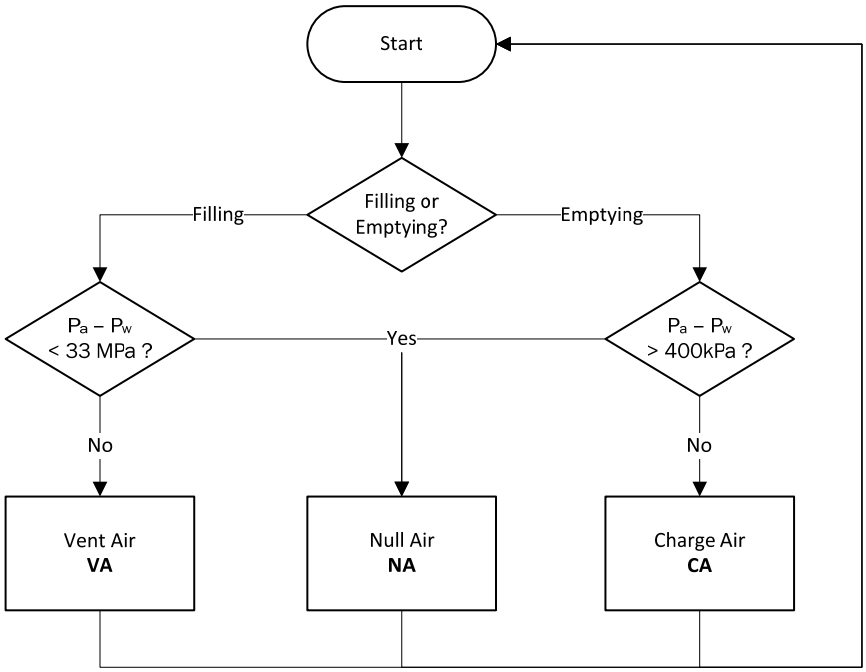


**FIGURE 5.7 - HIGH PRESSURE AIR ASSISTED LOGIC AS AN OPTION FOR VBS CONTROL**

### 5.2.2 Regenerative Mode

Liu et al. [11] also asserted that 100 MPa was likely impractical due to the limited availability of compressed air on an AUV. Therefore, the present author proposed a new method to reduce air pressure by returning air into Change Tank ⑧ and activating a Regen Air **RA** function rather than releasing it from the system with the Vent Air **VA** function.

The resultant Regenerative Air Assisted logic is shown in Figure 5.8. This mode is the same as the High Pressure Air Assisted mode as seen in Figure 5.7 but with the Regen function added. This function permits venting back into the charge tank when the system is being filled by the pump and the tank pressure $P_a$ is higher than the charge pressure $P_c$.

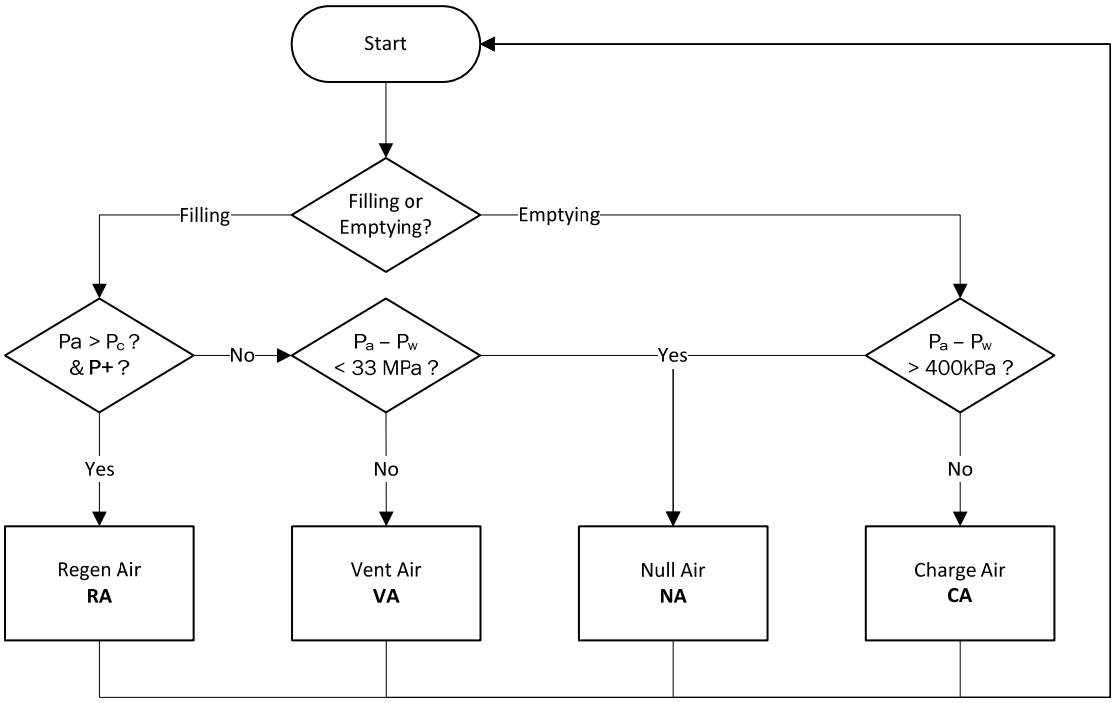


**FIGURE 5.8 - REGENERATIVE PRESSURE ASSISTED LOGIC TO AUGMENT HIGH PRESSURE AIR ASSISTED CONTROL**

### 5.2.3 Mode Comparison

To compare the four different modes of operation each was cycled at various water pressures in order to show the different performances at these pressures. An example of cycling the VBS water volume can be seen in Figure 5.9 where the Static mode is used with a water pressure $P_{sw}$ of 2500 kPa. The cycle begins with 30 L of water in the VBS Tank (50% of the full 60 L), as indicated in the upper portion of the figure as a dotted line, increasing to 45 L (75% full), down to 15 L (25% full) and back up to 30 L, repeating twice more. The energy consumed during the test is also indicated in the upper portion of the figure as a solid line increasing with the consumption of energy over time. The initial conditions for each test, regardless of water pressure $P_{sw}$, is:

$$P_a = 101\ kPa \tag{5.14}$$

$$P_c = 30\ MPa \tag{5.15}$$

$$V_a = 0.5\, V_t = 30\ L \tag{5.16}$$

The bottom portion of the figure displays the three pressures in the system where the water pressure $P_{sw}$ is indicated as a dashed line, the charge tank air pressure $P_c$ is shown as a dotted line and the VBS tank air pressure $P_a$ is denoted as a solid line. In the figure, water pressure remains constant at 2500 kPa for the test duration and charge pressure, similarly, remains at a constant 30 MPa as the Charge Air **CA** function is not used. The only pressure value to change in Figure 5.9 is air pressure; however, its value is so low that it appears as a straight line just above zero in this figure.

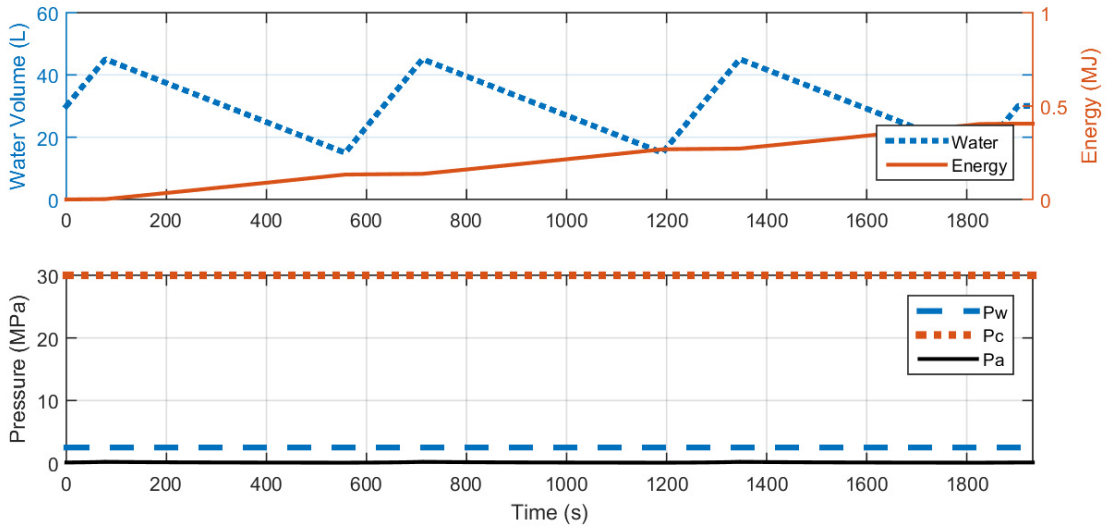


**FIGURE 5.9 - STATIC MODE VBS CYCLING BETWEEN 25% AND 75% FULL WITH INITIAL FILL OF 50% AT $P_{sw}$ = 2500 KPA**

This cycling test was repeated for each mode with water pressures $P_{sw}$ ranging from 2500 kPa to 40 MPa and the corresponding power consumption is shown in Figure 5.10. In this figure the power is indicated on the Y axis in Mega Joules and the water pressure, in kPa, is indicated on the X axis with the different modes grouped for each pressure. The Static mode can be seen to progressively require more power to operate as the pressure increases to the 40 MPa pressure at which point there were no results due to the pump failing to provide flow at this pressure. Since the quantity of air, and hence air pressure $P_a$, in VBS Tank ① remains constant, the pump effort increases for each test at

higher water pressures $P_{sw}$ which, in turn, corresponds to a higher total energy consumption for the test.

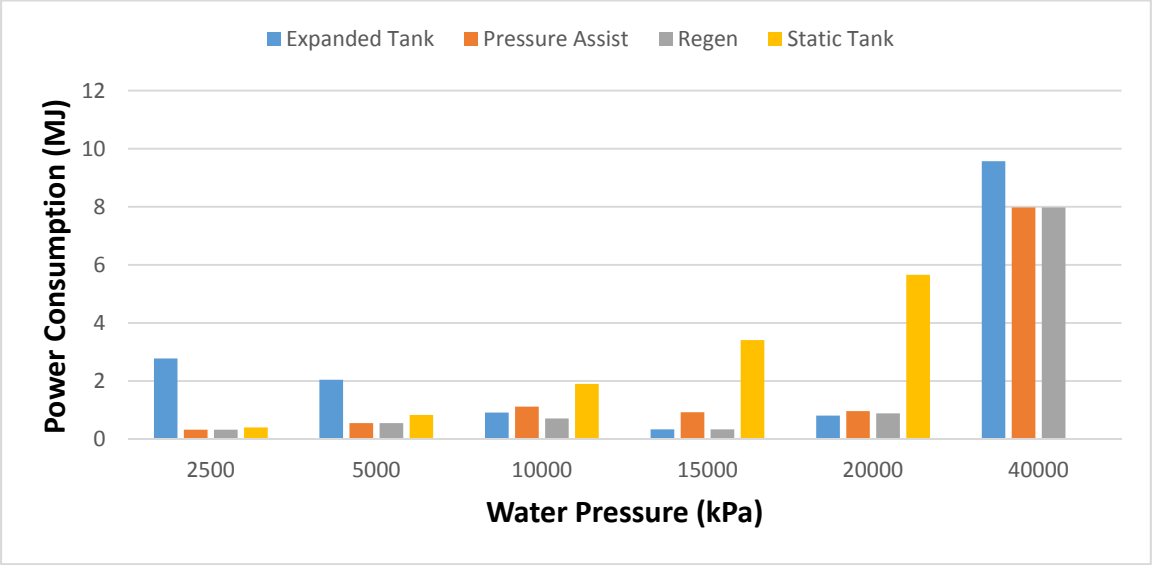


FIGURE 5.10 - VBS WATER CYCLING POWER CONSUMPTION AT VARIOUS PRESSURE DIFFERENTIALS

### 5.2.3.1 Expanded vs Static Mode

Compared to the Static mode, the Expanded mode demands more energy at lower water pressures which can be observed in Figure 5.10. However, as the water pressure $P_{sw}$ nears 15 MPa the Expanded mode becomes more efficient. The response of the VBS to cycling using the Expanded mode at a lower water pressure $P_{sw}$ of 2500 kPa is shown in Figure 5.11. The pressures, water volume and energy are indicated with lines similar to Figure 5.9.

Since the Expanded mode permits undisturbed air flow between VBS Tank ① and Charge Tank ⑧ the two pressures ($P_a$ and $P_c$) quickly equalize near 15 MPa in just under 50s. This air pressure results in a pressure difference ΔP of approximately -12.5 MPa requiring water to be pumped into the tank. Using the pumping in function **P+** with a ΔP this large results in a rapid increase in the energy used as seen in Figure 5.11. Once filled to 45 L at 350s, the air pressure becomes 20 MPa permitting a quick and low

energy consuming transition to 15 L using the free flow function **FF** which concludes at 420s. The cycle then repeats with the two tanks continuing to equalize their pressures. Consequentially due to the Expanded mode exhibiting a higher magnitude ΔP there is a higher energy demand at lower water pressures than for the Static mode.

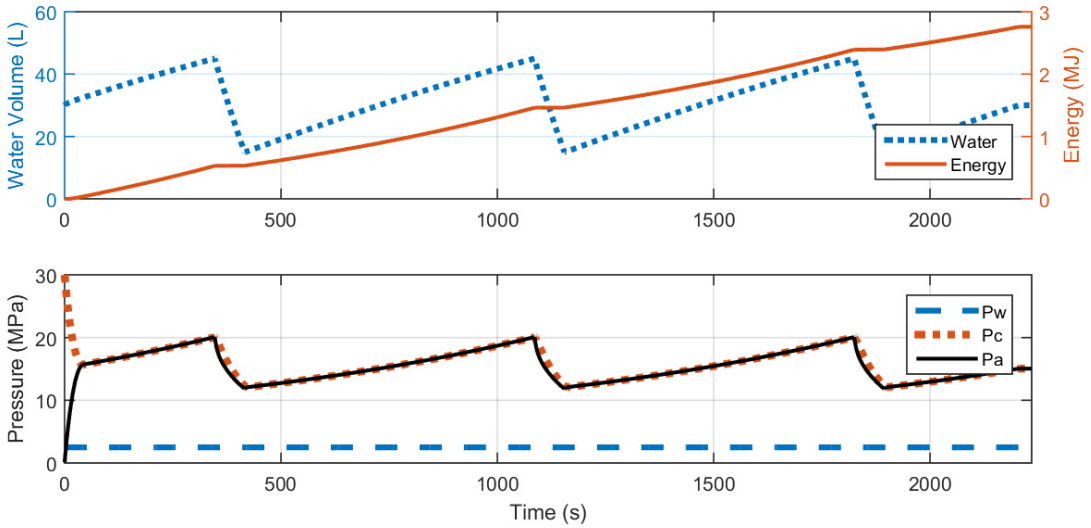


**FIGURE 5.11 - VBS WATER CYCLING IN EXPANDED MODE AT $P_{SW}$ = 2500 KPA – SHOWING HIGHER POWER CONSUMPTION THAN USED IN STATIC MODE IN FIGURE 5.9**

The equalized pressure $P_2$ at the initial conditions observed in Expanded mode can be can calculated from:

$$P_a V_a + P_c V_c = P_2 (V_a + V_c) \tag{5.17}$$

Since $P_a \ll P_c$ the value of $P_a$ can be assumed to be zero so that $P_2$ can be given as:

$$P_2 = \frac{P_c V_c}{V_a + V_c} \tag{5.18}$$

resulting in:

$$P_2 = \frac{30\ L}{60\ L}\ 30\ MPa = 15\ MPa \tag{5.19}$$

As water pressure nears that of equalization the efficiency of the Expanded mode improves. An example of the response of the VBS in Expanded mode at 15 MPa can be seen in Figure 5.12. Similar to the lower water pressure case, the tank air and charge pressures quickly converge and reflect each other for the remainder of the test. Initially the air pressure $P_a$ is much lower than the water pressure $P_{sw}$ permitting free flow **FF** mode to be used to quickly fill the tank until the two pressures approach each other at 30s during which very little energy is consumed. At this point the pressure requires the system to switch to pumping in **P+** mode until the desired water volume 45 L is achieved at 160s and, in doing so, the power consumed increases more with the pressure difference.

When the water volume reaches the upper bound, pressure in the tank increases to 20 MPa resulting in a ΔP value of 5 MPa which permits free flow **FF**. The pump out **P-** function takes over at 220s when the air pressure $P_a$ drops. The pump out **P-** function continues until the low water volume is reached at 490s with a corresponding increase in energy demand as observed in Figure 5.12. The cycle repeats using the same combination of free flow and pumping to fill and empty tank. Since air and water pressures remain closer than at lower water pressures (e.g. 2500 kPa) less energy is consumed.

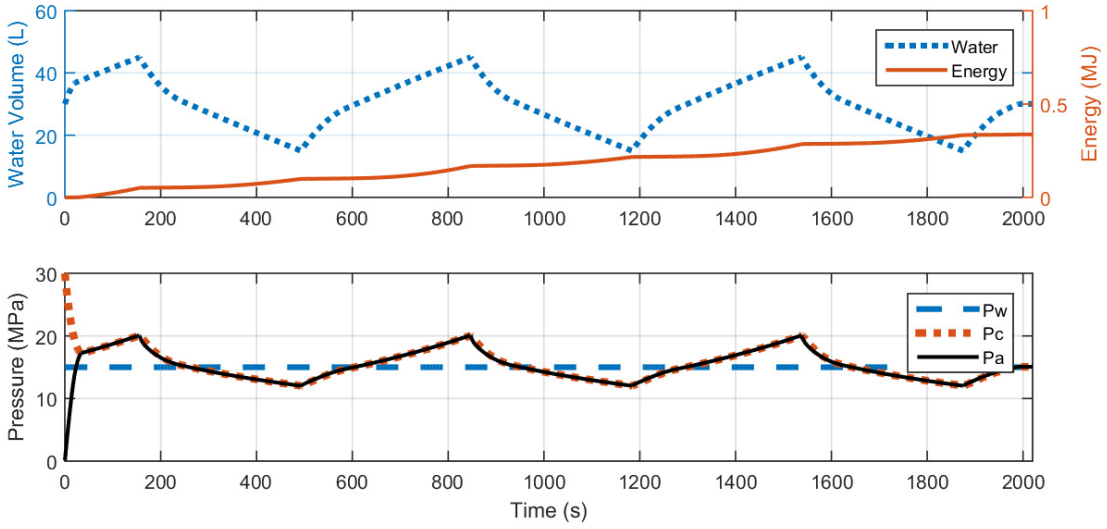


**FIGURE 5.12 - VBS WATER CYCLING IN EXPANDED MODE AT $P_{sw}$ = 15MPA – SHOWING LOWER POWER CONSUMPTION THAN USED IN STATIC MODE IN FIGURE 5.9 DESPITE OPERATING AT HIGHER PRESSURE**

### 5.2.3.2 Pressure Assisted Mode Comparison

Compared to both the Static and Expanded modes, there is a lower energy demand when using the Pressure Assisted mode for lower water pressures (e.g. $P_{sw}$ < 10 MPa) as shown in Figure 5.13 for a water pressure of 2500 kPa. With the water pressure $P_{sw}$ initially much higher than the air pressure $P_a$, free flow **FF** is used to quickly fill to 45 L of water. Once full, at 80s the new desired water volume is set to 15 L. To achieve this volume, charge air **CA** is enabled to keep ΔP above $P_{sustained}$ which permits the use of free flow **FF** to purge water until 490s.

With free flow **FF** used to both increase and then decrease water in the tank, not much energy is consumed up to 400s; however, increasing the volume of water once more in the tank to 45 L requires the use of the pump in **P+** function. At the end of the next fill cycle air pressure has increased to over 8000 kPa with a corresponding ΔP of 5500 kPa. Additionally, as this pressure is approached the energy demand greatly increases until the end of the cycle at 880s as seen in Figure 5.13. After this point the system continues to cycle using free flow to empty the tank until 1280s which requires very little energy.

The cycle repeats once more using the pump to fill and free flow to empty. For this water pressure $P_{sw}$, in comparison to both the Static mode (Figure 5.9) and Expanded mode (Figure 5.11), the Pressure Assist mode results in a lower use of energy.

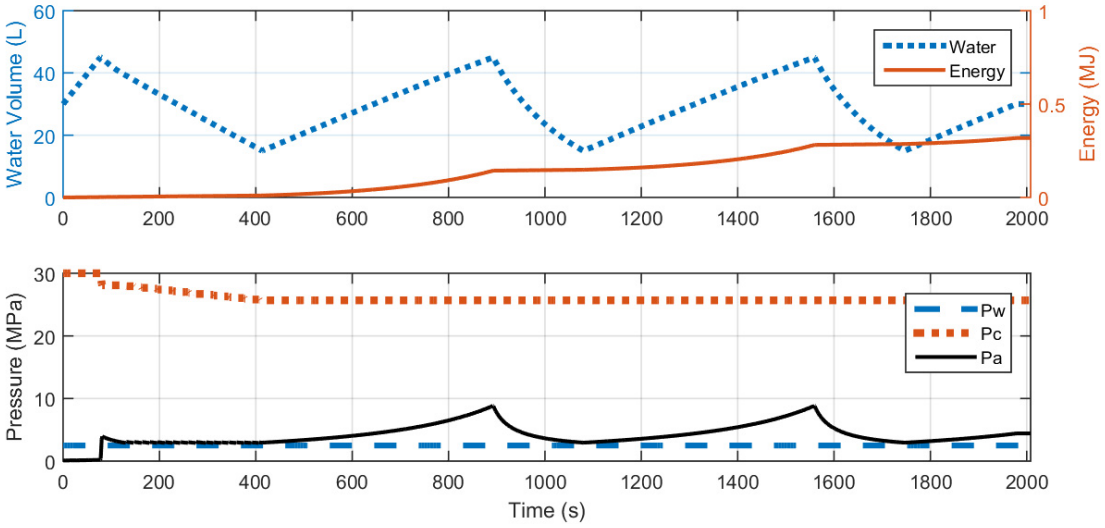


**FIGURE 5.13 - VBS WATER CYCLING IN PRESSURE ASSISTED MODE AT $P_{sw}$ = 2500 KPA – SHOWING LOWER POWER CONSUMPTION THAN USED IN STATIC MODE IN FIGURE 5.9**

The result of the VBS running in Pressure Assisted mode at a water pressure of 15 MPa can be seen in Figure 5.14. Similar to the response at 2500 kPa, the water volume quickly increases to 45 L at the start of the test using the free flow **FF** function and switches to charge air **CA** to reduce water volume $V_w$ at 40s. At this higher water pressure $P_{sw}$, the quantity of air in Charge Tank ⑧ is insufficient to increase the pressure in VBS Tank ① above the water pressure when filled with only 15 L of water. Consequentially at 220s the air pressure $P_a$ approaches the water pressure $P_{sw}$ and free flow cannot be used to reduce water further requiring pump out **P-** to complete the process.

With a water volume $V_w$ of 15 L at 460s, the VBS is commanded to return back to 45 L. To do so it selects free flow **FF** since the air pressure is less than the water pressure until 480s when pumping P+ must be used. While pumping, the air pressure $P_a$ quickly

increases with the water volume and peaks at 36 MPa when the water volume reaches at 45 L. The high air pressure results in a final ΔP of 21 MPa and corresponds to a large energy consumption while filling the tank a second time. The consecutive emptying of the tank at 920s initially uses free flow **FF** to quickly reduce the water volume until the pressure difference becomes small at around 980s when pumping out **P-** is required. One more cycle is then performed identical to the last.

Compared to the Static mode, the Pressure Assist mode provides a considerable savings in energy at a water pressure of 15 MPa (Figure 5.10). However, in comparison to the Expanded mode (Figure 5.12) at the same water pressure, the Pressure assist mode is less efficient.

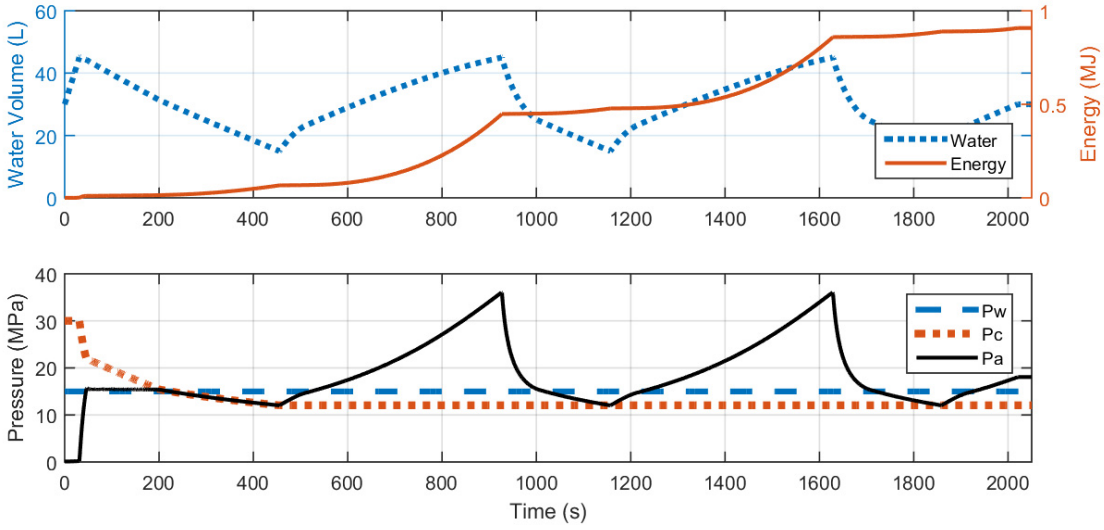


**FIGURE 5.14 - VBS WATER CYCLING IN PRESSURE ASSISTED MODE AT $P_{sw}$ = 15 MPA – SHOWING HIGHER POWER CONSUMPTION THAN USED IN EXPANDED MODE IN FIGURE 5.12**

### 5.2.3.3 Regenerative Pressure Mode Comparison

When comparing the Regenerative mode to the other three at lower pressures (e.g. $P_{sw}$ < 10 MPa) its performance mirrors that of the Pressure Assisted mode. At these lower water pressures, the air pressure $P_a$ does not exceed the charge pressure $P_c$ (see Figure

5.12), consequentially, the regen air **RA** function cannot be used and this mode behaves the same as the Pressure Assist mode.

Figure 5.15 shows the results of cycling the VBS in the Regenerative mode at 15 MPa where the initial cycle, concluding at 450 seconds, is identical to the response of the Pressure Assist mode in Figure 5.14. To refill the tank, the system first engages free fill **FF** until 500s when ΔP becomes small, after which both pump in **P+** and regen air **RA** engage to increase the water volume to 45L. This combination results in a reduction in the pressure difference ΔP across the pump and a lower energy consumption compared to the Pressure Assist mode as seen in Figure 5.14.

At 850s, to reduce the water volume back to 15 L the system engages free flow **FF** and charge air **CA** until the air pressure $P_a$ can no longer be held above the water pressure $P_{sw}$ at 975s. When the water pressure drops further, pump out **P-** is engaged to complete the cycle at 1250s and the process is repeated once more.

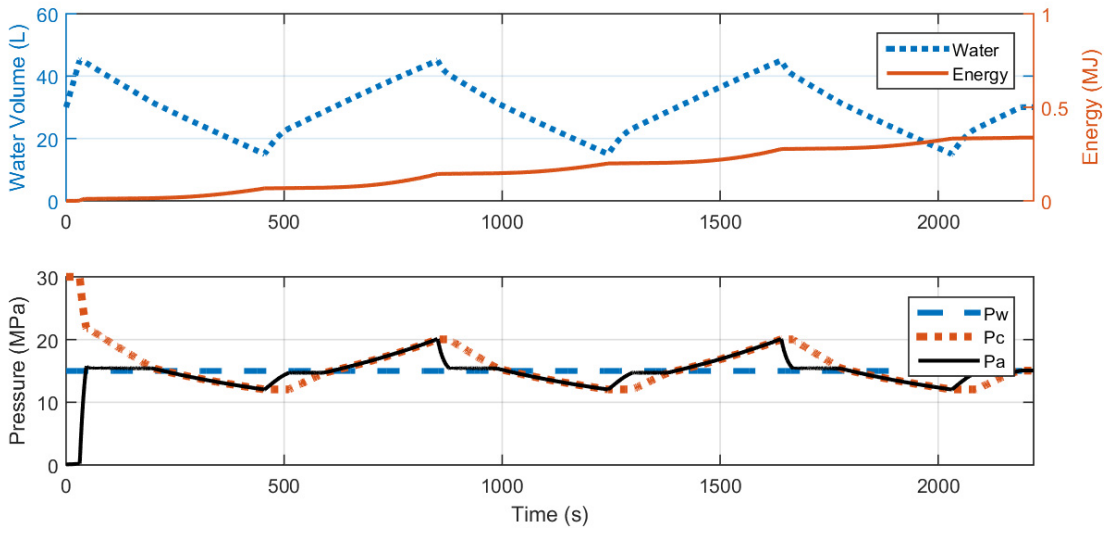


**FIGURE 5.15 - VBS WATER CYCLING IN REGEN MODE AT $P_{sw}$ = 15 MPA – SHOWING LOWER POWER CONSUMPTION THAN USED IN PRESSURE ASSISTED MODE IN FIGURE 5.14**

Compared to the Pressure Assisted mode, the Regenerative mode offers energy savings and behaviour comparable to the Expanded mode when close to a water pressure of 15

MPa. Since the Regenerative mode has proven to be of equal or better efficiency to the other three modes it was used for the remainder of this thesis.

## 5.3 Mass control

With the system designed to react to a command signal **sig**, which determines both flow direction and the degree to which either water is pumped or free-flows through the directional valve, it is possible to create a control loop around the system mass. Liu et al. [11] proposed using a PD loop to control the mass of the prospective VBS. This approach was adopted for this thesis and the resulting control loop for VBS mass is seen in Figure 5.16. The input to the loop is taken from the VBS model as mass $m_{vbs}$ and is compared to the desired mass $m_{set}$ to give the mass error $m_{err}$. The PD controller acts on this error value to generate a command signal **sig** to the VBS.

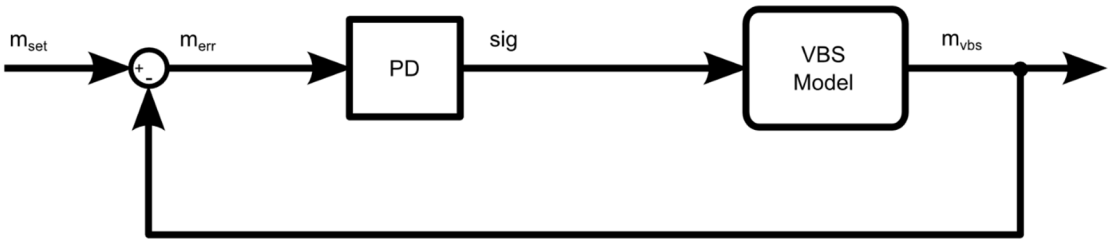


**FIGURE 5.16 - VBS MASS CONTROL USING PID (PD)**

The initial conditions for testing the VBS Mass Controller are shown in Figure 5.17 where VBS Tank ① was half full of water leaving the remaining 30 L volume for air $V_a$ at a pressure $P_a$ of 101 kPa. Pressure in Charge Tank ⑧ $P_c$ was set to 30 MPa with the volume $V_c$ set to 30 L. Depth was selected to be 1000m corresponding to a water pressure $P_{sw}$ of 10 MPa.

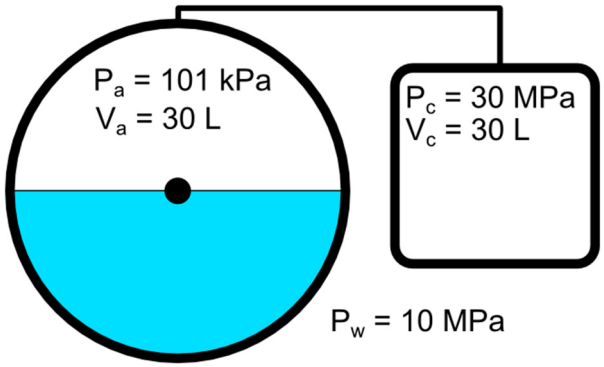


FIGURE 5.17 - VBS MASS CONTROL INITIAL CONDITION FOR TESTING

The result of the tuned controller is shown in Figure 5.18 where the step response of the mass of the VBS can be seen. In the figure the dashed line denotes the commanded signal which changes from the initial command of 0 kg to an additional 20 kg at 30 seconds, and then setting the signal back to 0 kg at 160 seconds. The VBS response, shown in Figure 5.18 as a solid line, quickly changes from 0 kg to the commanded 20 kg in approximately 60 seconds. This swift change is due to the system running in the free flow state with a high ΔP of 10 MPa. Reducing back to 0 kg takes longer (200 seconds) due to the difference in the VBS function. Initially, the VBS engages the pump to expel water while the charge function increases the tank pressure for the first 20 seconds. After this time the system switches to free flow mode while maintaining the pressure at $\Delta P \geq 400$ kPa. This lower magnitude ΔP value causing the tank to empty results, expectedly, in a lower observed flow rate. The selected gains for the PD controller were P = 1 and D = 0.1.

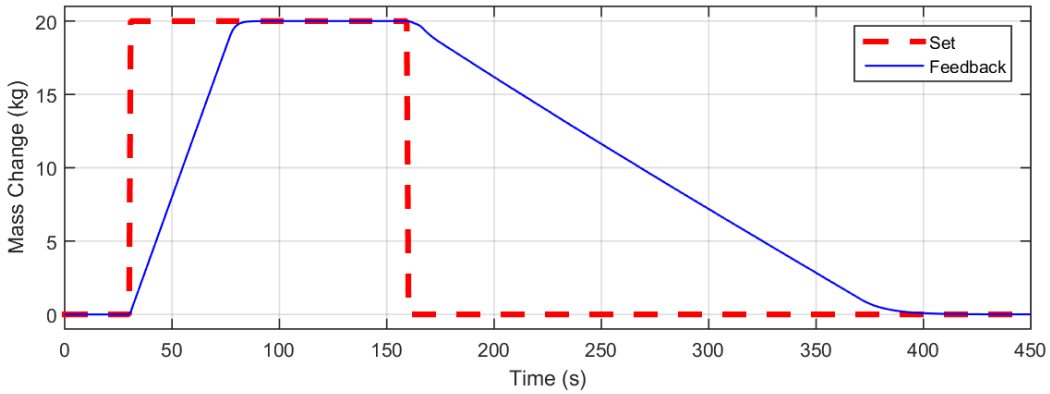


FIGURE 5.18 – VBS MASS STEP RESPONSE FROM 0 KG, TO 20 KG BACK TO 0 KG

## 5.4 Depth Control

The ability of the VBS forces to affect AUV depth are depicted in Figure 5.19. The forces $F_{vbsf}$ and $F_{vbsa}$ act with or against gravity, depending on the net buoyancy, and as such are applied in the global Y axis direction, unlike the hydrodynamic forces. To command a change in only depth and hence prevent a change in pitch, the moment $M_\psi$ about the Z axis must be zero.

It is therefore possible to directly adjust depth with only the VBS input; however, as there are two VBS on board located at distances $l_{fb}$ and $l_{ab}$ from CoG, adjustments must be made so as not to affect the AUV's pitch (see Equation (2.5)). The equation for moment $M_\psi$ in this case would be give as:

$$M_\psi = F_{vbs_f} l_{fb} - F_{vbs_a} l_{ab} = 0 \tag{5.20}$$

resulting in:

$$F_{vbs_f}\, l_{fb} = F_{vbs_a}\, l_{ab} \tag{5.21}$$

where

$F_{vbsf}$ = the net buoyancy force of the fore VBS

$F_{vbsa}$ = the net buoyancy force of the aft VBS

$l_{fb}$ = the longitudinal position of the fore VBS

$l_{ab}$ = the longitudinal position of the aft VBS

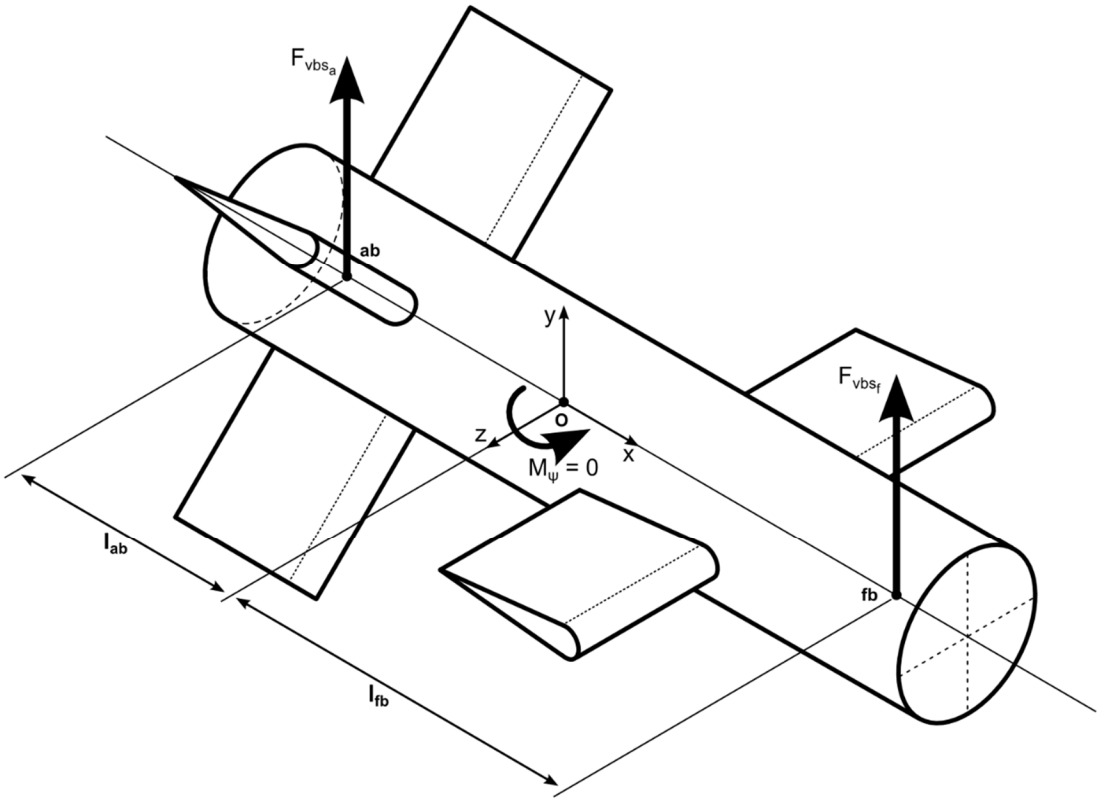


FIGURE 5.19 - VBS DEPTH CONTROL FORCES

For this thesis it has been assumed that the lengths $l_{fb}$ and lab are equal:

$$l_{fb} = l_{ab} \tag{5.22}$$

Therefore, control of AUV depth can be achieved by changing both the fore and aft VBS equally to not affect pitch such that:

$$F_{vbs_a} = F_{vbs_f} \tag{5.23}$$

Using the command mass input $m_y$, the input values for the VBS (per Equations (5.4), (5.22) and (5.23)) would be:

$$m_{f_{set}} = m_y \tag{5.24}$$

$$m_{a_{set}} = m_y. \tag{5.25}$$

In Figure 5.20 the control diagram for depth using only VBS input can be seen. In this loop the feedback signal is the actual depth $y$ of the AUV. This value is compared to the setpoint depth $y_{set}$ to give the difference $y_{err}$ which is acted upon by the PID controller. The output of this controller is given to the two VBS as a desired mass signal $m_y$ where the mass controlled VBS model (Figure 5.16), in turn, calculates the actual masses to be applied to the AUV model.

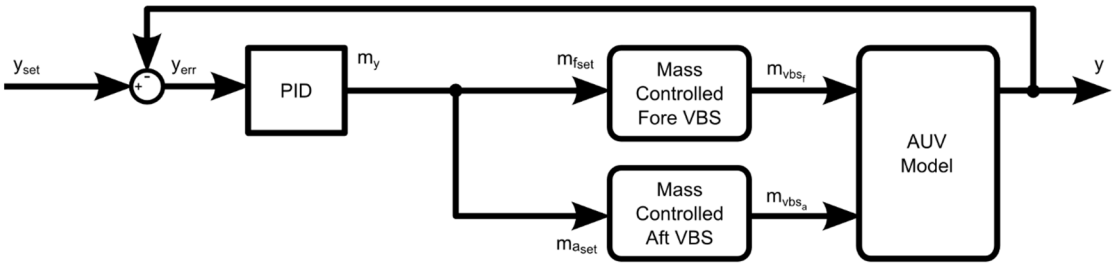


FIGURE 5.20 - VBS DEPTH CONTROL

The response of the AUV with this VBS controller enabled in the absence of any hydroplane control input can be seen in Figure 5.21. In this figure the dashed line indicates the commanded depth stepping from the initial 0 m down to 20 m at 30 seconds. The subsequent dotted, dash-dot and solid lines are the feedback depth using the proportional gains P = 0.1, P = 0.3 and proportional gain P = 0.3 with derivative gain D = 6. It can be seen that an increase in the proportional gain from 0.1 to 0.3 improved the response time by about 100 seconds. Additionally, the inclusion of the derivative gain prevents overshoot as the feedback settles at the set point near 250 seconds. The selected gains for the PID controller were, therefore P = 0.3 and D = 6.

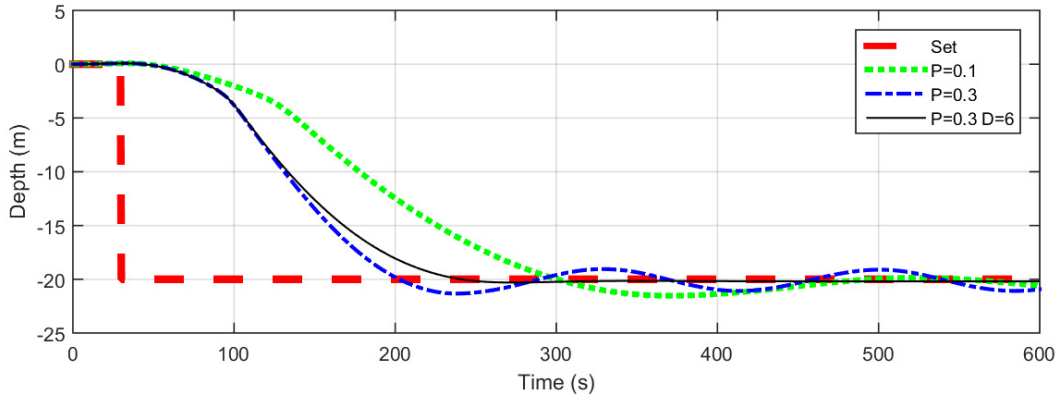


FIGURE 5.21 - DEPTH STEP RESPONSE FROM 0 M TO 20 M WITH VBS CONTROLLER

## 5.5 Pitch Control

Unlike depth control which requires a net change in the buoyancy force and a zero induced moment, the reverse is required to achieve a change only in pitch. The corresponding VBS forces and moment can be seen in Figure 5.22.

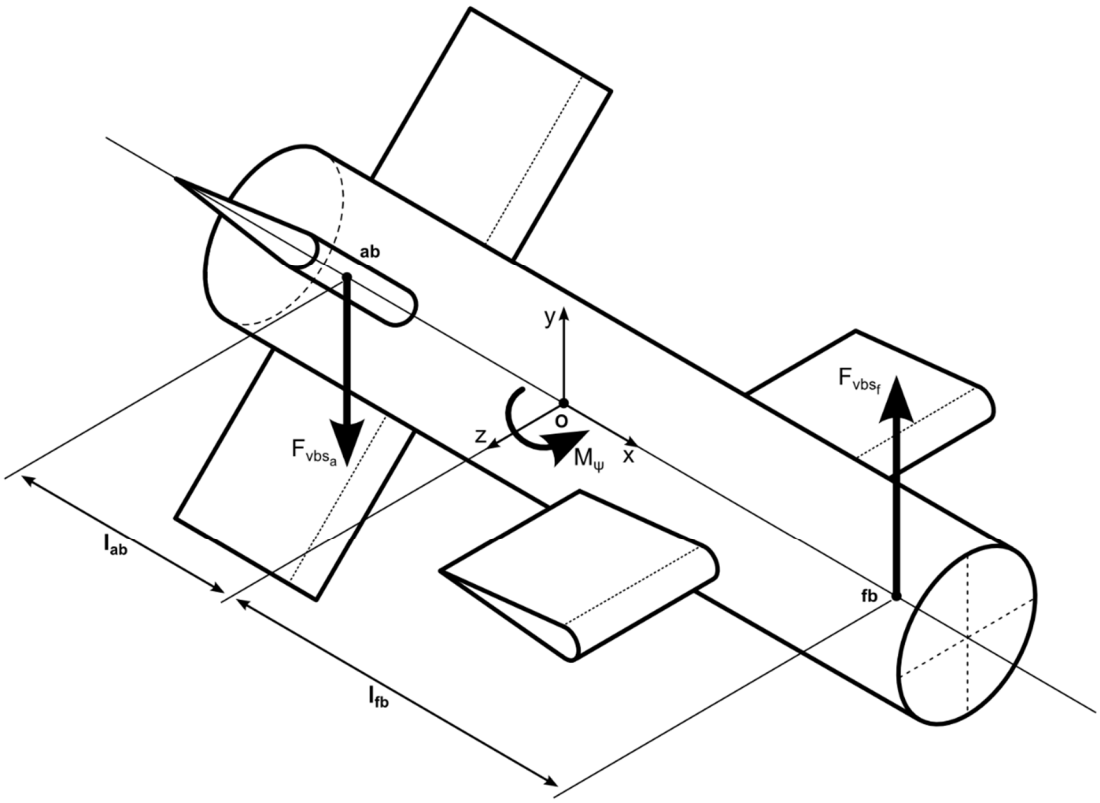


FIGURE 5.22 - VBS PITCH CONTROL FORCES

As a result, the moment $M_\psi$ is given as:

$$M_\psi = F_{vbs_f} l_{fb} - F_{vbs_a} l_{ab} \neq 0 \tag{5.26}$$

Combining Equations (5.22) and (5.26) gives:

$$F_{vbs_f} \neq F_{vbs_a} \tag{5.27}$$

To ensure that the depth is not affected the two VBS forces must sum to zero. The equation for the forces are given as:

$$F_{vbs_f} + F_{vbs_a} = 0 \tag{5.28}$$

$$F_{vbs_f} = -F_{vbs_a} \tag{5.29}$$

Using the command input of mass $m_\psi$ the signals for the two VBS would be given as:

$$m_{f_{set}} = -m_\psi \tag{5.30}$$

$$m_{a_{set}} = m_\psi \tag{5.31}$$

In Figure 5.23 the control diagram for pitch using only VBS input can be seen. In this loop the feedback signal is the actual pitch angle ψ of the AUV. This value is compared to the desired pitch $\psi_{set}$ to give the difference $\psi_{err}$ which is acted upon by the PID controller. The output of this controller is given to the two VBS as a desired mass signal $m_\psi$ with as a positive value for one and a negative value for the other. The mass controlled VBS model (Figure 5.16) in turn calculates the actual masses to be applied to the AUV model.

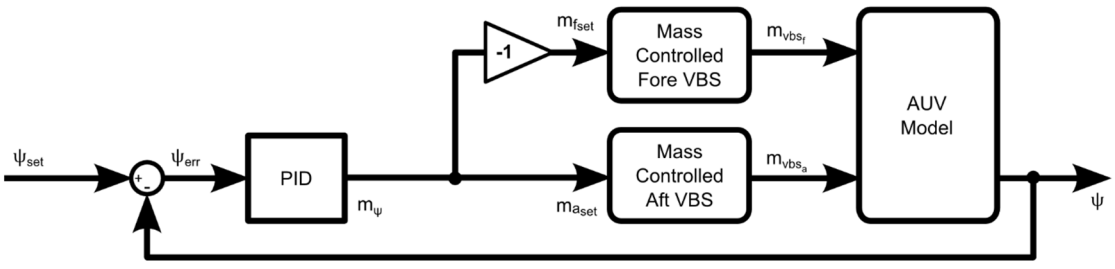


FIGURE 5.23 - VBS PITCH CONTROL

The response of the pitch controlled VBS can be seen in Figure 5.24. In this figure the dashed line indicates the commanded pitch stepping from the initial 0° to 5° at 30 seconds. The subsequent dotted, dash-dot and solid lines are the feedback depth using the gains of P = 0.5, P= 1 and D = 20, and a third controller adding I = 0.01 to the PD controller. Use of higher proportional gains was found to create instability requiring differential gains to stabilize the system when P > 0.5. When P was set to 1, a steady-state error was still observed and, as such, an integral gain was required to eliminate this steady-state error; however, some oscillation was observed – ultimately resulting in the use of a PID controller having gains of P=0.5, P=1 and D=20. With this selected PID control the pitch was found to achieve the set value within 400 seconds as shown in Figure 5.24, which is much longer than the response observed using hydroplane control in Figure 3.14. This longer response time is indicative of the relative speeds that the hydroplanes and VBS can affect the AUV.

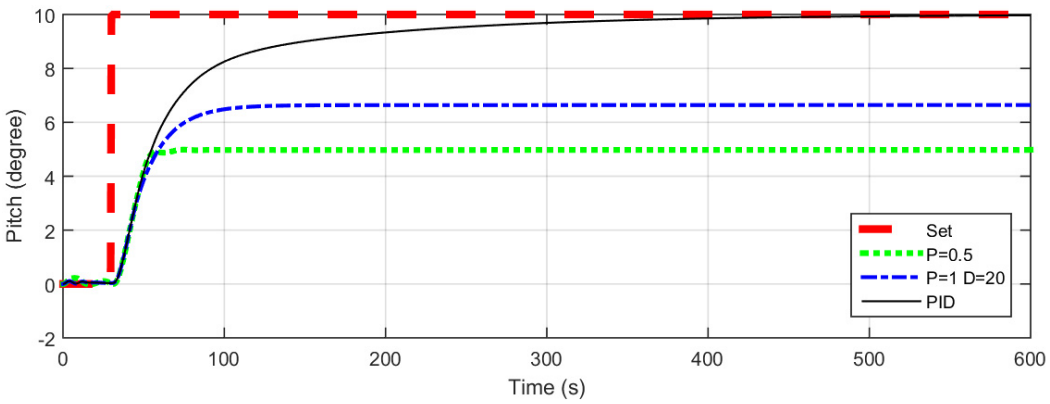


FIGURE 5.24 - PITCH STEP RESPONSES FROM 0 DEGREES TO 10 DEGREES WITH VBS CONTROLLER

## 5.6 Combined Pitch and Depth Control

Combining the depth and pitch control schemes which were governed by Equations (5.24), (5.25), (5.30), and (5.31) yields:

$$m_{f_{set}} = m_y - m_\psi \tag{5.32}$$

$$m_{a_{set}} = m_y + m_\psi. \tag{5.33}$$

The resulting combined control diagram is shown in Figure 5.25. In this figure, as in Figure 5.20 and Figure 5.23, the depth and pitch errors are calculated from the setpoint and feedback values. These errors are then minimized by their respective PID controllers. The outputs from these PID controllers are now, however, combined with the sum of the two being applied to VBS2 and the difference to VBS1 per Equations (5.32) and (5.33).

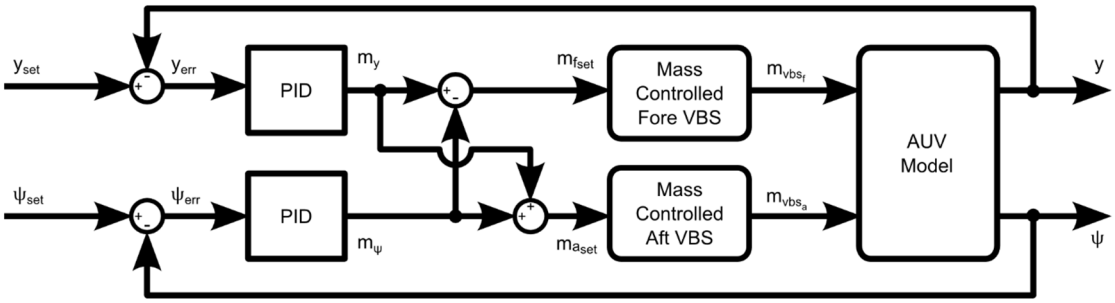


FIGURE 5.25 - VBS PITCH AND DEPTH CONTROL

The response of the combined controller can be seen in Figure 5.26. In the upper portion of the figure the depth values are shown with the commanded value, denoted as a dashed line, stepping from a depth of 0m down to 20 m at 30s. The depth response, shown as a solid line, can be seen to repeat the results from Figure 5.21 reaching the desired depth at 430s. The lower portion of the figure shows the pitch angle, where the depth command is once more shown as a dashed line and changes from 0° to 10° at 30s. The response is different than that observed in Figure 5.24 as the response rate of the VBS is too slow to compensate for the hydrodynamic moment generated while descending. Despite the additional forces being generated the desired pitch is still achieved albeit in a slightly longer length of time than when operating independently.

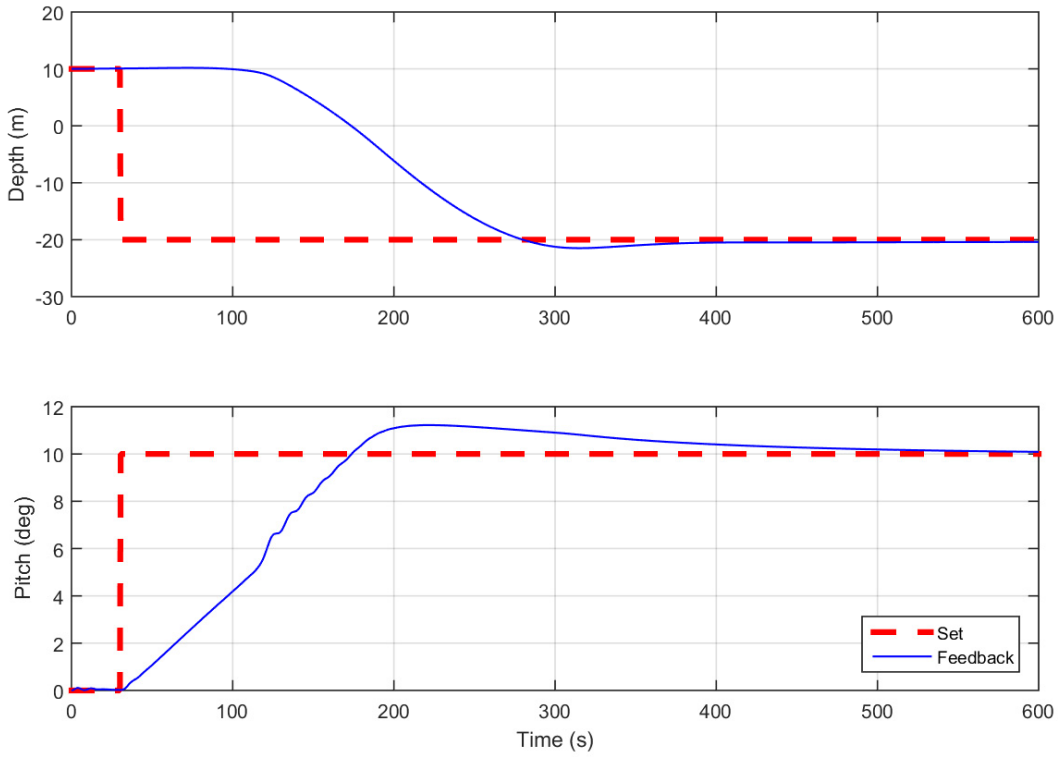


FIGURE 5.26 - SIMULTANEOUS STEP RESPONSE FROM 0M AND 0° TO -20M AND 10° PITCH

# Chapter 6: Integrating Controls

AUV control to this point in this thesis has been limited to either hydroplane or VBS control inputs. In this chapter the interaction of these two control inputs will be further explored to help better understand scenarios where this new VBS control system can be successfully utilized.

## 6.1 Simultaneous VBS and Hydroplane Control

Simultaneously using the hydroplane controller developed in Chapter Chapter 3: and the VBS controller developed in Chapter Chapter 5: to adjust pitch yields the results seen in Figure 6.1 where the AUV is set to a velocity u of 1.5 m/s. In Figure 6.1 a) the commanded pitch is shown as a dashed line and the actual feedback pitch as a solid line. Referring to this figure, a commanded step input of 10° is given at 30 seconds and the resulting AUV pitch quickly achieves this desired 10° pitch in less than 20 seconds.

The deflection of the hydroplanes can be seen as a function of time in Figure 6.1 b) where the aft hydroplanes, shown as a solid line, are seen to quickly react to the commanded step change and their deflection reaches just over 5° and then reduces to a slightly lower steady-state value. The fore hydroplanes, shown as a dotted line, remain constant at zero degrees as no set depth was commanded for this test.

Little VBS reaction is observed from the VBS in Figure 6.1 c) where the masses of the fore and aft VBS are shown as a dotted and a solid line, respectively. This limited response of the VBS is due to the difference in reaction time of the VBS and the hydroplanes. Recalling from Figure 5.24, the time to adjust the AUV pitch using the VBS is much longer than seen here for the hydroplanes. As a result, the VBS does not have the opportunity to react substantially before the pitch error is eliminated and the hydroplanes are left holding at a steady-state angle to maintain the set pitch.

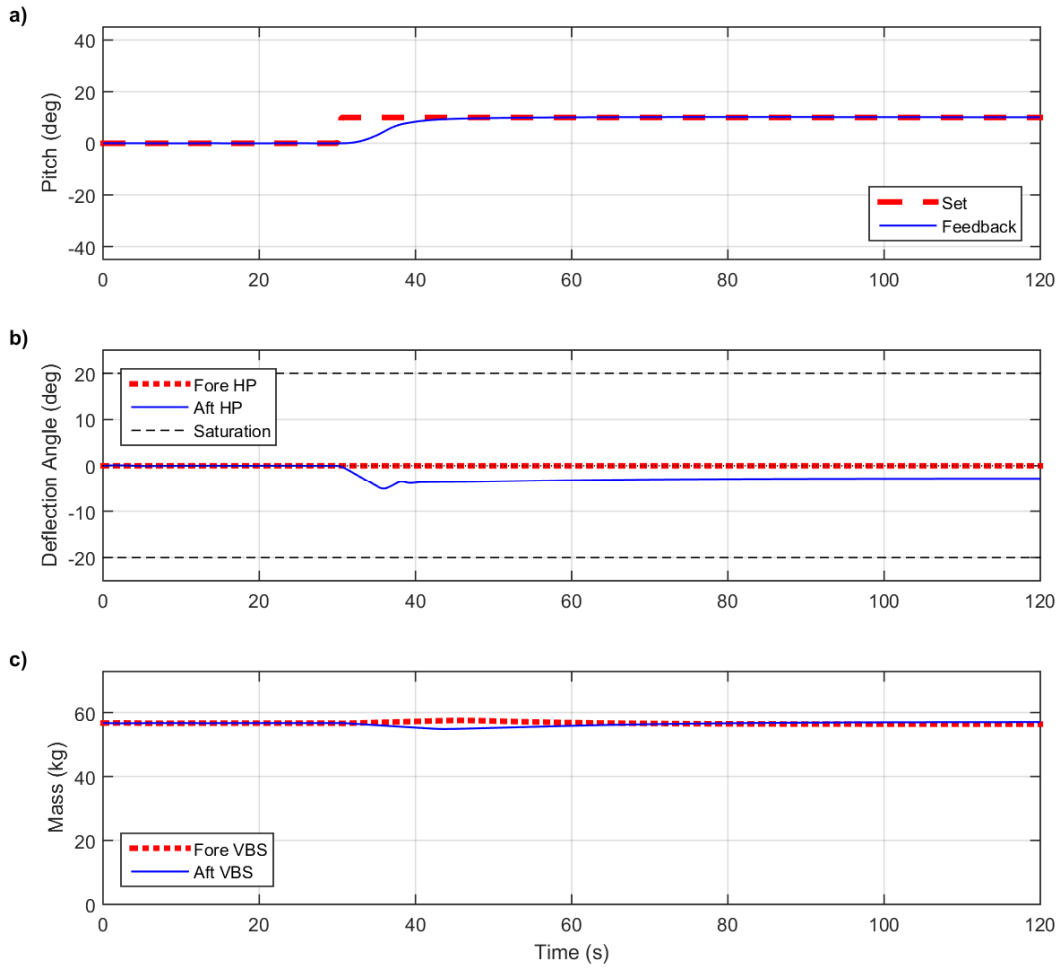


FIGURE 6.1 - INTEGRATED CONTROL AUV RESPONSE TO FIXED PITCH OF 20 DEGREES

A similar result can be observed where the AUV's depth position is set to rise to depth a 15° incline trajectory while operating at a velocity u of 1.5 m/s and holding to a pitch of 0° as demonstrated in Figure 6.2. The corresponding simulation results with the AUV's hydroplanes and VBS operating together is shown in Figure 6.3.


FIGURE 6.2 - AUV TRAJECTORY: 15° INCLINE

The set depth, depicted as a dashed line, and feedback depth, shown as a solid line, are presented in Figure 6.3 a) where the feedback depth can be seen to closely follow the set depth as desired. The corresponding AUV feedback pitch, shown in Figure 6.3 b) as a solid line, is seen to remain stable near the 0° set point.

The AUV depth is achieved through deflections of the fore planes, shown as a dotted line in Figure 6.3 b). These fore planes react immediately to the depth error and eventually hold steady at a deflection angle near 15°. The velocity from moving in the vertical Y direction generates drag along the length of the AUV. This drag force is uniform on the cylindrical body; however, on the hydroplanes this force is much larger. Since the location of this higher drag force is not located at the center of gravity a pitching moment is generated coupled to the vertical motion. The aft planes, shown as a solid line in Figure 6.3 c), react to this pitching moment to hold the pitch stable and, in doing so, establish a steady deflection angle near 8°.

Finally, the masses of the fore and aft VBS can be seen in Figure 6.3 d) as a dotted line and a solid line, respectively. The small offset observed in the VBS response does not significantly reduce the deflection angles of either the aft or fore hydroplanes.

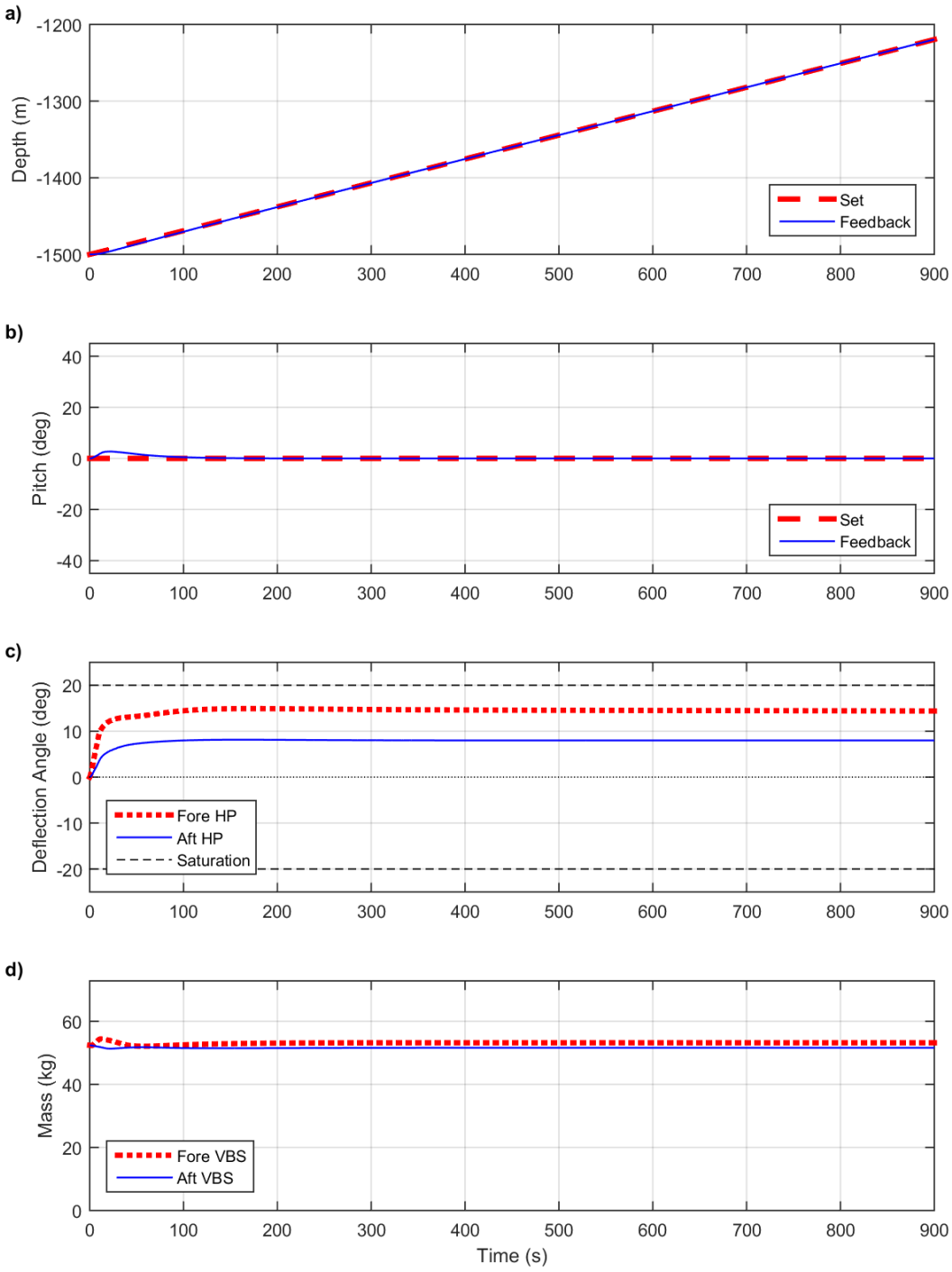


**FIGURE 6.3 - AUV RESPONSE FOLLOWING 15° INCLINE USING CLOSED LOOP CONTROL ON PITCH AND DEPTH FOR BOTH HP AND VBS RESULTING IN LIMITED RESPONSE FROM VBS DUE TO LONGER REACTION TIME**

Given the observed lack of sufficient response from the VBS system using AUV depth and pitch error as control inputs a new control strategy was developed to try to more directly affect the hydroplane deflection angles in order to help restore their control authority.

## 6.2 Hydroplane Deflection Feedback

In this section a new control scheme is proposed for the VBS that uses the actual deflection angles of the fore hydroplane $\alpha_f$ and decoupled contribution to pitch of the aft hydroplane deflection as feedback in place of AUV depth y and pitch ψ. Using this control strategy permits the VBS to respond to a direct measure of the effort on the part of the hydroplanes. The result being that the slower responding VBS provides restoration of the HP control authority which in turn allows them to respond to short term changes in trajectory. The resultant controller, shown in Figure 6.4, closely resembles what was used previously in Figure 5.25 except for the new feedback signals $\alpha_f$ and $\alpha_{a\psi}$.

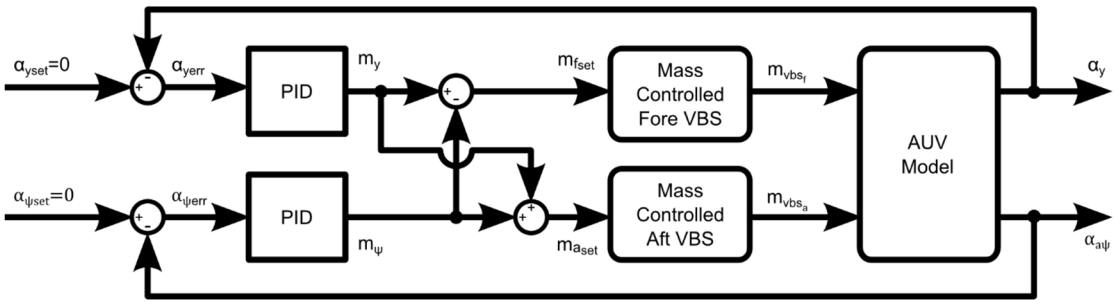


**FIGURE 6.4 - VBS CONTROL USING HYDROPLANE DEFLECTION ANGLE**

Three different proportional gains were tested using the new controller strictly for pitch control. Figure 6.5 shows the results where each of these three gains were tested. A gain of P=2 was ultimately selected as it resulted in the smallest steady state error. No

integral gain was added to eliminate this steady state error in order to give preference to depth control over pitch.

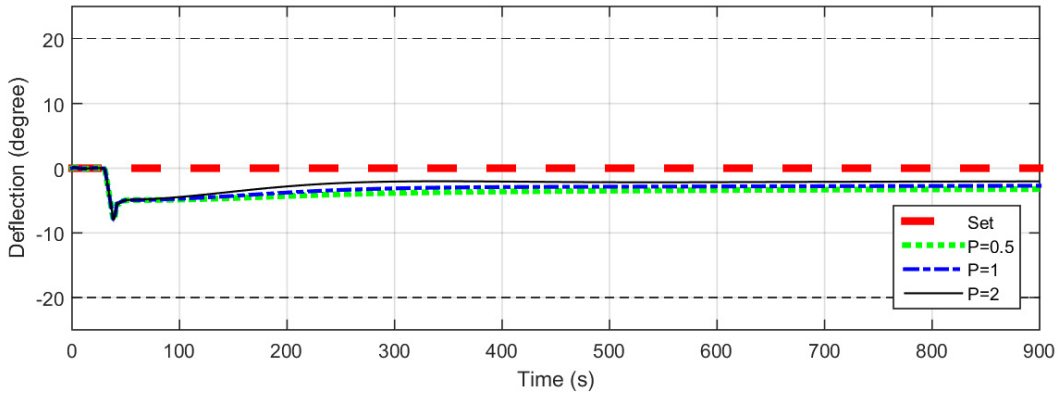


FIGURE 6.5 - PROPORTIONAL GAIN SELECTION ON $\alpha_{a\psi}$ FEEDBACK FOR VBS CONTROLLER

Figure 6.6 shows the result of repeating the AUV pitch simulation from Figure 6.1 using the new controller with the selected gain. As before, the pitch response seen in Figure 6.6 a) quickly achieves its set point while the aft deflection angle $\alpha_{a\psi}$ in Figure 6.6 b) is shown to quickly adjust in response to the step input as before. With the new control strategy the aft hydroplane deflection angle slowly reduces toward 0°.

The cause of the reduced deflection angle can be observed in Figure 6.6 c) where the VBS can be seen to slowly respond by increasing the aft VBS mass and reducing the fore VBS mass.

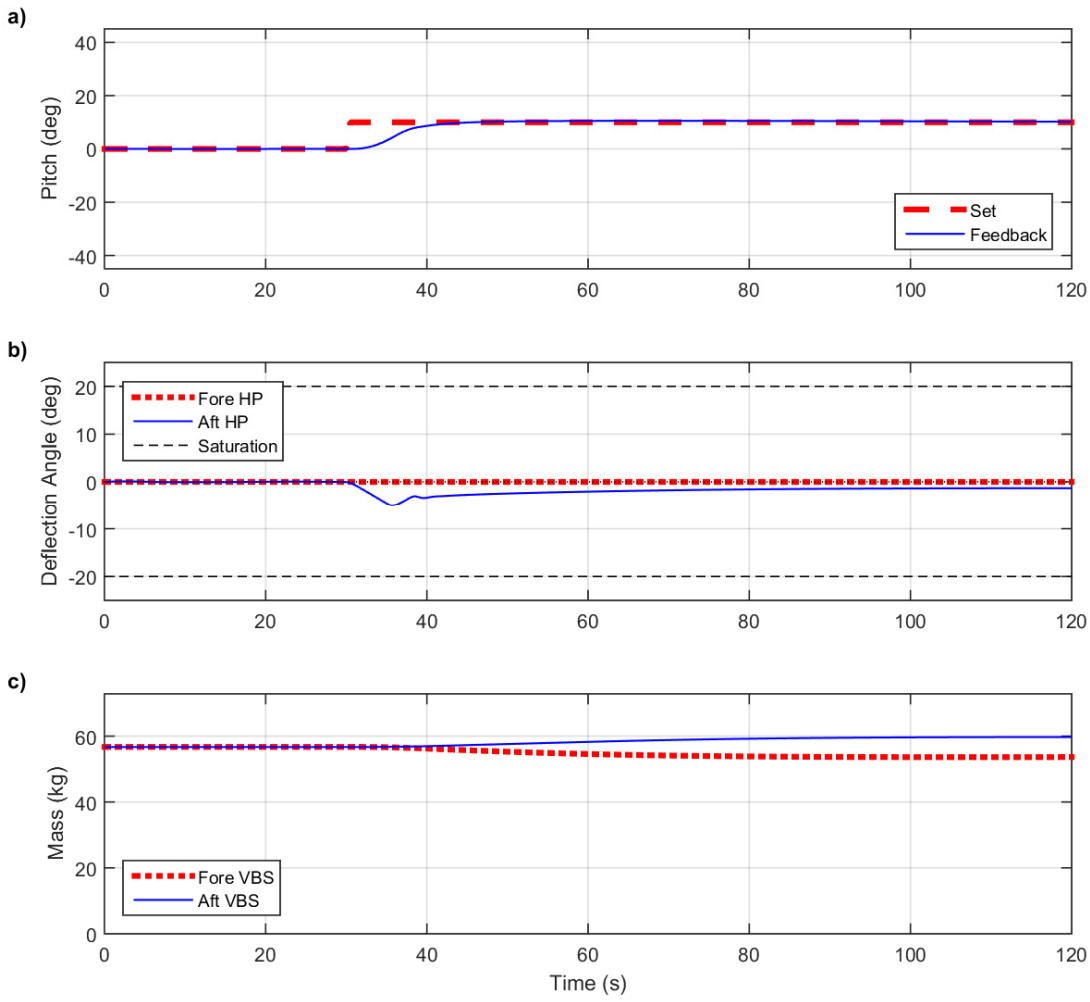


FIGURE 6.6 - INTEGRATED CONTROL AUV RESPONSE TO FIXED PITCH OF 20 DEGREES

Three different sets of gains were tested using the new controller for depth control. Figure 6.7 shows the results where each of these three sets of gains were tested. The tested gains were P=4, P=6 and a third added the integral term of I=0.01 along with a gain P=6. It can be seen that an increase in the proportional gain showed some improvement on the steady state error; however, the integral term was necessary to have a significant effect. Therefore, the gains of P=6 and I=0.01 were ultimately selected.

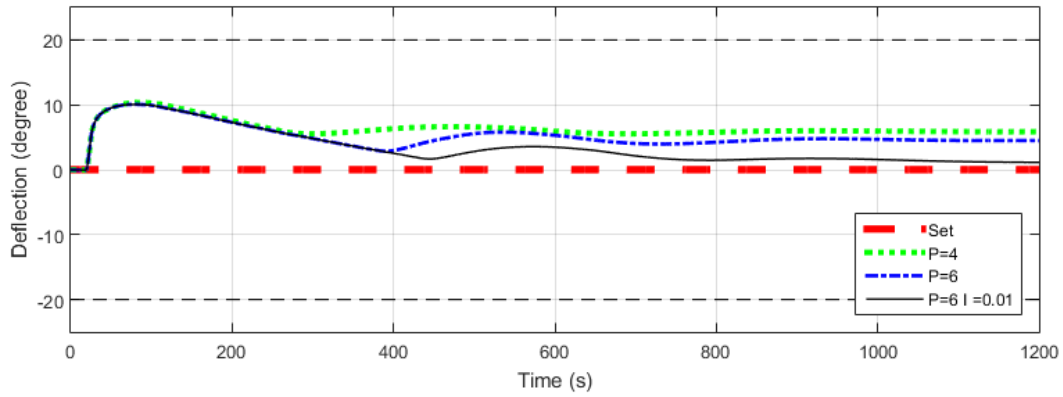


FIGURE 6.7 - GAIN SELECTION ON $\alpha_F$ FEEDBACK FOR VBS CONTROLLER

Figure 6.8 shows the result of repeating the AUV depth simulation shown in Figure 6.2 with the new controller and selected gains. Depth and pitch responses seen in Figure 6.8 a) and b) are the same as in the previous test; however, in Figure 6.8 c) instead of the fore deflection angle $\alpha_f$ reaching 15° and then holding level, the fore deflection angle reaches a maximum angle of just over 10° after which it decreases to approximately 5°.

Recalling from Equations (5.30) and (5.31), in order for the VBS mass to affect the AUV's pitch the masses of each of the fore VBS and aft VBS must be adjusted equally in opposite directions. Such a response can be seen in Figure 6.8 d) where the two masses are observed diverging at 300s at which time the aft deflection angle $\alpha_{a\psi}$ begins to reduce as well.

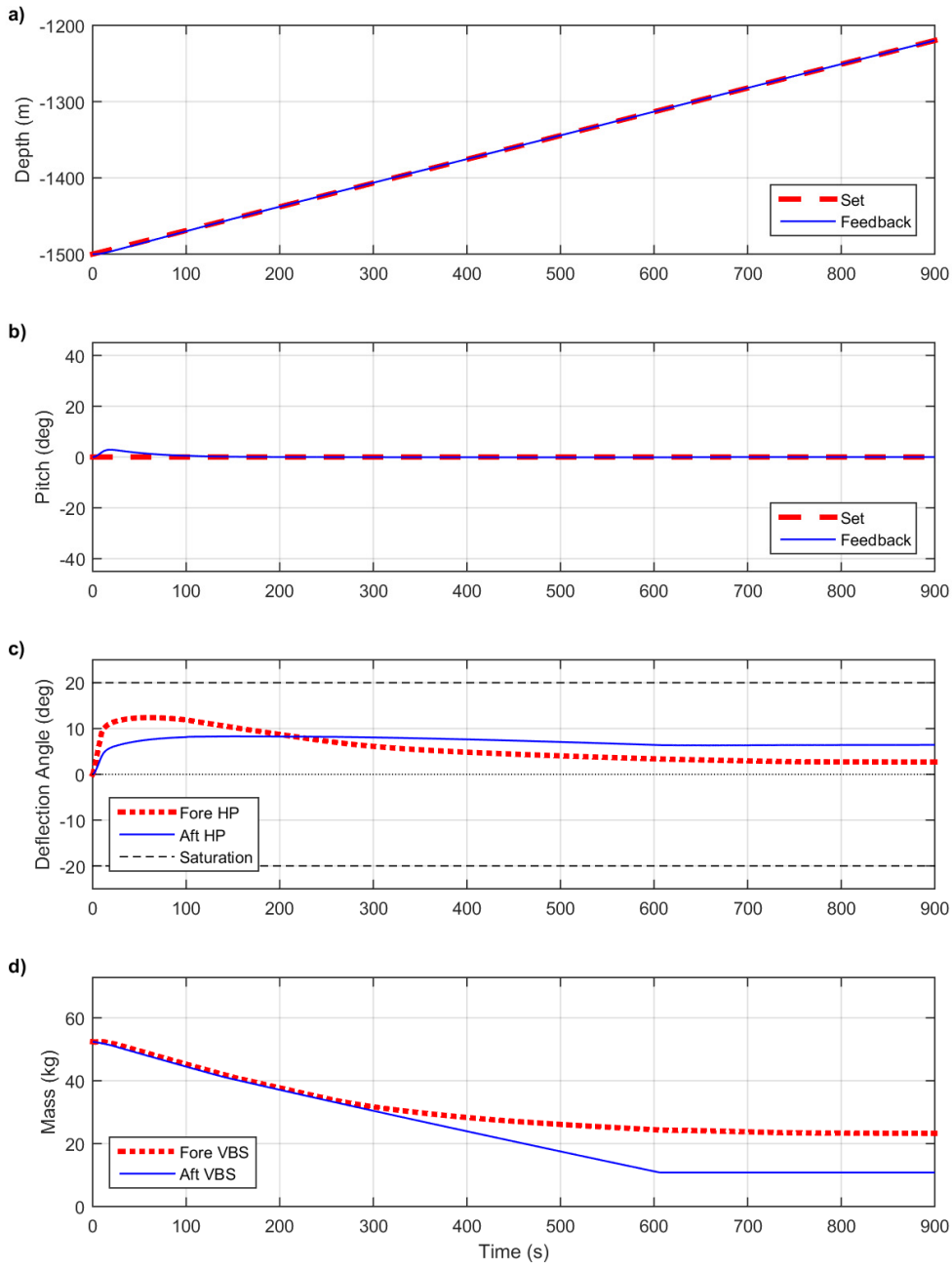


**FIGURE 6.8 - AUV RESPONSE FOLLOWING 15° INCLINE USING HP DEFLECTION ANGLE AS FEEDBACK FOR VBS RESULTING IN A REDUCTION IN THE HP DEFLECTION ANGLES AND LARGER RESPONSE FROM VBS THAN OBSERVED IN FIGURE 6.3**

While this controller appears to work well for these two scenarios, a new situation is now investigated where the hydroplanes are required to react to a frequently changing input as shown in Figure 6.9. The results of this scenario is shown in Figure 6.10 where the AUV performs bottom following on flat terrain with a sinusoid superimposed on the terrain having an amplitude of 2 m and a wavelength of 75 m.


FIGURE 6.9 - AUV TRAJECTORY: 0° INCLINE WITH SINUSOID

It can be seen that the resulting AUV depth shown in Figure 6.10 a), and pitch shown in Figure 6.10 b), remain stable operating about 0° as desired for the duration of the test. The deflection angles of the fore and aft hydroplanes, shown in Figure 6.10 c), similarly oscillate about 0° to attempt to follow the given path. With the newly proposed VBS controller, these hydroplane deflections are given as feedback to the VBS and the reaction of the VBS is to switch continuously between filling and emptying as shown in Figure 6.10 d). As an example of the power consumption estimate the value in this simulation from continuous filling and emptying gave a result of 339 kJ.

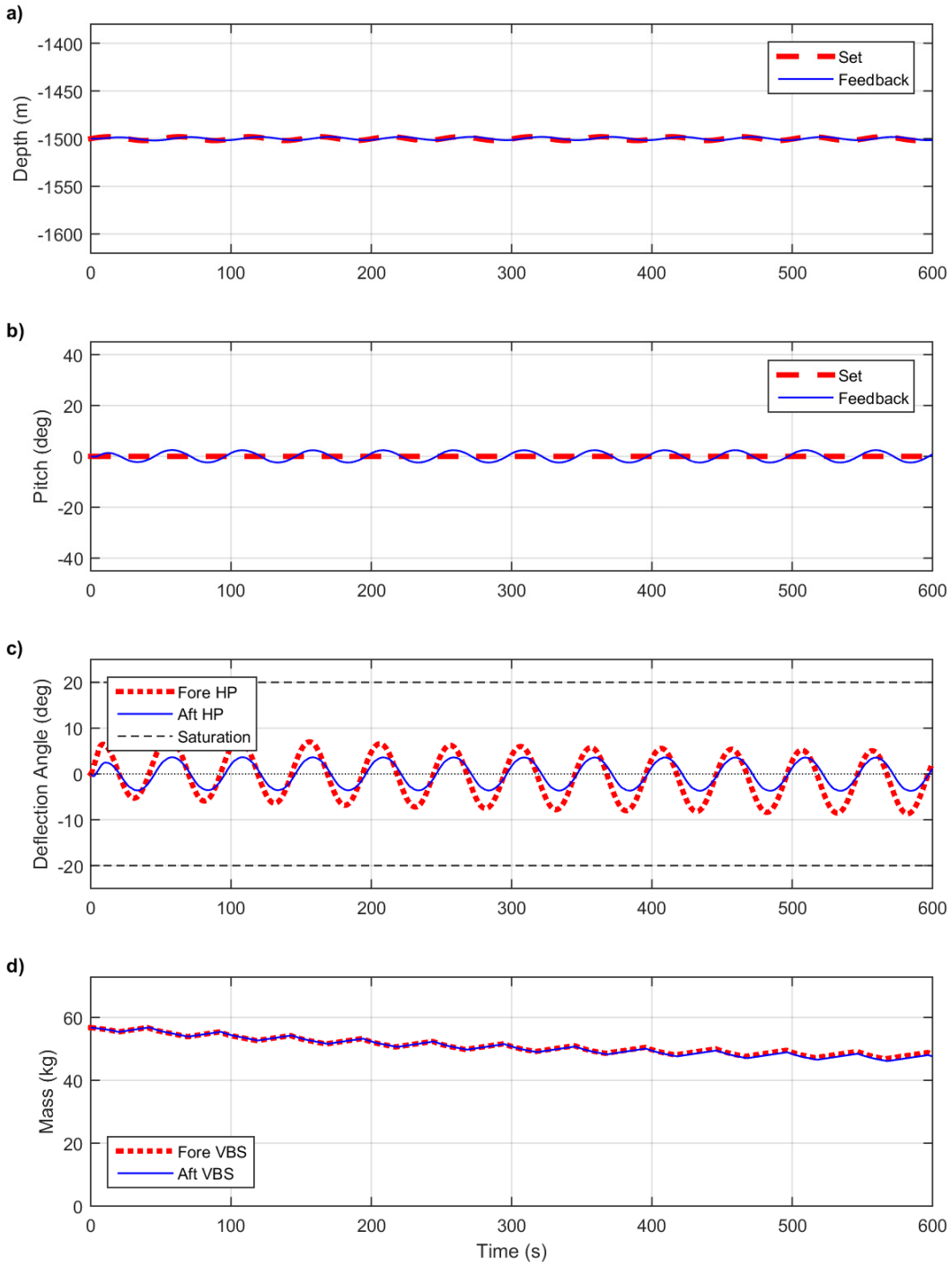


**FIGURE 6.10 - AUV FOLLOWING SINUSOID USING VBS WITH RAW HP DEFLECTION AS FEEDBACK RESULTING IN REPEATED FILLING AND EMPTYING OF VBS**

To try to reject these high frequency responses from occurring in the VBS a second-order Bessel filter was applied to the VBS reference control signal coming from the hydroplanes. Figure 6.11 re-plots on separate axes as solid lines the deflection angles of the fore hydroplanes (on top) and aft (on bottom) observed from the previous test seen in Figure 6.10. The effect of using filters with a passband frequency of 0.1 rad/s (dotted line) and 0.01 rad/s (dot-dash line) on these two signals are superimposed on Figure 6.11. The results of the lower frequency passband show a less fluctuating feedback signal for the VBS to follow and, therefore, this cut off frequency was selected for the filter.

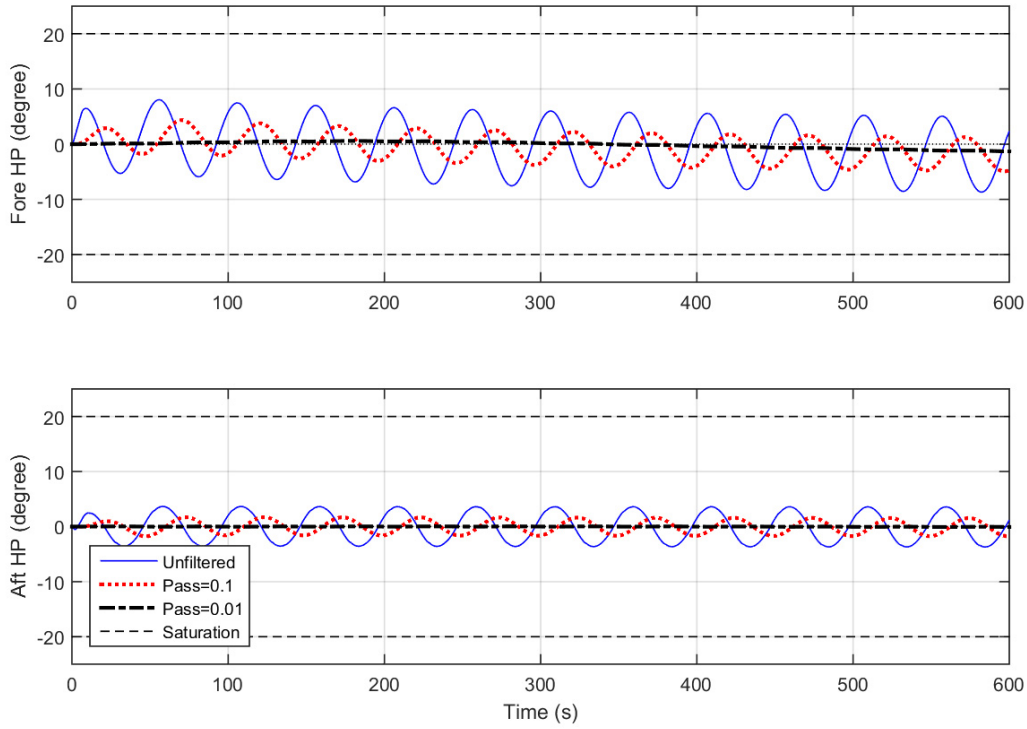


FIGURE 6.11 - FILTERED DEFLECTION RESULTS FROM BOTTOM FOLLOWING

Figure 6.12 demonstrates the effect of this filter on the VBS response when re-running the same bottom following test as in Figure 6.10. The response largely reflects that of the previous test with respect to the AUV depth, pitch, and hydroplane deflection angles; however, the VBS masses can be seen to change much less than in the previous

case. The inclusion of the filter corresponds to an overall reduction in power consumed by over 20% with a result of 264 kJ (from 339 kJ).

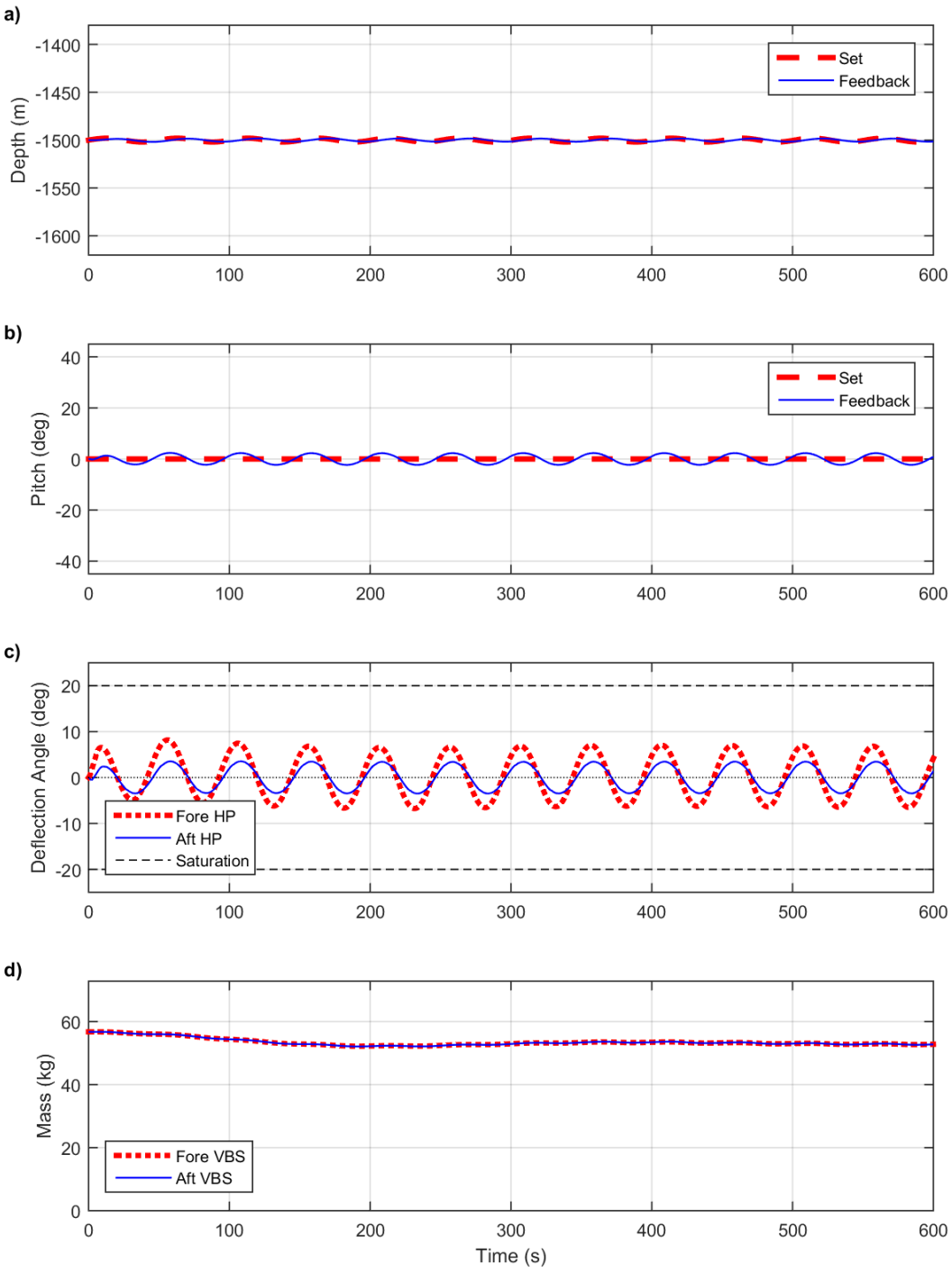


**FIGURE 6.12 - AUV FOLLOWING SINUSOID USING VBS WITH FILTERED HP DEFLECTION AS FEEDBACK RESULTING IN REDUCED RESPONSE OF VBS**

These results demonstrate the suitability of both the new control strategy (using deflection angle as feedback) and the use of the filter to reject higher frequency changes in these signals leaving the VBS to respond to low frequency changes.

## 6.3 Scenarios

With a new control strategy developed it is now possible to examine a series of simulation scenarios that demonstrate when the VBS may be used successfully. The following scenarios were selected as a non-exhaustive list of cases where the hydroplane control authority is enhanced through the use of VBS.

1. **Combined Incline with Sinusoid**: This simulation was selected to show the response of the AUV when presented with the combined trajectory of a 15° incline as depicted in Figure 6.2 and the sinusoid from Figure 6.9.
2. **Reduced Velocity**: The control authority of hydroplanes is a function of the square of the AUV's velocity (see Equation (2.39) ). Simulating the AUV using the same trajectory as in Figure 6.2 but at a lower velocity demonstrates this reduction in control authority.
3. **Continuous Mass Reduction**: Hydroplanes can compensate for changes in the AUV's mass; however, at the expense of control authority. One possible scenario is where the AUV is paying out wire resulting in a continuous reduction in the vehicle's mass.
4. **Increased Depth**: Net buoyancy of the AUV is affected by its depth (Figure 2.7). Without VBS the hydroplanes would need to maintain a fixed deflection angle just to hold to constant depth as seen in this scenario.

### 6.3.1 Combined Incline with Sinusoid

In this scenario the AUV is set to follow an incline of 15° with a superimposed sinusoid with an amplitude of 2 m and wavelength of 75 m as depicted in Figure 6.13. The pitch of the AUV is maintained at 0° again for this scenario while the vehicle rises to depth.

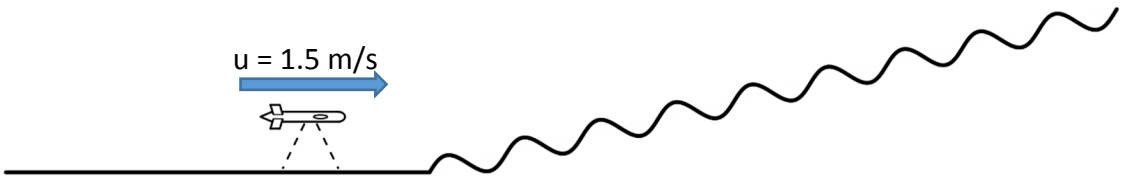


FIGURE 6.13 - AUV TRAJECTORY: 15° INCLINE WITH SINUSOID

The simulation results for this scenario without VBS can be see in Figure 6.14 and the result with VBS are shown in Figure 6.15. The depth and pitch feedback can be seen to closely follow the set values in Figure 6.14 a) and b). The fore hydroplane deflection $\alpha_y$ can be seen Figure 6.14 c) to repeatedly hit the saturation limit and, at steady state, oscillates about an average value of 15°. The aft deflection $\alpha_{a\psi}$, in turn, responds to a pitching moment to maintain a stable pitch closely reflecting the pattern of the fore deflection angle. At steady state the aft hydroplane oscillates about an average value of 8°. Finally, since the VBS is disabled no reaction is observed in Figure 6.14 d).

In Figure 6.15 the AUV is set again to follow an incline of 15° with the same superimposed sinusoid as used previously; however, now the new VBS controller is engaged. The AUV depth and pitch feedback can be seen to closely follow the set values in Figure 6.15 a) and b) as previously observed. The fore hydroplane deflection $\alpha_y$ can also be seen in Figure 6.15 c) to initially reach very high angles coming close to saturation; however, the mean deflection angle is now seen to slowly reduce as the VBS responds. The aft deflection angle $\alpha_{a\psi}$, in turn, responds to the coupled pitching moment to maintain a stable pitch closely reflecting the pattern of the fore deflection with a slight reduction in the mean value as time passes. Figure 6.15 d) shows the reaction of the VBS as the two masses (fore and aft) react to the fore hydroplane deflection angle $\alpha_f$.

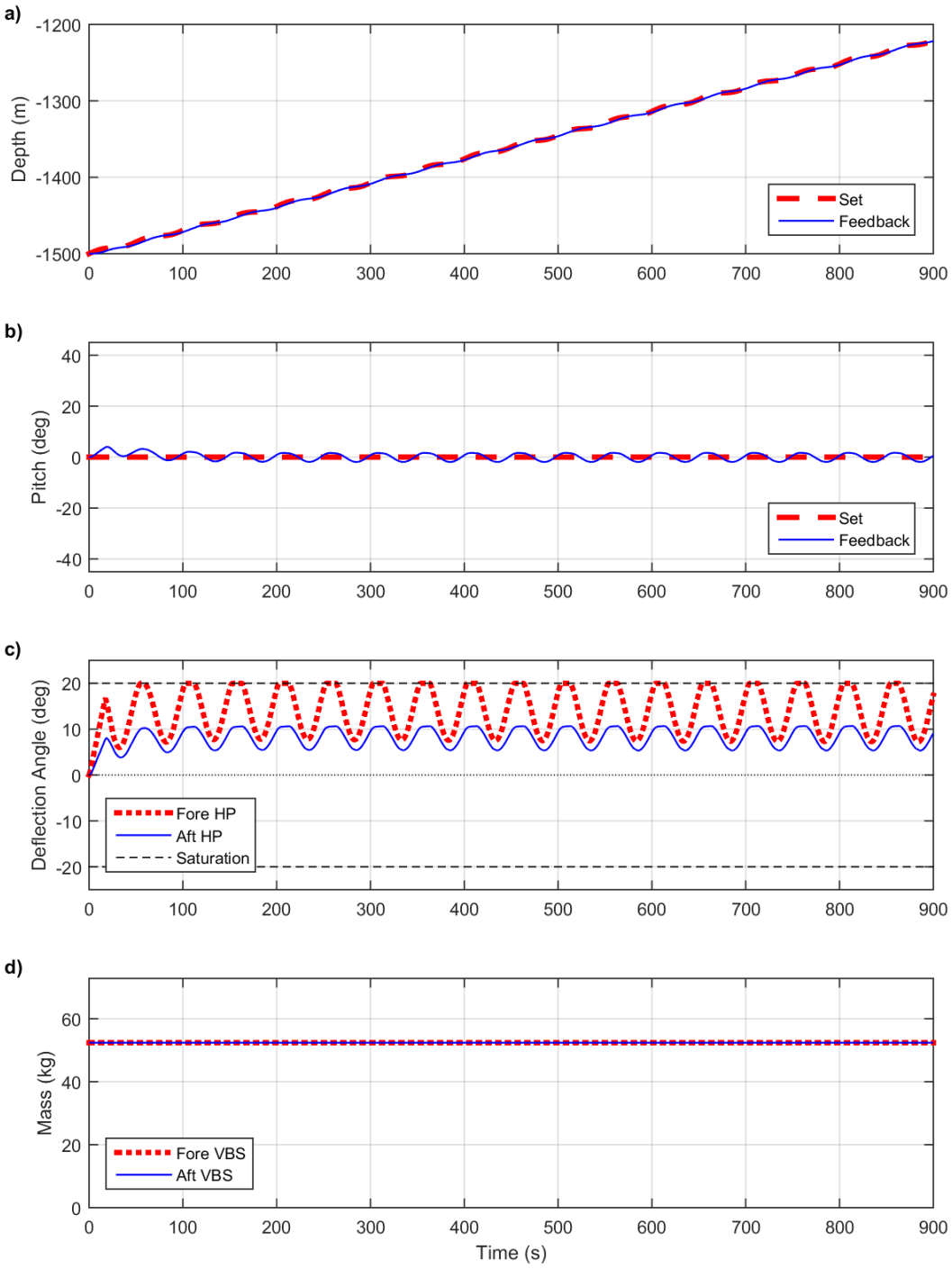


**FIGURE 6.14 - AUV RESPONSE FOLLOWING 15° INCLINE WITH A SUPERIMPOSED SINUSOID USING HYDROPLANES ONLY WITHOUT VBS. NOTICE THE LARGE MEAN HYDROPLANE DEFLECTIONS AND SATURATIONS.**

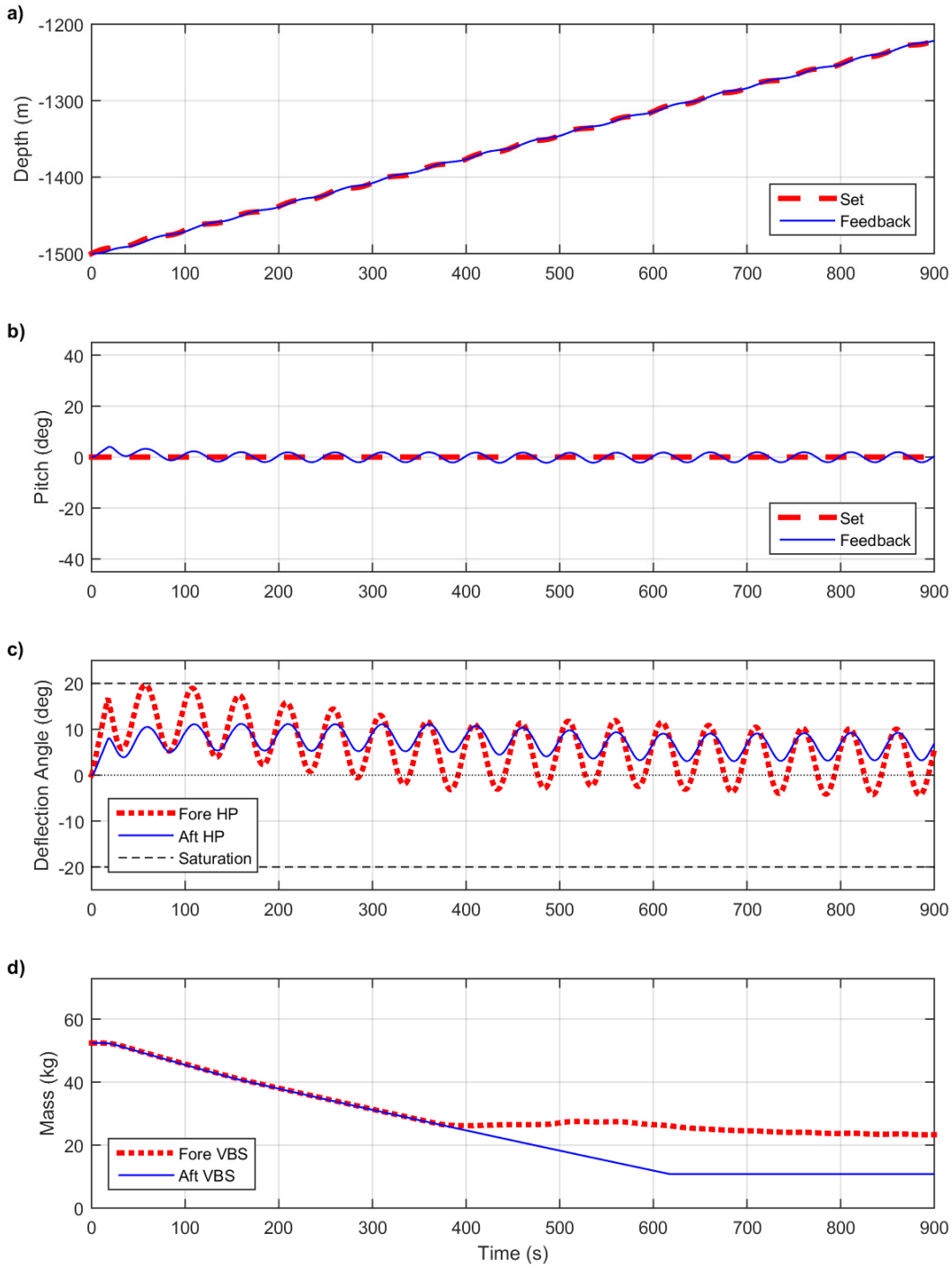


**FIGURE 6.15 - AUV RESPONSE FOLLOWING 15° INCLINE WITH A SUPERIMPOSED SINUSOID WITH HYDROPLANE AND VBS RESULTING IN REDUCTION OF MEAN DEFLECTIONS AND ELIMINATION OF SATURATIONS**

Figure 6.16 replots on a different axes the hydroplane deflection angle results from this incline test that uses the VBS. The upper portion shows the fore hydroplane deflection angle $\alpha_f$ with the filtered result reducing to approximately 5°, much less than the previous average result of 15° without the VBS. The lower plot shows the aft hydroplane deflection $\alpha_{a\psi}$ with its filtered result ending around a stable 6°, slightly lower than the average response of 8° seen in Figure 6.14.

As previously stated, the energy cost to utilizing the VBS can be significant. In this scenario the energy cost running with VBS was estimated to be 797 kJ which is significant in comparison to without the VBS which was estimated to be just 273 kJ, however, that this increased energy cost affords a significant increase in control authority of the hydroplanes.

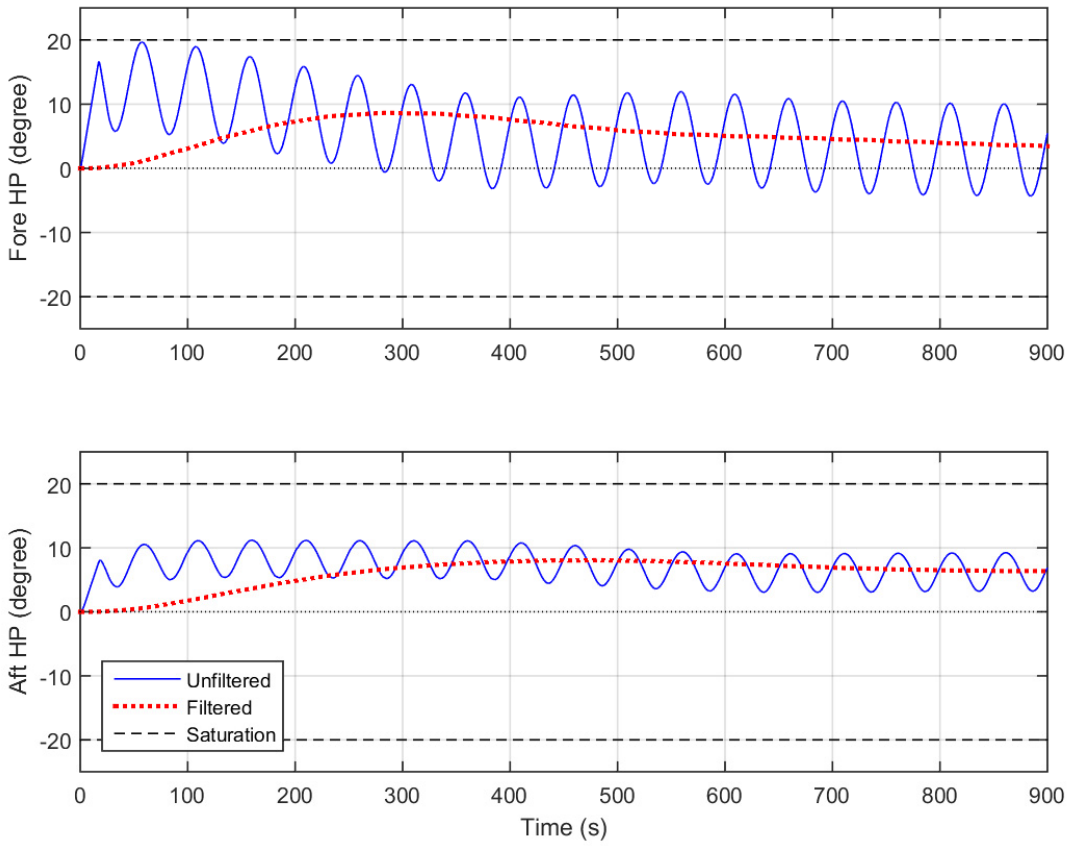


FIGURE 6.16 - HYDROPLANE DEFLECTION AND FILTERED RESULTS FROM TEST SEEN IN FIGURE 6.15

### 6.3.2 Reduced Velocity

Reducing the velocity of the AUV adversely affects control authority of the hydroplanes whose lift force is proportional to the square of the velocity (Equation (2.39)). An example of this reduced control authority can be seen in Figure 6.17 where the set velocity is reduced from 1.5 m/s to 1.2 m/s while following a 15° incline again rising to depth while maintaining a pitch of 0°.


**FIGURE 6.17 - AUV TRAJECTORY: 15° INCLINE AT REDUCED VELOCITY (1.2 M/S)**

Due to the decreased velocity the AUV has difficulty achieving the desired depth as the feedback depth diverges from the set depth over the course of the test in Figure 6.18 a). AUV pitch remains relatively stable for the course of the test which, save for an adjustment before 100s, remains at 0° as shown in Figure 6.18 b). The hydroplane angles both adjust significantly (Figure 6.18 c)) with the fore planes reaching 20° saturation around 60 seconds and the aft reaching 10° to hold the pitch. No response is commanded on the VBS for this test which remains constant in Figure 6.18 d).

Figure 6.19 shows the results of the same test utilizing the new VBS controller. Contrasting with the previous results it can be seen that the AUV is now able to achieve the desired depth closely following the set depth over the course of the test in Figure 6.19 a). AUV pitch, again, remains stable for the course of the test at 0° as shown in Figure 6.19 b). Unlike previously the fore hydroplane does not reach saturation in Figure 6.19 c), which becomes 3° after reaching a peak of approximately 15°. The aft planes also see a reduction starting at 350 seconds from 10° going down to 6°. Referring to Figure 6.19 d), with VBS enabled the fore and aft masses reduce uniformly until 350 seconds when the fore VBS diverges from the continued decline of the aft VBS due to

saturation. These simulation results demonstrate that the use of the new VBS controller has enabled the AUV to complete this maneuver successfully.

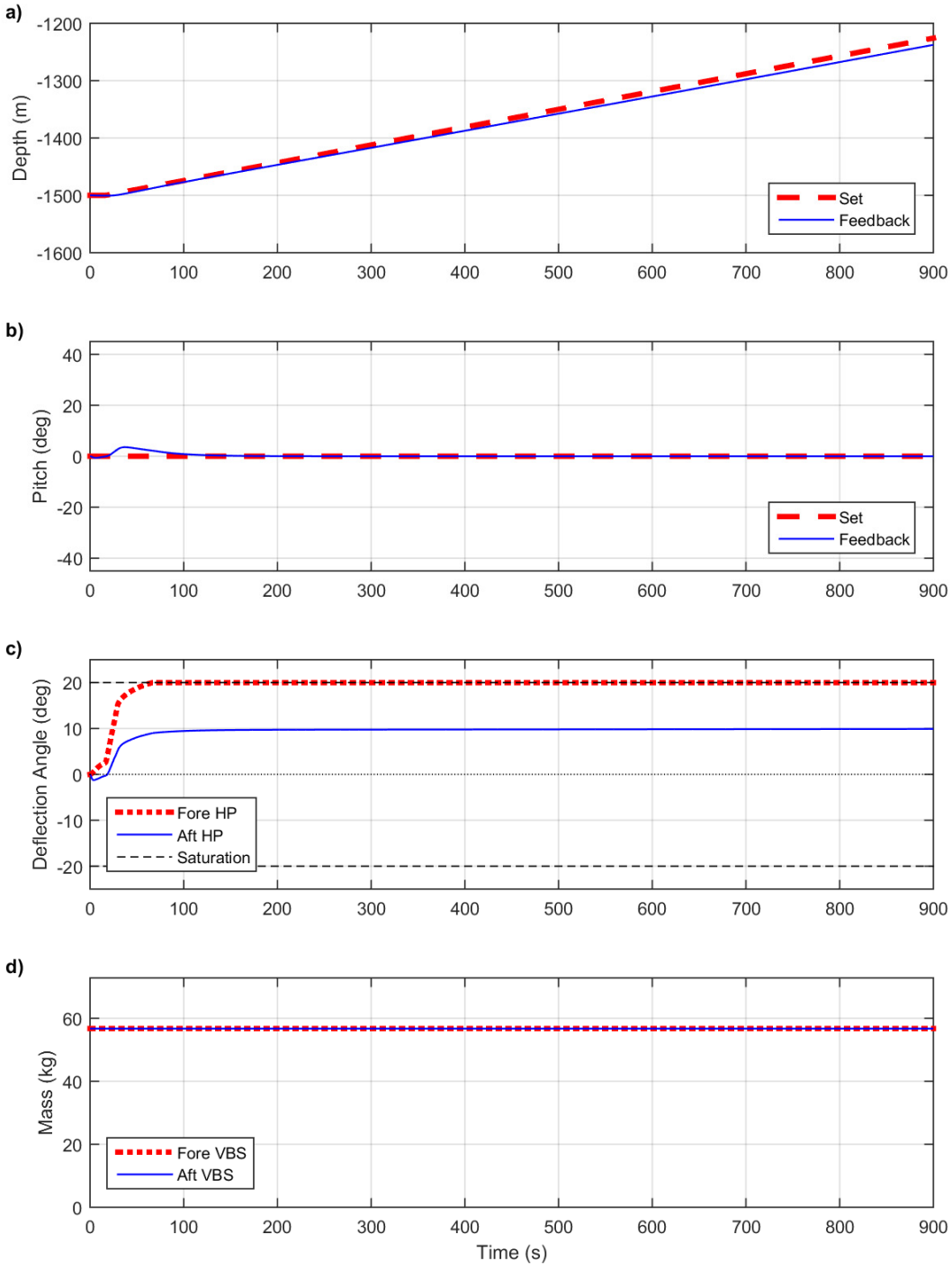


**FIGURE 6.18 - AUV RESPONSE FOLLOWING 15° INCLINE AT 1.2 M/S WITHOUT VBS REQUIRING THE AFT HP TO HOLD A LARGE FIXED DEFLECTION ANGLE AND THE FORE HP TO HOLD AT SATURATION**

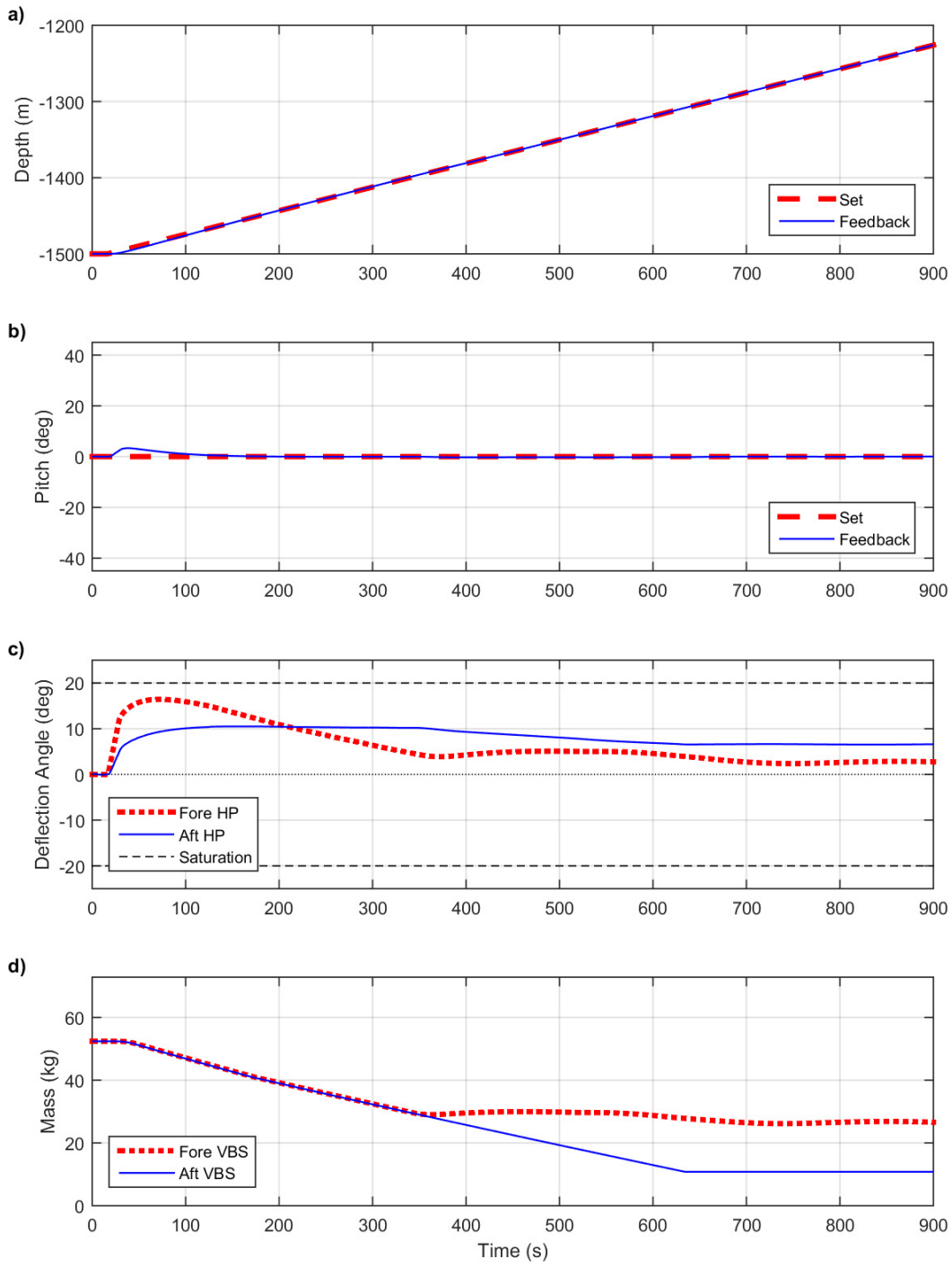


**FIGURE 6.19 - AUV RESPONSE FOLLOWING 15° INCLINE AT 1.2 M/S WITH VBS RESPONDING TO HP DEFLECTION ANGLE RESULTING IN A NOTICEABLE REDUCTION IN THE FORE HP DEFLECTION ANGLE OVER TIME**

### 6.3.3 Continuous Mass Reduction

Another scenario affecting hydroplane control authority occurs when there is a significant change in AUV mass. An example of this situation would be when the AUV is slowly deploying a cable for a cable laying or payload deployment mission as demonstrated in Figure 6.20.

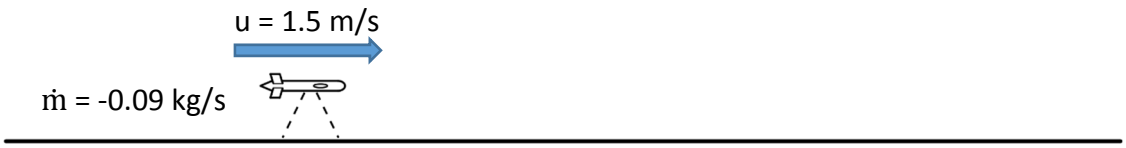


**FIGURE 6.20 - AUV TRAJECTORY: 0° INCLINE WITH CONTINUOUS DECREASE IN MASS OF 0.09 KG/S**

This scenario is explored in Figure 6.21 where the AUV is commanded to follow flat terrain while deploying the cable and gradually losing mass at a rate of 0.09 kg/s. For this test the VBS controller is not enabled and Figure 6.21 a) and b) show a steady depth and pitch until just past 900s when the AUV begins to ascend and its pitch can no longer be held at zero. The source of this change can be seen in Figure 6.21 c) where the fore hydroplanes continuously increase until they reach saturation and the AUV can no longer maintain its depth. At this time the AUV begins to ascend and requires the aft planes to react in an attempt to hold its pitch to zero. Finally, the change in load mass from the cable can be seen as a dashed line in Figure 6.21 d) where it reduces continuously from 80kg until it reaches 0kg. The mass of water in the VBS remains constant for the duration of the test as the VBS control system is not enabled.

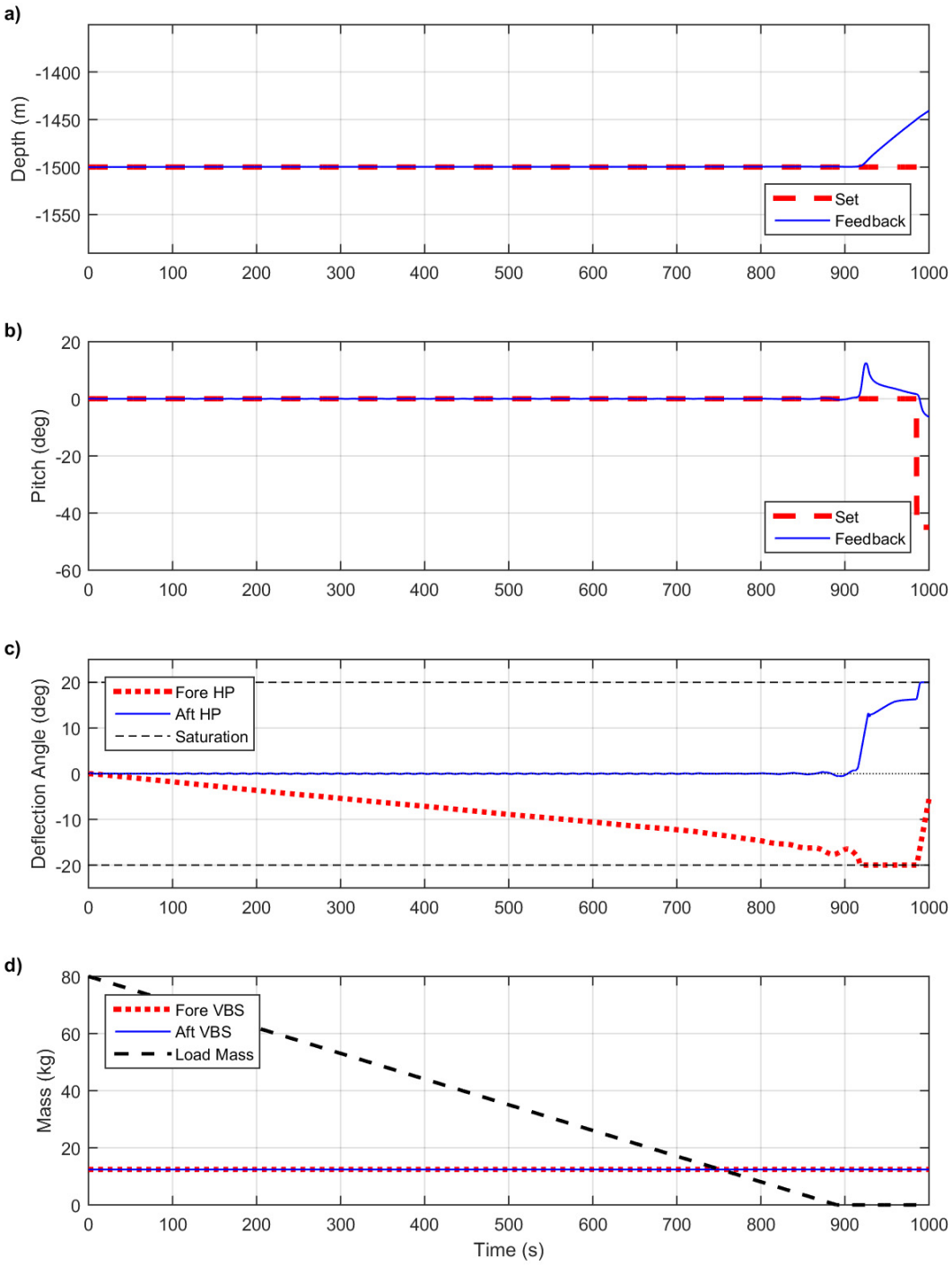


**FIGURE 6.21 - AUV HOLDING LEVEL WITH MASS CHANGE AND WITHOUT VBS RESULTING IN FAILURE AT CONCLUSION OF THE TEST**

Figure 6.22 shows the response of the AUV to the same conditions with the new VBS controller enabled. In this case both the AUV depth and pitch are kept stable throughout the entire test as seen in Figure 6.22 a) and b). Additionally, the fore deflection angle $\alpha_f$ remains close to 0° for the entirety of the test. The masses of the fore and aft VBS can be seen to increase to compensate for the change in the fore deflection angle. Again, the mass of the cable load reduces at a continuous rate from 80 kg to the minimum 0kg at a rate of 0.09 kg/s. The comparison of these results display an important application of where VBS can be used to maintain control of the AUV. Additionally, unlike many other situations this case also serves as an example of where the use of the VBS technology actually reduced the power consumption since it was estimated that only 409 kJ is required to operate with the VBS and 431 kJ is required without VBS control. It should be pointed out, however, that in this particular case the VBS is functioning primarily in free filling mode requiring much less energy than would be required if the pump were in use.

The results of this scenario demonstrate where the VBS responds to a slow change in the AUV's mass over time. Since the hydroplane deflection angle responds to these changes, among others, the hydroplane deflection angle provides an indirect method to measure the change in mass and the AUV responds to the change with an appropriate adjustment in VBS mass. As such no direct accounting for the change in mass is necessary as it is compensated for without further consideration.

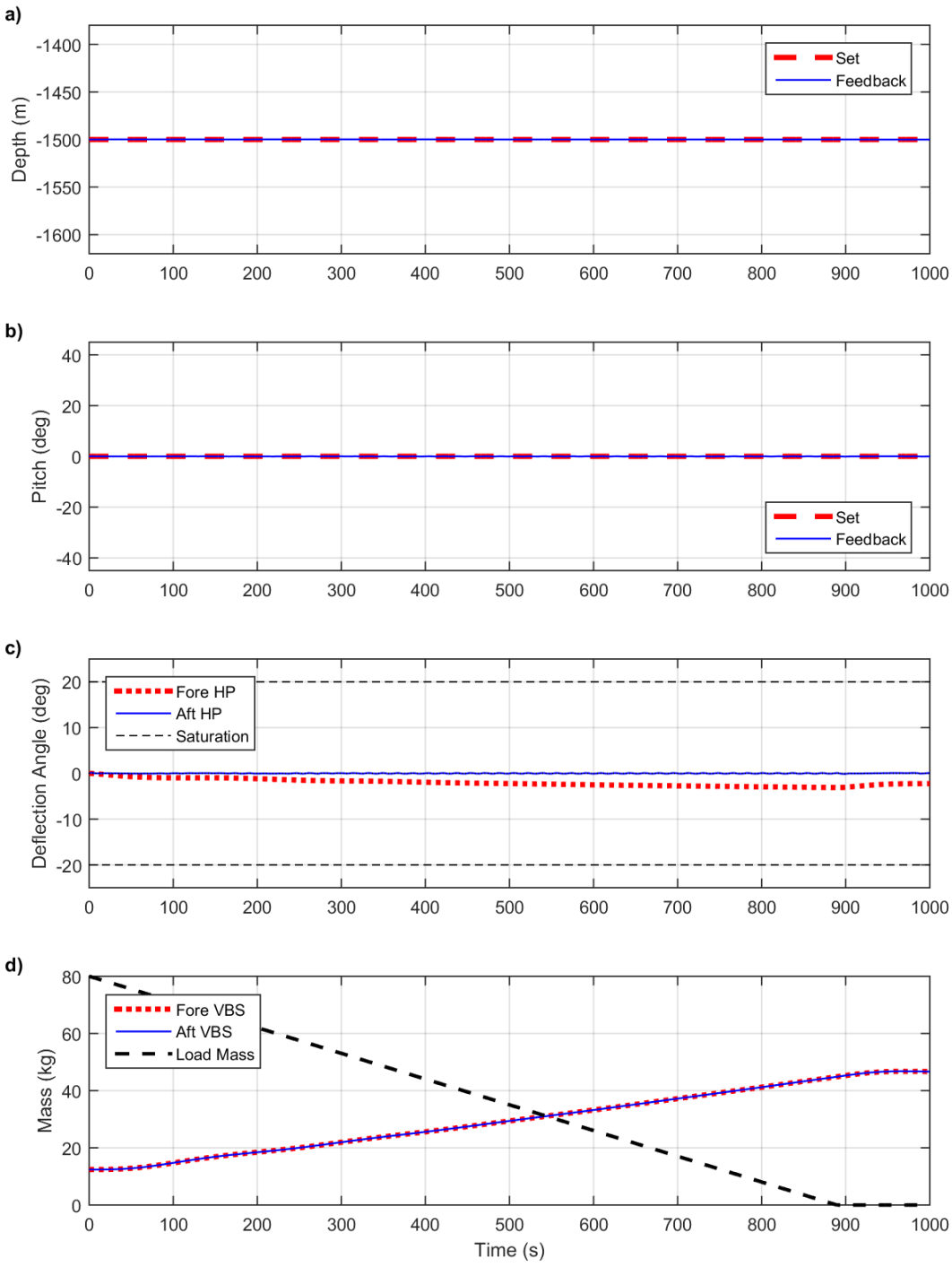


**FIGURE 6.22 - AUV HOLDING LEVEL WITH MASS CHANGE AND WITH VBS WHICH COMPENSATES FOR CHANGE IN MASS**

### 6.3.4 Increased Depth

When the AUV operates at an increased depth the buoyancy characteristic is affected by the increased pressure. For example, as seen in Figure 2.7, as AUV depth increases beyond 500 m, the net buoyancy becomes increasingly negative. Additionally, as depth increases the volumetric efficiency of the pump decreases which reduces the pump flow rate with increased external pressure. This loss in efficiency can be compensated for by increasing the pressure in the VBS tank; however, as seen in Chapter Chapter 5:, this response is limited when water pressure $P_w$ exceeds 15 MPa (equivalent to approximately 1500m deep). Figure 6.23 shows the execution of a simple flat bottom following test at 4000m depth with the results of the simulation with and without VBS enable shown in Figure 6.25 and Figure 6.24, respectively.

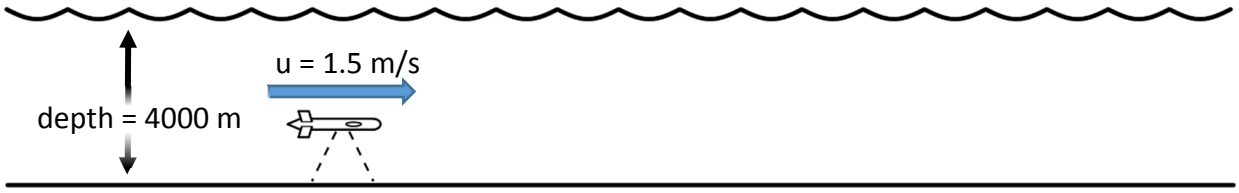


**FIGURE 6.23 - AUV TRAJECTORY: 0° INCLINE AT DEPTH OF 4000 M**

The AUV depth and pitch in Figure 6.24 a) and b) can be seen to hold steady at their set values. The fore plane deflection angle $\alpha_f$ can be seen in Figure 6.24 c) reacting to the AUV's downward motion due to the AUV being negatively buoyant at this depth. This angle $\alpha_f$ can be seen to increase until it reaches approximately 5° where it holds for the duration of the test. The aft hydroplane angle $\alpha_{a\psi}$ is seen to briefly react to hold the pitch to zero but otherwise holds steady at 0°. In Figure 6.24 d) the two VBS masses are seen to remain constant due to the VBS control system being disabled.

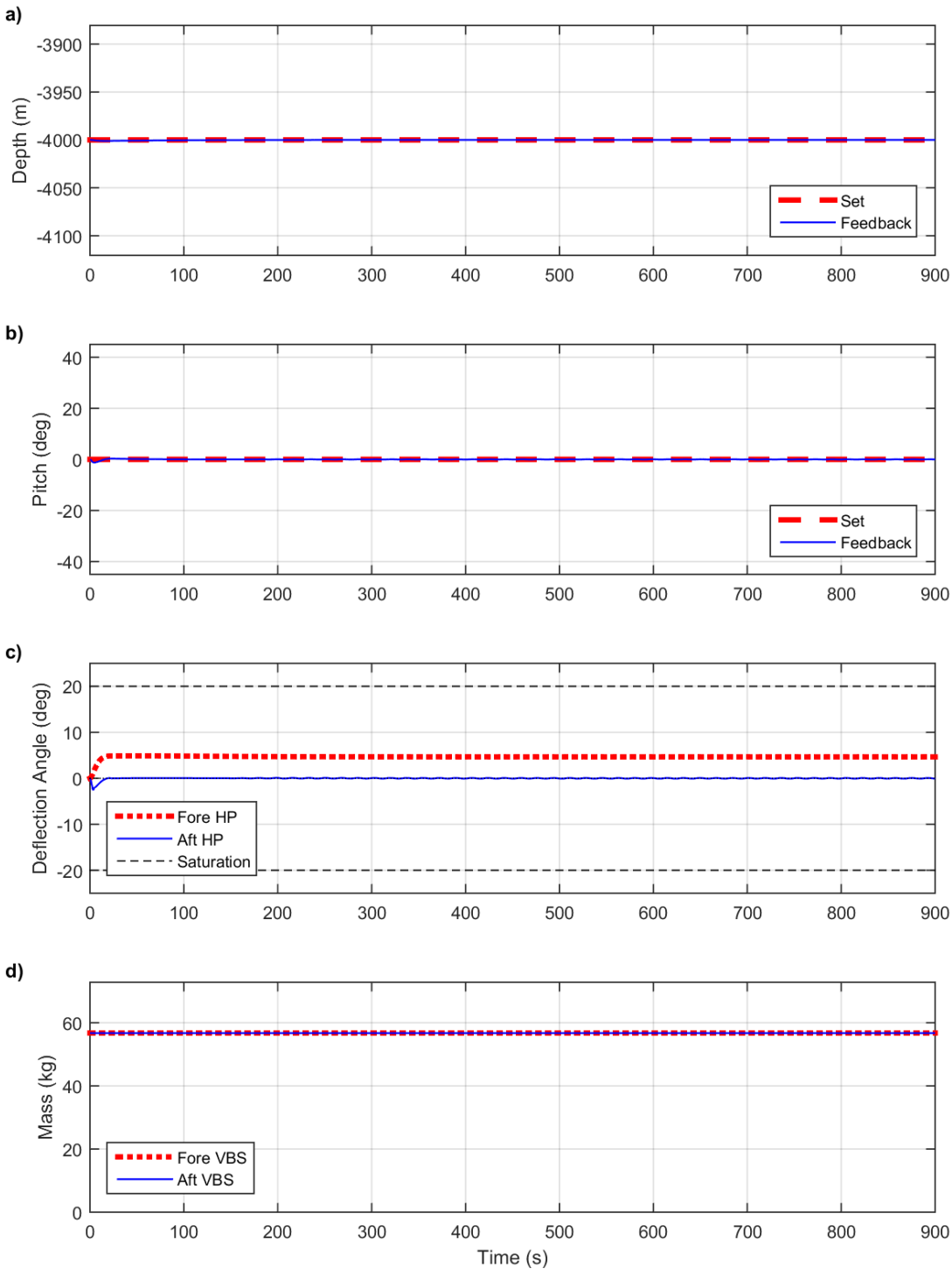


**FIGURE 6.24 - AUV HOLDING LEVEL AT 4000M WITHOUT VBS REQUIRING HP TO HOLD DEFLECTION ANGLE TO MAINTAIN DEPTH DUE TO REDUCTION DISPLACEMENT FORCE $F_{\Delta}$**

Figure 6.25 show the same test at 4000m deep using the new VBS controller. Again, AUV depth and pitch in Figure 6.25 a) b) can be seen to hold steady at their set values. The fore plane deflection angle $\alpha_f$ can be seen in Figure 6.25 c) increasing initially to 5° then reducing over time as it reacts to the AUV's downward motion due to its negative buoyancy at this depth. The aft hydroplane angle $\alpha_{a\psi}$ is seen to briefly react to hold the pitch to zero but otherwise it holds steady at 0°. The two VBS masses in Figure 6.25 d) are seen decreasing in response to the fore plane deflection and they eventually settle around 42 kg.

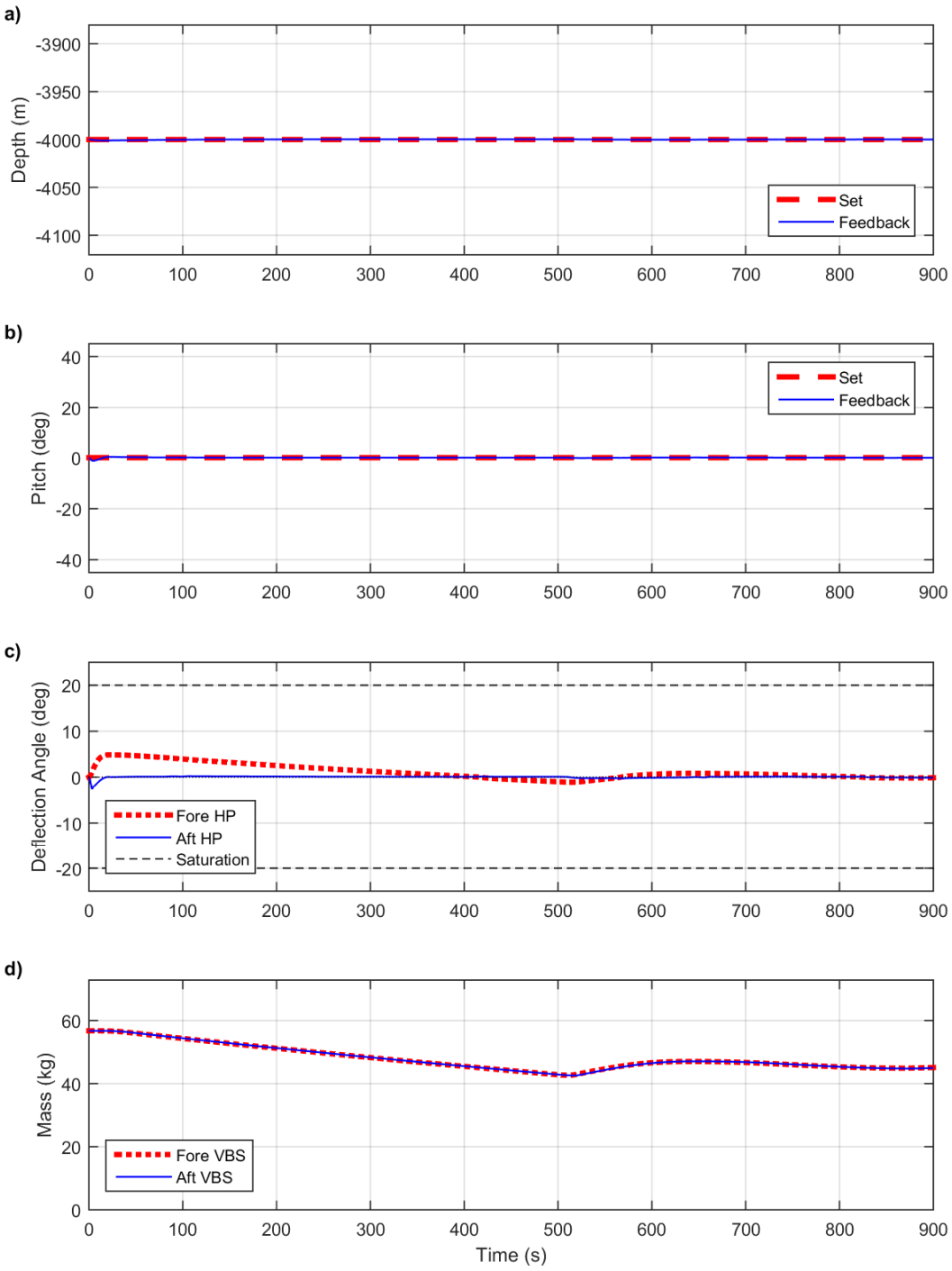


FIGURE 6.25 - AUV HOLDING LEVEL AT 4000M WITH VBS COMPENSATING FOR CHANGE IN BUOYANCY

# Chapter 7: Conclusion

In this thesis a 3D model of an AUV was developed in MathWork Simulink using the SimMechanics Toolbox with the inclusion of a dual variable ballast system. This model was first used to develop a control system for the AUV when it is just using its hydroplanes. Then the model was used to develop a control system for the AUV when it is just using the VBS. Finally, a control system was developed that can simultaneously use the hydroplanes and VBS inputs in tandem.

As in Woods [26], a seawater ballast system with high pressure air support was modelled. An improvement suggested was to include better flow calculations of the air and water through the valves in the VBS. This improvement was incorporated by the current author using a flow model based on the pressure difference across the valve.

To better understand the energy cost and gains contributed through the use of VBS a further contribution by the current author was the addition of a power consumption estimate. This estimate was used to calculate the energy use of the VBS controls and the AUV's other functions included in this model.

While developing a control strategy for the VBS a review of the previous high pressure air assist control used in Woods' work. This control mode was compared by the current author with three other modes of control to determine which strategies were more effective and efficient. The four modes investigated were:

| | |
|---|---|
| 1) **Static Volume** | Fixed volume of air in VBS Tank at low pressure |
| 2) **Expanded Volume** | Fixed larger volume of air at high pressure |
| 3) **High Pressure Air Assist** | Dynamic control of air pressure in VBS Tank through charging and venting |
| 4) **Regenerative Pressure Assisted** | Dynamic control of air pressure in VBS Tank through charging and recouping high pressure air back in charge tank |

The first two modes of control used fixed volumes and masses of air to regulate the pressure in the VBS tank; the first with a small volume and low mass and the second with a higher volume and much higher mass. Both these control modes were found to be energy efficient over a very narrow depth range.

The last two modes, having dynamic control over the pressure in the VBS tank, could make adjustments and be more efficient over a broader range of depths. The present author's proposed regenerative mode was found to be an improvement over the pressure assisted mode in two ways. Firstly, its power consumption was equal or better than that of the pressure assisted mode in all observed cases. Second, due to the design strategy air loss would be minimized by returning air back into the charge tank rather than venting it when the air pressure $P_a$ became too high.

Upon selection of the regenerative pressure air assisted mode a control strategy was successfully developed using the VBS to adjust the AUV's depth and pitch in isolation from the hydroplanes. Unfortunately, this control strategy proved unsuccessful when used in conjunction with the hydroplanes. This setback was due to the response rate of the hydroplanes being much faster than the VBS and, as such, the set point would be achieved before the VBS could adequately respond and no further response would be commanded to the VBS.

An alternative control strategy was therefore developed and investigated using the hydroplane defection as feedback to the VBS as a more direct measure of effort required. This new approach was found to be a successful scheme when introducing a low pass filter which rejected higher frequency responses from the hydroplanes. The result was a general improvement in the control authority of the hydroplanes as desired.

With this new control strategy in use, a series of scenarios were tested. The first was a test running the AUV up a 15° ramping bottom with a superimposed sinusoid. Results show that without the VBS, for the conditions used in this case study, the fore hydroplanes repeatedly hit saturation during the test. This saturation was later

alleviated in another test when the VBS control input was enabled. The result was an improvement in control authority but at the expense of a considerable increase in energy consumption. This frees up the control hydroplane authority to address perturbations and fine control.

Another scenario reduced the AUV velocity while climbing a 15° ramp. In this case, the result of the lower speed resulted in the AUV being incapable of following the desired depth profile. By adjusting the buoyancy through the use of the new VBS controller, however, the AUV was then shown to be able to achieve this profile.

A third trial experimented with the change in overall mass of the AUV which was simulated as a cable being payed out from the vehicle while maintaining a steady altitude. In this case, use of the new VBS controller was found to be critical since, without it, the vehicle began to rapidly ascend after the fore planes reached saturation. Interestingly, the power consumption was found to be less than with the VBS than without for the conditions used in this case study.

Finally, an increased depth trial was performed at 4000 m showing the need for the hydroplanes to be held at non-zero deflection to adjust for the change in buoyancy at this depth. The deflection angle was reduced to zero through the use of the VBS; however, at this increased depth the volumetric efficiency of the pump reduced greatly. As a result, the pump flow rate was considerably lower, reducing the VBS's response rate, and energy consumption was greatly increased.

## 7.1 Contributions

- A 3D model of an AUV was developed using the SimMechanics toolbox in Mathworks Simulink
- An improved air pressure control scheme (Regenerative Air Pressure Assist) was developed for the VBS which reduced air loss during use and showed better power consumption than the others reviewed

- Flow through the VBS valves was more accurately modelled compared to [10], [26]
- A new control strategy was developed using a filtered hydroplane deflection angle as feedback which permitted the control inputs of both the VBS and hydroplanes to work together
- Power consumption was included in the model to help estimate the cost of VBS and to make an informed trade-off between hydroplanes and VBS for certain scenarios

## 7.2 Recommendations

Power consumption remains the Achilles heel of the VBS, due to its high energy demand its continuous use may be difficult to justify when the AUV is not operating in conditions resulting in hydroplane angle saturation. As such, further investigations into optimizing the design and control of the VBS to reduce the power consumption of the system is still needed to make it a viable system for widespread use in AUVs.

For example, a control design investigation could be carried out so that the VBS responds to hydroplane feedback while limiting the response to only that required to prevent hydroplane angle saturation. This control approach could considerably reduce the power consumption in comparison with attempting to reduce the hydroplane to a zero mean deflection angle as performed in this thesis.

While energy consumption was reduced through the use of the regen air assist mode further investigation could be made to improve it. For example, this mode could be optimized more thoroughly by selection of tank pressures and volumes for specific operating depths. Additionally, selection of system components requiring less energy to operate such as mechanically-held valves could be considered.

Finally, as investigation into this control strategy has been done in the form of a computer simulation it would then be pertinent to implement it on hardware and perform field trials.

# References


[1] International Submarine Engineering, “Arctic Explorer Datasheet.” [Online]. Available: http://www.ise.bc.ca/pdfs/ISE_Arctic_Explorer_AUV_Datasheet_2012.pdf. [Accessed: 14-May-2016].

[2] A. L. Carroll, “Variable Ballast System Design for an Unmanned Submersible,” Masters Thesis, Massachusetts Institute of Technology, 1980.

[3] W. Defa, L. Yinshui, C. Jinyue, J. Zhuo, and J. Tao, “Research on the pump of seawater hydraulic variable ballast system in submersible,” presented at the 2011 International Conference on Fluid Power and Mechatronics (FPM), Beijing, 2011, pp. 429–434.

[4] M. Kemp, M. Palanza, C. Skibski, J. Ormsby, and M. Estaphan, “Persistence at full ocean depth,” presented at the 2012 IEEE/OES Autonomous Underwater Vehicles (AUV), Southampton, 2012, pp. 1–7.

[5] P. Motyka and E. Bergmann, “The design of a control system for the ballast and trim of an unmanned submersible,” presented at the American Control Conference, San Diego, 1984.

[6] P. A. DeBitetto, “Fuzzy logic for depth control of Unmanned Undersea Vehicles,” *IEEE J. Ocean. Eng.*, vol. 20, no. 3, pp. 242–248, Jul. 1995.

[7] P. J. Craven, R. Sutton, and R. S. Burns, “Control Strategies for Unmanned Underwater Vehicles,” *J. Navig.*, vol. 51, no. 1, pp. 79–105, 1998.

[8] R. K. Lea, R. Allen, and S. L. Merry, “A comparative study of control techniques for an underwater flight vehicle,” *Int. J. Syst. Sci.*, vol. 30, no. 9, pp. 947–964, Jan. 1999.

[9] S. Tangirala and J. Dzielski, “A Variable Buoyancy Control System for a Large AUV,” *IEEE J. Ocean. Eng.*, vol. 32, no. 4, pp. 762–771, 2007.

[10] S. A. Woods, R. J. Bauer, and M. L. Seto, “Automated Ballast Tank Control System for Autonomous Underwater Vehicles,” *IEEE J. Ocean. Eng.*, vol. 37, no. 4, pp. 727–739, Oct. 2012.

[11] Y. Liu, X. Zhao, D. Wu, D. Li, and X. Li, “Study on the control methods of a water hydraulic variable ballast system for submersible vehicles,” *Ocean Eng.*, vol. 108, pp. 648–661, Nov. 2015.

[12] T. I. Fossen, *Guidance and control of ocean vehicles*. Chichester; New York: Wiley, 1994.

[13] F. P. Beer, E. R. Johnston, and G. W. Brown, *Vector mechanics for engineers. Dynamics*. Boston [etc.]: McGraw-Hill, 1997.

[14] J. N. Newman, *Marine hydrodynamics*. Cambridge, Mass.: MIT Press, 1977.

[15] E. E. Allmendinger, *Submersible vehicle systems design*. Jersey City, N.J.: Society of Naval Architects and Marine Engineers, 1990.

[16] J. A. Knauss, *Introduction to physical oceanography*, 2.ed., Reissued. Long Grove, Ill: Waveland Press, 2005.

[17] B. R. Munson, D. F. Young, and T. H. Okiishi, *Fundamentals of fluid mechanics*, 3rd ed. update. New York: J. Wiley, 1998.

[18] W. K. Bullivant, “Tests of the NACA 0025 and 0035 Airfoils in the Full-Scale Wind Tunnel,” NASA Center for AeroSpace Information (CASI), 708, 1941.

[19] V. Bakaric, Z. Vukic, and R. Antonic, “Improved basic planar algorithm of vehicle guidance through waypoints by the line of sight,” presented at the First International Symposium on Control, Communications and Signal Processing, Tunisia, 2004, pp. 541–544.

[20] Z. Qiu, “Design and research on a variable ballast system for deep-sea manned submersibles,” *J. Mar. Sci. Appl.*, vol. 7, no. 4, pp. 255–260, Mar. 2009.

[21] S. S. Zumdahl, *Chemical principles*, 3rd ed. Boston: Houghton Mifflin Co, 1998.

[22] L. S. Marks, *Marks’ standard handbook for mechanical engineers*, 11. editon, [90. anniversary edition]. New York, NY: McGraw-Hill, 2007.

[23] Hydrocon Subsea, “Ocean Submersible Solenoid Valve.” [Online]. Available: http://www.hydracon.com/wp-content/uploads/2014/11/Npa1703-201H.pdf. [Accessed: 23-May-2016].

[24] Praxair, “Nitrogen N2 Spec Sheet.” [Online]. Available: http://www.praxair.com/~/media/praxairus/Documents/Specification%20Sheets%20and%20Brochures/Gases/Nitrogen/Nitrogen%20N2%20Spec%20Sheet%20SS%20P4631.pdf?la=en. [Accessed: 20-May-2016].

[25] Ingersoll Rand, “Reciprocating Compressor.” [Online]. Available: http://www.ingersollrandproducts.com/air/catalogs/Small%20Recip%20ESA%20Family%20Brochure_A4.pdf. [Accessed: 14-May-2016].

[26] S. Woods, “Automated Ballast Tank Control System for Autonomous Underwater Vehicles,” Thesis, Dalhousie University, 2012.

# Appendix A: AUV Model Validation

With the AUV sufficiently defined, a series of validation tests were run to ensure a sound model. For these tests the following conditions were set:

- center of gravity was placed at the center of buoyancy
- buoyancy force was set to neutral ignoring any dynamic effects of depth
- water density was set to the surface value (1022.7 kg/$m^3$)
- control inputs were all set to neutral including:
    - hydroplanes
    - VBS mass
    - thrust

By setting the center of bouyancy and center of gravity to coincide, the restoring force, shown in Figure 2.5, is eliminated which could otherwise detract from the hydrodynamic forces being observed. With buoyancy neutral, the vehicle will not unexpectedly begin to ascend or descend and similarly the control set to neutral prevents motion not originating from the applied force or moment.

For observing each applied force or moment, three different tests were performed which are labeled and described as follows:

| | |
|---|---|
| **Body Force** | Simulation includes only the drag forces on the AUV body |
| **Hydroplane Force** | Includes the Body Force as well as the forces generated by the hydroplanes at neutral deflection |
| **Addedmass** | Incoporates the previous forces and adds the effect of the virtual added mass |

In all cases, the forces or moments are applied in the body fixed frame and observed for a duration of 30 seconds.

## A.1 Force in X Direction

The results of a test with a 25 N force in the X direction which would correspond to a velocity u of approximately 1 m/s can be seen in Figure A.1. This figure is divided as

follows: Figure A.1 a) and b) show the AUV translational and angular (pitch only) positions, Figure A.1 c) and d) show the AUV translational and angular (pitch only) velocities, while Figure A.1 e) and f) show the AUV translational and angular accelerations (pitch only). For each of the charts the results display the values in the X, Y and Z directions showing the effect of the body forces, hydroplane forces and added mass.

***Body Force***

The reaction of the system with only the effects of hydrodynamic forces on the AUV body is displayed in Figure A.1 as a thick green line. This reaction can be seen to result in an instantaneous translational acceleration $\dot{u}$ in Figure A.1 e). The corresponding velocity $u$ is then seen in Figure A.1 c) to increase which in turn results in an increase in $x$ as seen in Figure A.1 a).

***Hydroplane Force***

A dashed red line is used in Figure A.1 to display the effects of also including the forces of drag from the hydroplanes in addition to the body. The result is seen to increase the total drag force observed as a reduction in the acceleration $\dot{u}$ in Figure A.1 e). With lower acceleration, a slower velocity $u$ and a shorter distance travelled in the $x$ is then found in Figure A.1 c) and a), respectively.

***Added Mass***

The final effect of the virtual added mass is displayed in Figure A.1 as a thinner blue line. The result from increasing the mass is seen in Figure A.1 e) to decrease acceleration $\dot{u}$ consequentially decreasing the observed velocity $u$ and position $x$ in Figure A.1 c) and a) respectively.

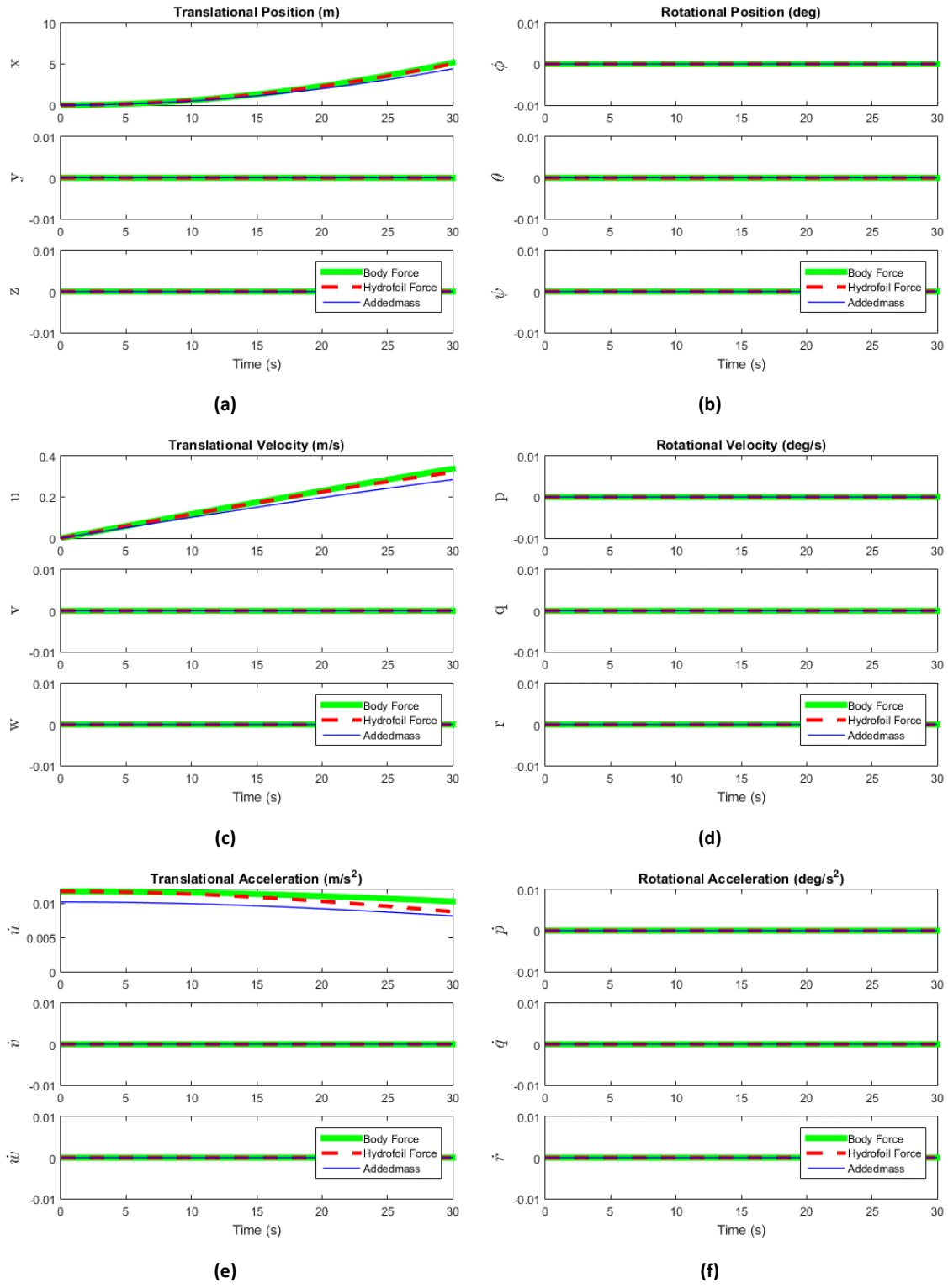


FIGURE A.1 - 6 DOF POSITION, VELOCITY AND ACCELERATION SIMULATION RESPONSE TO 25 N FORCE IN X DIRECTION

To ensure a reasonable result a simple one-dimensional simulation was performed as an estimate. The position after each time step $x_{k+1}$ was calculated using Equation (A.1) by adding the change from the previous position $x_k$ due to the velocity $u_k$ and acceleration $\dot{u}_k$ at the previous time step. Similarly the velocity $u_{k+1}$ was calculated using Equation (A.2) from the previous step's velocity and acceleration. The force $F_{k+1}$ was calculated using Equation (A.4) from the applied force $X_a$ and the drag force $X_D$ which in turn was calculated from the previous velocity per the drag Equation (2.19). Acceleration was then calculated using Equation (A.3) from the previous force $F_k$ divided by the mass $m$.

$$x_{k+1} = x_k + u_k T + 0.5\, \dot{u}_k T^2 \tag{A.1}$$

$$u_{k+1} = u_k + \dot{u}_k T \tag{A.2}$$

$$\dot{u}_{k+1} = \frac{1}{m} F_k \tag{A.3}$$

$$F_{k+1} = X_a - X_D \tag{A.4}$$

Table A.1 shows the position $x$, velocity $u$, and acceleration $\dot{u}$ for this numerical estimate as well as the corresponding Simulink model. This table displays the comparison of the results of both the Simulink model and this numerical estimate with only the body forces applied. The results for acceleration $\dot{u}$ seen in the far right column are in perfect agreement. Velocity $u$ in the second last column are very close; however errors introduced due to a larger time step than the Simlink model in the numeric estimate are observable. Finally, the x position, which utilizes both the acceleration and velocity as it is calculated in Equation (A.1), accumulates further differences. Nevertheless, the results of both the Simulink model and numeric estimate are still very close . Consequently, the Simulink model captures the essential aspects of forward motion for the AUV.

TABLE A.1 - X FORCE SIMULATION ESTIMATED VS OBSERVED WITH BODY FORCES

| | $x$ (m) | $u$ (m/s) | $\dot{u}$ (m/s²) |
|---|---|---|---|
| SIMULINK MODEL | 5.170 | 0.337 | 0.010 |
| ESTIMATE | 5.177 | 0.338 | 0.010 |

## A.2 Force in Y Direction

The results of a test applying a force $Y_a$ of 25 N to the vehicle in the Y body frame direction can be seen in Figure A.2 which is arranged the same as Figure A.1. Unlike applying a force in X direction, the Y-direction force results in unballanced forces whose effects can be seen as motion in the X direction in Figure A.2 a) and rotation about the Z axis in Figure A.2 b).

***Body Force*** ——————————

The reaction of the system to a force in the Y direction is similar to that in the X direction. Initially the system accelerates as seen in Figure A.2 e) due to the applied force. This acceleration $\dot{v}$ then reduces as the velocity $v$ increases as seen in Figure A.2 c) creating a counter-acting drag force. During this time the y position becomes increasingly negative as seen in Figure A.2 a) due to the velocity $v$ maintaining its downward direction.

***Hydroplane Force*** - - - - - - - - - - - - - - - - - - - -

Including the effect of the hydroplanes causes minimal changes from the previous test for motion in the Y direction (as intuitively expected based on the relative magnitudes). The additional drag force results in acceleration $\dot{v}$ decreasing to zero sooner than seen previously in Figure A.2 e). Consequentially a lower maximum velocity $v$ is observed in Figure A.2 c) and the movement along $y$ is much less as seen in Figure A.2 a), as expected.

The motion in directions other than Y are due to the hydroplane drag force creating a moment about the Z axis. This moment is created by the hydroplane drag forces being applied offset from the center of pitch rotation causing an acceleration $\dot{r}$. The acceleration seen in Figure A.2 f) begins at zero and increases with the translational velocity $v$. As the rotational velocity $r$ increases in Figure A.2 d) a counter-acting drag force about the Z axis is created reducing the rotational acceleration $\dot{r}$.

***Added Mass***

Including the effect of added mass yields results that are similar to the last two scenarios in the Y direction; however, due to the mass dynamically being greater, the initial acceleration $\dot{v}$ is observed to be lower in Figure A.2 e). Correspondingly, the velocity $v$ is diminished and the distance travelled in the $y$ is less which can be seen in Figure A.2 c) and a).

The more noticeable difference commences with an initial pitch acceleration $\dot{r}$ in Figure A.2 f). The added mass, which has its center of mass aft of the origin, creates a moment which, in turn, causes this rotational acceleration. This acceleration results in the rotational velocity $r$ which increases over time as seen in Figure A.2 d). The velocity in turn creates a counter-acting drag force about the Z axis and continues to increase with velocity r until it neutralizes the effect of the moment created by the added mass.

As rotation in the added mass test is higher than with just the hydroplane forces motion in the local Z direction are reflected in movement in the inertial X direction as the angle $\psi$ becomes larger.

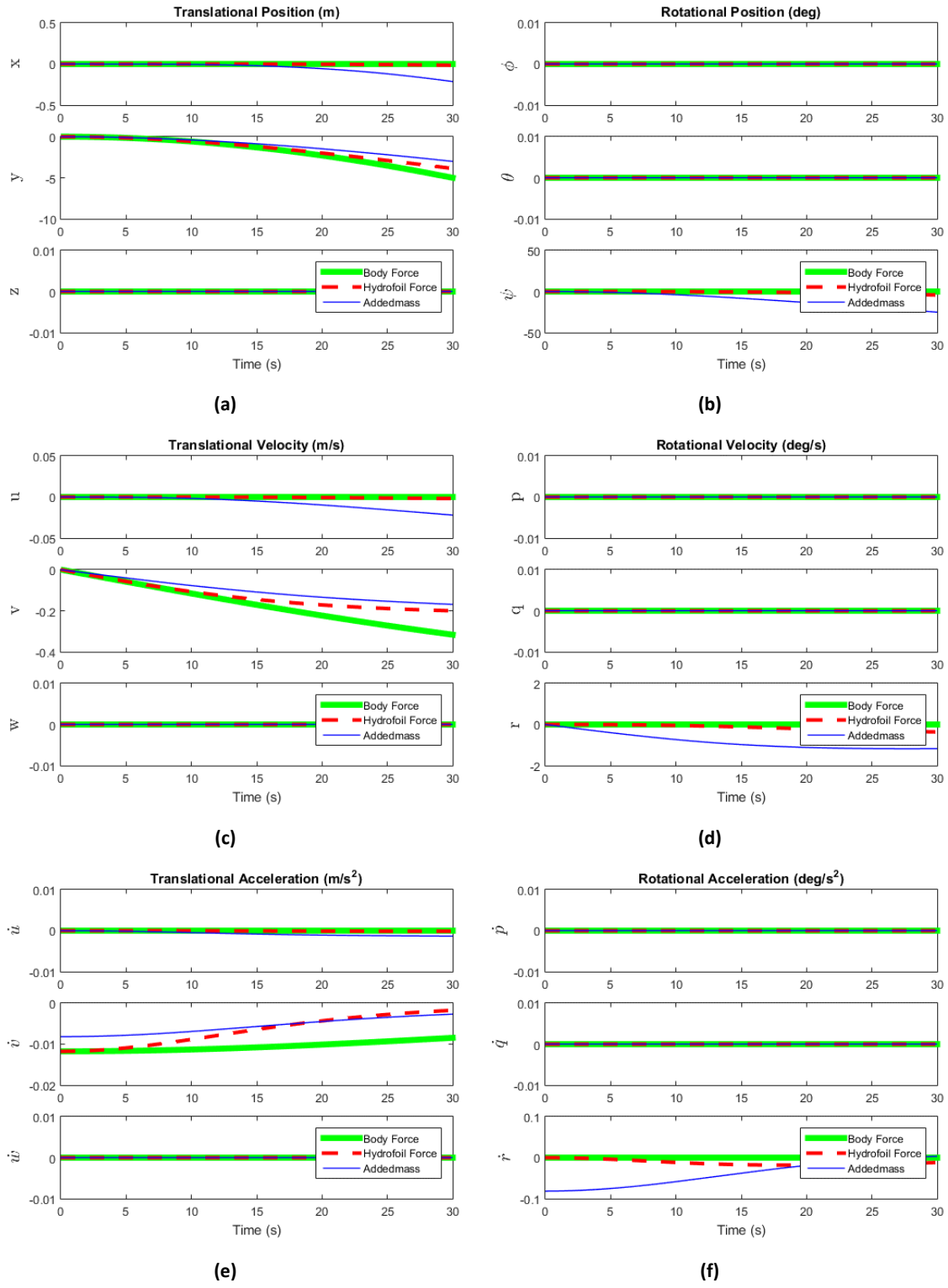


FIGURE A.2 - 6 DOF POSITION, VELOCITY AND ACCELERATION SIMULATION RESPONSE TO 25 N FORCE IN Y DIRECTION

A numeric simulation was performed using Equations (A.1) to (A.4) substituting the $y$ position, velocity $v$, accleration $\dot{v}$ and force $Y$. The results are seen in Table A.2. It can be seen in the table that, as with the x-direction, acceleration $\dot{v}$ and velocity $v$ corresponds closely between both calculations. The position $y$ for the estimate is slightly different from the model due to accumulated error but is still fairly close.

**TABLE A.2 - Y FORCE SIMULATION ESTIMATED VS OBSERVED BODY FORCES**

| | $y$ (m) | $v$ (m/s) | $\dot{v}$ (m/s$^2$) |
|---|---|---|---|
| SIMULINK MODEL | -5.006 | -0.317 | -0.008 |
| ESTIMATE | -5.022 | -0.318 | -0.008 |

## A.3 Force in Z direction

As the configuration of the AUV is similar in the Z direction as in the Y (due to symmetry), the response was observed to correspond; therefore, for brevity these results were omitted.

## A.4 Moment about X axis (roll)

The effect of applying a 10 Nm moment about the X axis can be seen in Figure A.3 with the same layout as seen in the previous sections. From the results it can be seen that motion is only in the applied direction $\phi$ which is to be expected as the sources of drag are symmetric about the X axis.

***Body Force***

With only body-based hydrodynamic forces, the rotational drag is expectedly very low about the X axis as seen by the slow decline in rotational acceleration $\dot{p}$ in Figure A.3 f). As a result, despite the rotational velocity $p$ growing higher in Figure A.3 d), the drag force does not have much effect. This correspondingly results in a very large rotation $\phi$ about the x axis shown in Figure A.3 b).

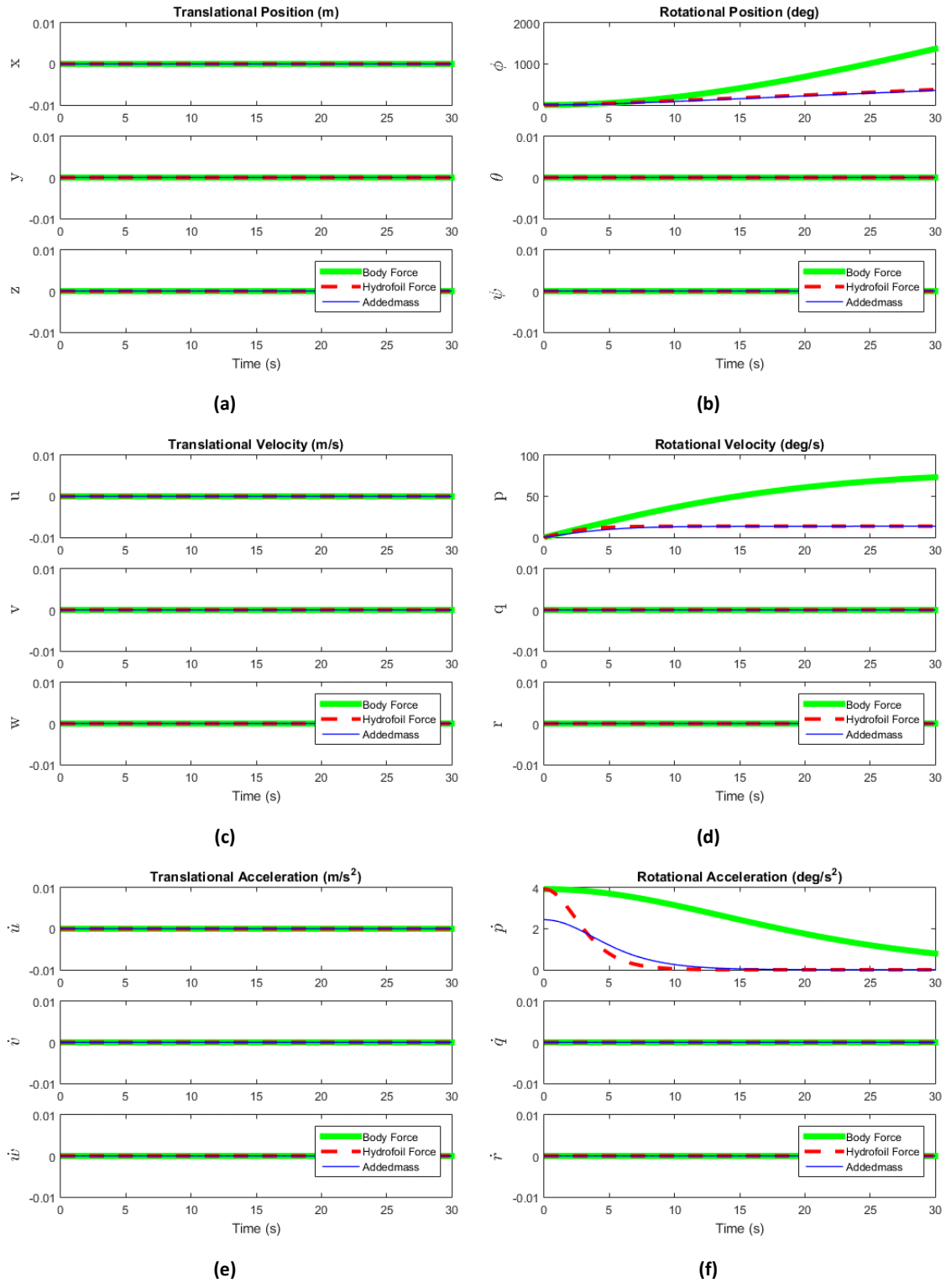


**FIGURE A.3 - 6 DOF POSITION, VELOCITY AND ACCELERATION SIMULATION RESPONSE TO 10 NM TORQUE ABOUT X AXIS (ROLL)**

***Hydroplane Force***

The inclusion of hydroplanes results in a large increase in the rotational drag force in addition to the body forces. As viewable in Figure A.3 e), acceleration decreases rapidly reaching zero in under 10 seconds. The velocity that is reached is much lower than previously in Figure A.3 c) with a correspondingly decreased movement in rotational position $\phi$ as seen in Figure A.3 b).

***Added Mass***

The effect of added mass is visible as a reduction in the initial forward acceleration in Figure A.3 f). This reduced acceleration causes the velocity to take longer to reach its maximum; however, since the same drag force is still in effect the same velocity is ultimately achieved. The corresponding result in rotational position is almost the same as for the hydroplane but at a lower rate due to the longer time required to reach peak velocity.

Similar to the translational motion validation, a simple one dimensional simulation was performed as an estimate for roll rotation. The angle after each time step $\phi_{k+1}$ was calculated using Equation (A.5) by adding the change from the previous angle $\phi_k$ due to the rotational velocity $p_k$ and acceleration $\dot{p}_k$ at the last time step. Similarly the velocity $p_{k+1}$ was calculated using Equation (A.6) from the previous step's rotational velocity and acceleration. The moment $K_{k+1}$ was calculated using Equation (A.8) from the applied moment $K_a$ and the drag moment $K_D$ which, in turn, was calculated from the previous velocity per the drag Equation (2.24). Acceleration was then calculated using Equation (A.7) from the previous moment $K_k$ divided by the moment of inertia $I_x$.

$$\phi_{k+1} = \phi_k + p_k\, T + 0.5\, \dot{p}_k\, T^2 \tag{A.5}$$

$$p_{k+1} = p_k + \dot{p}_k\, T \tag{A.6}$$

$$\dot{p}_{k+1} = \frac{K_k}{I_x} \tag{A.7}$$

$$K_{k+1} = K_a - K_D \tag{A.8}$$

The results of this estimate compared to the model for a moment about X can be seen in Table A.3. From these results it can be seen that the acceleration $\dot{p}$ and velocity $p$ values for both the Simulink model and the analytical estimate correspond well . The angle $\phi$ is slightly less in the estimate than the model which is, again, due to the accumulated error in the one-dimensional estimate.

**TABLE A.3 - MOMENT ABOUT X SIMULATION ESTIMATED VS OBSERVED BODY FORCES**

| | $\phi$ (deg) | $p$ (deg/s) | $\dot{p}$ (deg/s$^2$) |
|---|---|---|---|
| SIMULINK MODEL | 23.888 | 1.279 | 0.014 |
| ESTIMATE | 22.841 | 1.276 | 0.014 |

## A.5 Moment about Y axis (yaw)

The results of applying a 10 Nm moment about the Y axis can be seen in Figure A.4. Unlike with moments about the X axis, the drag forces in this test were unbalanced resulting in motion in the X and Z directions as well as the expected $\theta$ rotation.

***Body Force***

The effect of hydrodynamic forces on the AUV body appear small as indicated from the change in acceleartion $\dot{q}$ in Figure A.4 f). The corresponding velocity seen in Figure A.4 d) increases with a resultant change in angle $\theta$ seen in Figure A.4 a) for the duration of the test.

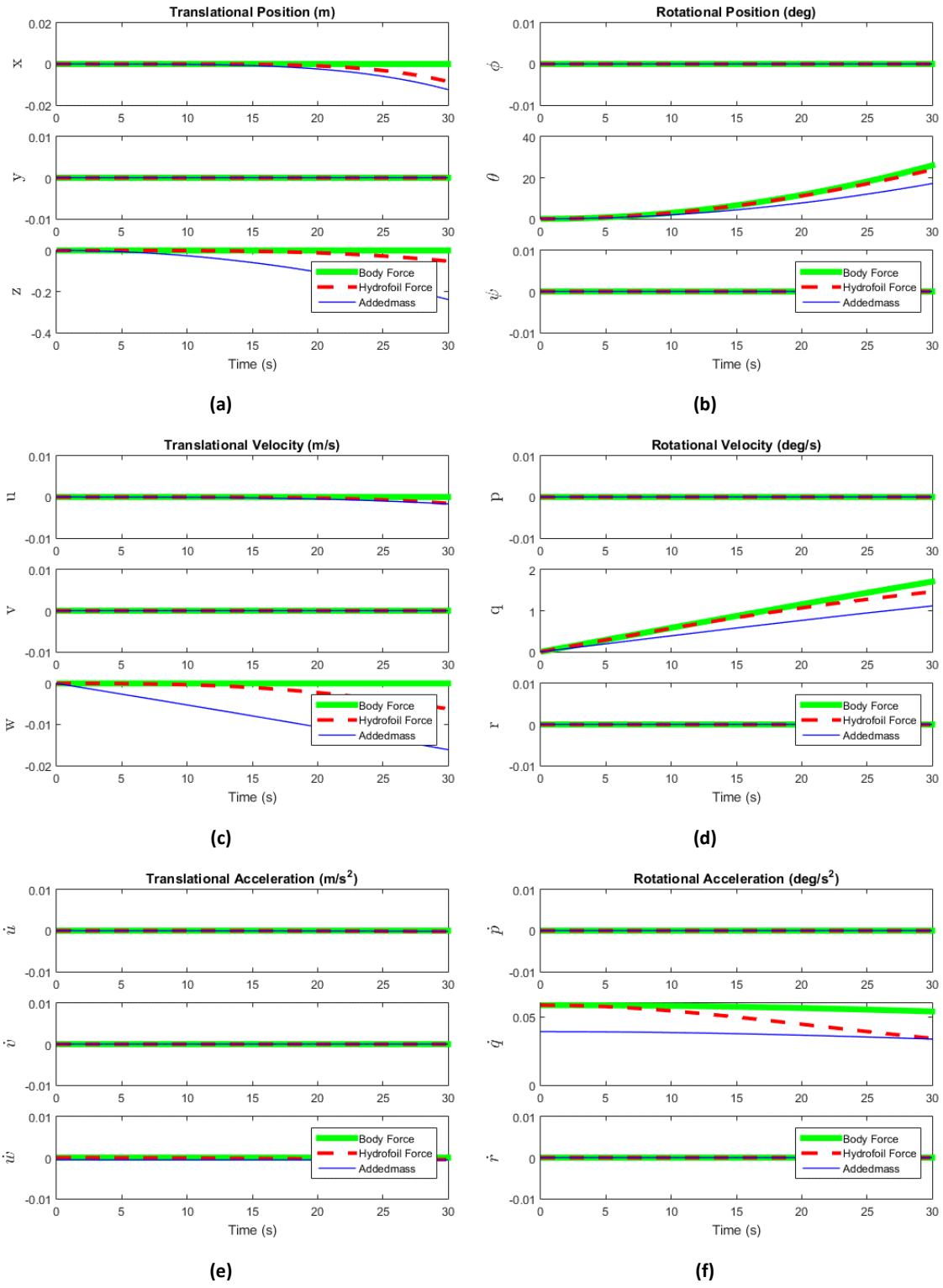


FIGURE A.4 - 6 DOF POSITION, VELOCITY AND ACCELERATION SIMULATION RESPONSE TO 10 NM TORQUE ABOUT Y AXIS (YAW)

***Hydroplane Force***

Including the drag forces from the hydroplanes is seen to cause larger rotational drag reducing acceleration $\dot{q}$ more with increasing velocity $q$. This velocity has a correspondingly lower maximum with a similarly lower change in angle $\theta$ as seen in Figure A.4 b).

In additional to rotation, movement in the X and Z directions due to the coupling of the yaw and sway movements can be seen in Figure A.4 a). The distribution of drag along the length of the AUV is imbalanced with a higher value at the stern due to the presence of the aft hydroplanes. This imbalance along the X axis creates a moment arm which, in turn, causes movement in the body fixed Z direction. Since the AUV is rotating about the Y axis this translation would initially be in the inertial Z direction; however, as rotation $\theta$ increases, motion is seen in the inertial X.

***Added Mass***

Results of including the added mass effects show a smaller initial acceleration $\dot{q}$ with a similar reduction in its magnitude due to the higher moment of inertia. This lower acceleration results in the rotational velocity $q$ and rotation in $\theta$ both being less than previously observed in Figure A.4 d) and b).

Again the effect of motion coupling can be observed between yaw and heave resulting in motion in the X and Z directions. It can be observed in Figure A.4 a) that motion in the Z direction has greatly increased with a small increase in X motion when compared to the previous hydroplane results. The cause of this increase in motion is due to the non-uniform distributiabout Y on of added mass which produces a sway force with the rotation about the Y axis. The bulk of this increased movement is observed in the Z direction due to the rotation θ being less than previous.

Once more a numeric simulation was performed using Equations (A.5) to (A.8) by substituting the angle $\theta$, velocity $p$, accleration $\dot{p}$ and moment $M$. The estimate from

the numeric simulation due to body forces as seen in Table A.4 were again very close to the results from the model.

**TABLE A.4 – MOMENT ABOUT Y SIMULATION ESTIMATED VS OBSERVED BODY FORCES**

| | $\theta$ (deg) | $q$ (deg/s) | $\dot{q}$ (deg/s$^2$) |
|---|---|---|---|
| SIMULINK MODEL | 0.454 | 0.030 | 0.001 |
| ESTIMATE | 0.424 | 0.029 | 0.001 |

## A.6 Moment about Z

The characteristics of the AUV rotating about the Z axis invokes a similar response as about the Y. As such the results have been omitted.

# Appendix B: VBS Model Validation

To ensure the model behaves as intended, individual tests of each of the water and the air modes needed to be performed to validate this model. On the water side this validation meant testing the following functions:

- Positive pumping (into the VBS tank)
- Negative pumping (out of the tank)
- Free filling
- Free emptying

Similarly, the air side needed tests to validate:

- Air Venting
- Air Charging

## B.1 Pump Flow

To validate pump flow, the VBS was tested at low pressure load meaning the outlet of the pump was at the same or lower pressure than the inlet. For positive pumping a low pressure load would mean that the tank pressure $P_a$ is equal or less than seawater pressure $P_{sw}$ with the reverse for negative pumping condition (i.e $P_a \leq P_{sw}$). As the flow rate for the pump was fixed at 5 L/min the expected flow rate, after considering the 80% volumetric efficiency assumption in Equation (4.6), was 4 L/min. The flow observed in the model running at low pressure was 4 liters per minute in both directions of flow.

An example of positive pumping at no pressure load (i.e. $P_a \leq P_{sw}$) can be seen in Figure B.1. This figure shows the volume of water in the VBS tank over a period of one minute and demonstrating the per minute flow rate achieving a final volume of 34 L achieving the expected 4 L change.

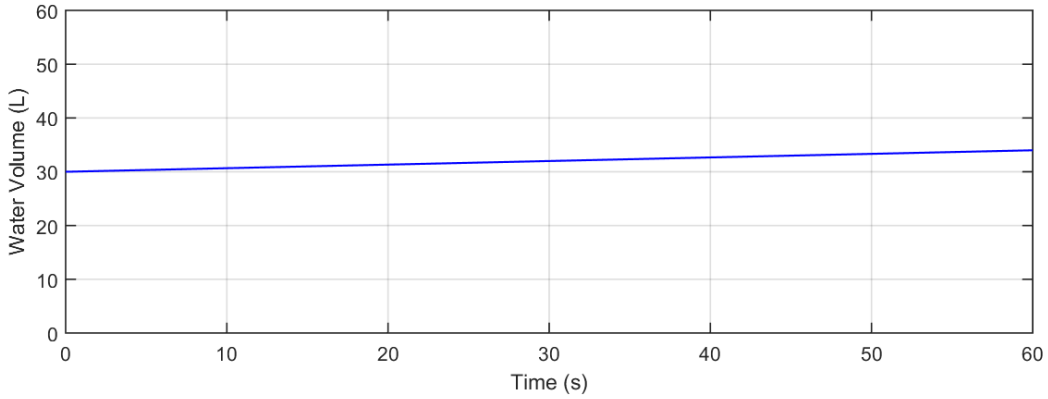


FIGURE B.1 - NO LOAD POSITIVE PUMPING

Similarly, an example of negative pumping is shown in Figure B.2 where, again, there is no pressure load (i.e. $P_{sw} \leq P_a$). Once more the duration is 60 seconds; however, in this case flow is pumped in the opposite direction and, as such, the volume decreases 4 L from 30 L down to the expected 26 L.

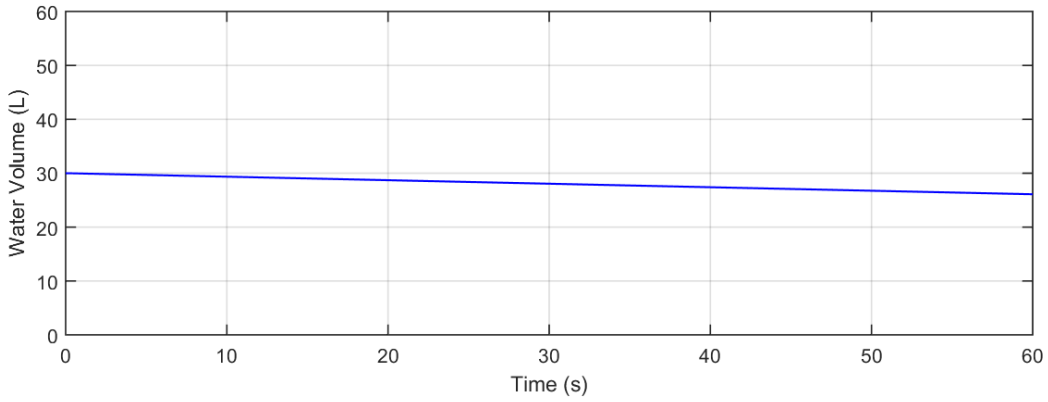


FIGURE B.2 - NO LOAD NEGATIVE PUMPING

Additional tests were performed to observe the effects of increasing the pressure load on the pump. As given in Equation (4.6) increasing the pressure load decreases the volumetric efficiency which, in turn, reduces the change in volume. As expected these tests showed reductions in the change in volume when pumping in both the positive and negative directions.

## B.2 Free Flow

Validating the free flow modes required both the evaluation of the resultant flow of water and the change in pressure as they affect each other, with the flow rates defined for free emptying in Equation (4.14) and for free filling in Equation (4.15). Both these modes result in a change in the volume of water and, consequently , the volume of air; however, the mass of air would be expected to remain constant making it possible to estimate the new pressure $P_2$ from Boyle's Law [21]:

$$P_2 = \frac{P_1 V_1}{V_2} \tag{B.1}$$

where:

$P_1$ = initial pressure

$V_1$ = initial volume

$V_2$ = new volume

The result of a 60 second free emptying test can be seen in Figure B.3. This figure displays the pressures of air $P_a$ and seawater $P_{sw}$ in the top graph and the volume of air $V_a$ in the bottom graph. In this test the initial air pressure $P_a$ was set to 5000 kPa which is approximately 50 atmospheres of pressure, the seawater pressure $P_{sw}$ to 1000 kPa which corresponds to a depth of approximately 100 m and the free flow valve opened. As a result of water flow out of the VBS tank the volume of air increases from the initial 30 L to the final amount of 43.3 L for a total change of 13.3 L. The pressure, likewise, is observed to reduce from 5000 kPa down to 3466 kPa resulting in a pressure change of 1534 kPa. Using Equation (B.1) the final pressure due to the change in volume can be calculated as:

$$P_2 = \frac{P_1 V_1}{V_2} = \frac{5000 \text{ kPa} \times 30 \text{ L}}{43.3 \text{ L}} = 3464.2 \text{ kPa}. \tag{B.2}$$

The analytical results from Equation (B.2) closely resembles that of the numeric simulation with only a small difference observed.

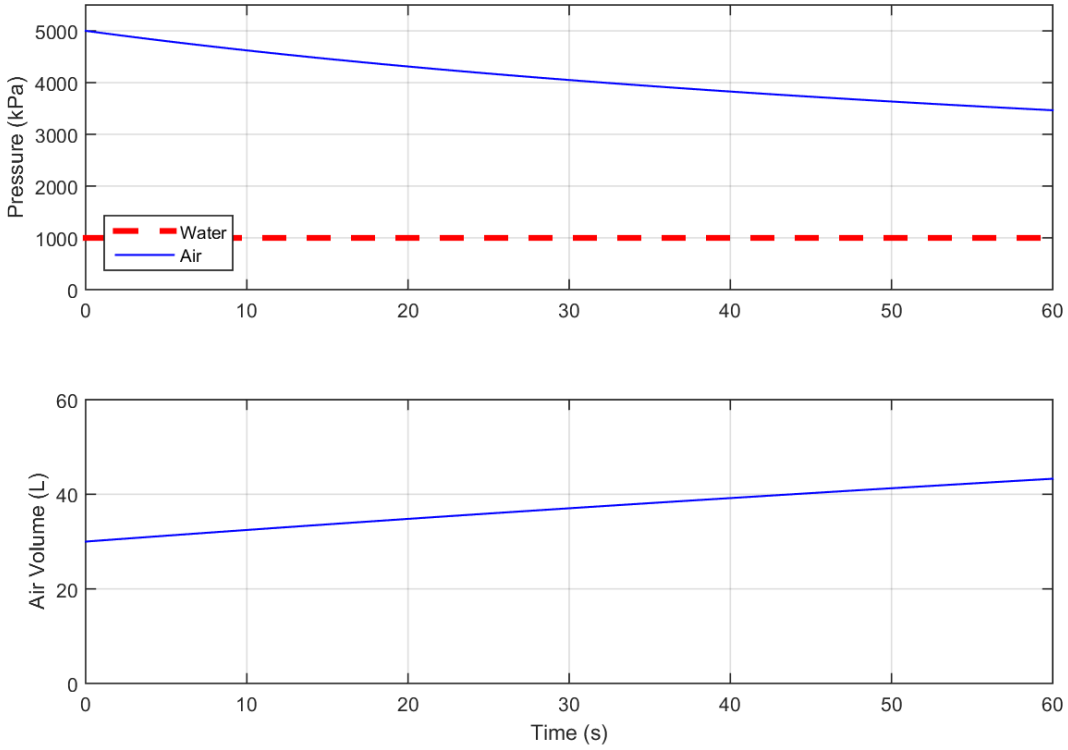


FIGURE B.3 - FREE EMPTY AT Δ P = 4000 KPA

Figure B.4 shows the results of free filling where the initial conditions are the air pressure set to 1000 kPa and the water pressure at 5000 kPa, thus reversing the two pressures from the previous free emptying example. In this case the flow of water causes the volume of air to decrease from 30 L down to 15.6 L for a change of 14.4 L. With this change there is a corresponding increase in pressure $P_a$ of 923 kPa from 1000 kPa to the final value of 1923 kPa. The resultant pressure once more can be calculated from the new volume using Equation (B.1) to give:

$$P_2 = \frac{1000\ \text{kPa} \times 30\ \text{L}}{14.4\ \text{L}} = 1923\ \text{kPa}. \tag{B.3}$$

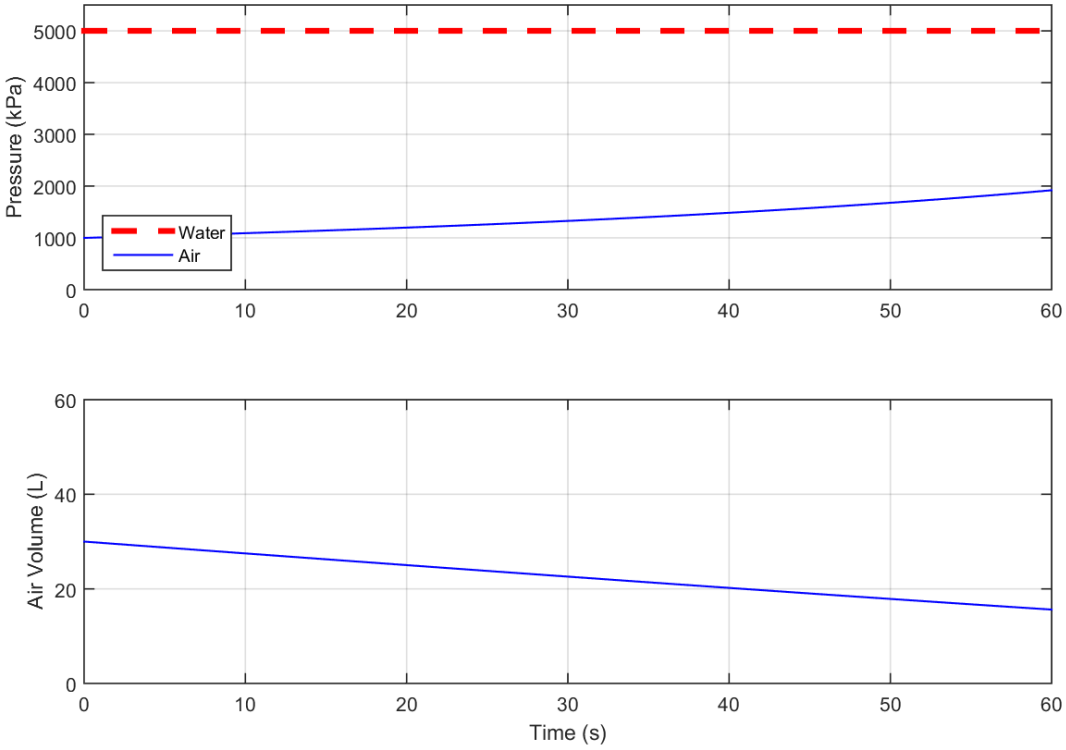


FIGURE B.4 - FREE FILL AT Δ P = 4000 KPA

Both tests seen in Figure B.3 and Figure B.4 appear to closely resemble a linear result making it possible to check them against a constant flow rate. Since they both start with the same difference in pressure of 4000 kPa between the tank $P_a$ and the seawater pressure $P_{sw}$, it is then possible to calculate the initial magnitude of both flow rates using Equation (4.11). Assuming the water density ρ to be 1022.7 kg/m$^3$ and using the values from Table 4.1, this flow rate can be calculated as:

$$Q = 0.6\,(1.5 \times 10^{-4}\ \mathrm{m}^2)\sqrt{2\,\frac{4000\ \mathrm{kPa}}{1022.7\ \mathrm{kg/m}^2}} \tag{B.4}$$

$$Q = 2.52 \times 10^{-4}\ \mathrm{m}^3/\mathrm{s}. \tag{B.5}$$

If maintained over 60 seconds this flow rate would result in an air volume change of 15.1 L. A comparison between this constant flow result and those of the free empty and free fill results can be seen in Table B.1. In this table the largest observed change is with

the constant flow condition which was expected as the other flow conditions were reduced by pressure changes. It can also be seen that the free fill mode results in a larger difference in volume (14.4 L) versus the free empty result of 13.3 L. This difference is due to the free empty condition having a quicker decline in pressure ending with a change of 1534 kPa which is considerably larger than the free fill change in pressure of 923 kPa. As a result of the larger pressure change the flow is reduced more for the free empty case thus explaining the different value in Table B.1.

**TABLE B.1 - FREE FLOW VS CONSTANT RATE VOLUME CHANGE COMPARISON**

| | ABSOLUTE CHANGE IN WATER VOLUME (L) |
|---|---|
| **CONSTANT FLOW** | 15.1 |
| **FREE EMPTY** | 13.3 |
| **FREE FILL** | 14.4 |

If depth were increased there would be a corresponding increase in water pressure resulting in a smaller pressure difference in the free empty test lowering the flow rate. However, for the presented free fill rate this would increase the pressure difference and hence flow rate. Conversely, for shallower depth the free empty would increase flow and the free fill would see a decrease in the flow rate.

## B.3 Air side flow

The air side modes deal with changes in mass in one or both of the charge tank and the VBS tank. Equation (4.16) determines the flow rate out of the charge tank $\dot{m}_c$ with the rate venting out of the VBS tank $\dot{m}_v$ given by Equation (4.17). Since the volume remains constant for both these modes the new pressure $P_2$ can be calculated using Avogadro's law [21] as:

$$P_2 = P_1 \frac{m_2}{m_1}. \tag{B.6}$$

Figure B.5 shows an example of the venting mode where the internal air pressure $P_a$ is initially 5000 kPa and water pressure $P_{sw}$ is 1000 kPa. This figures shows both the air pressure $P_a$ and the seawater pressure $P_{sw}$ in the upper graph with the air mass $m_a$ in the lower graph. The result of this test show the mass of air in the VBS tank $m_a$ decreasing nonlinearly from 1.784 kg down to 0.517 kg. A corresponding change in pressure $P_a$ decreases from the initial 5000 kPa down to 1448.4 kPa.

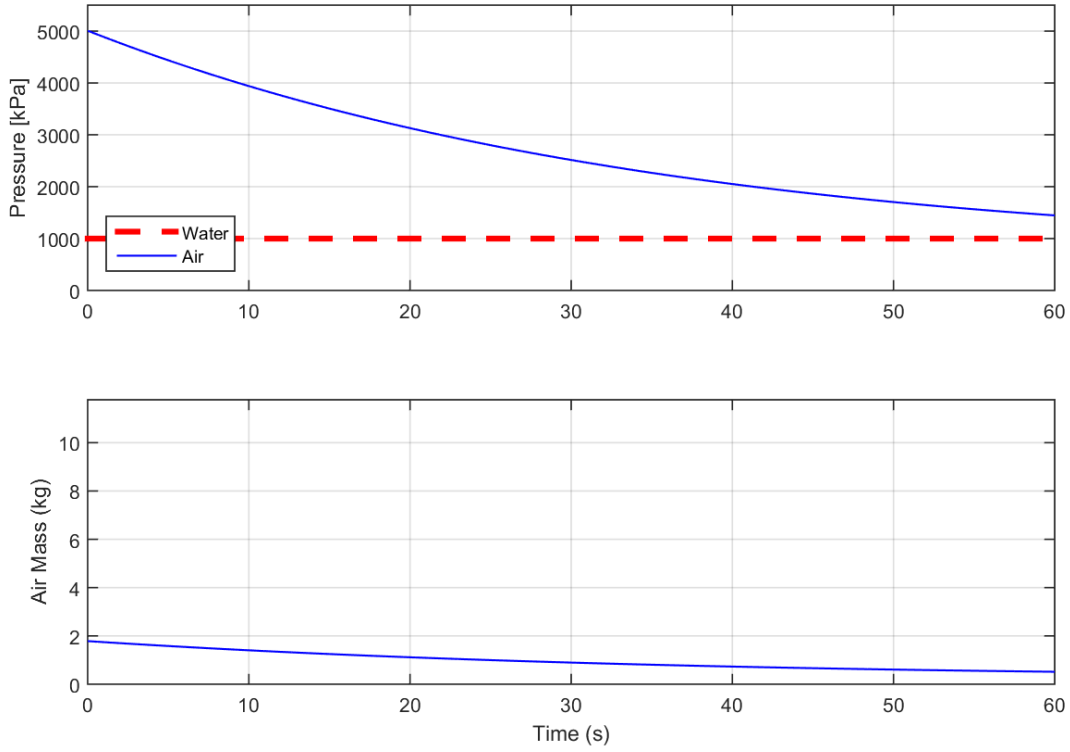


**FIGURE B.5 - TANK AIR VENTING SIMULATION**

Since the flow rate observed is non-linear, a constant rate cannot be used to estimate the result. As such a numeric simulation was performed using a 1 second time step T and estimating the mass flow rate from Equation (4.17) given as:

$$\dot{m}_{a_{k+1}} = CYA_2\sqrt{2\,\rho_{a_k}(P_{a_k} - P_w)} \tag{B.7}$$

where the values of $C$, $Y$ and $A_2$ are those given in Table 4.1 and subscript $k$ refers to the current step time value, while subscript $k+1$ refers to that of the next time step. Since the mass is flowing out of the VBS tank it would then be given as:

$$m_{a_{k+1}} = m_{a_k} - \dot{m}_{a_k} T \tag{B.8}$$

and density given as:

$$\rho_{a_{k+1}} = m_{a_k}/V_a. \tag{B.9}$$

Finally, using Equation (B.6) pressure can be calculated as:

$$P_{a_{k+1}} = \frac{m_{a_{k+1}}}{m_{a_k}} P_{a_k}. \tag{B.10}$$

The result of this estimate is compared to that of the VBS model in Table B.2. It can be seen that the results closely resemble each other with the pressure being slightly off. This difference can be accounted for due to accumulated error in the numeric estimate.

**TABLE B.2 - VENTING MODE MODEL VS ESTIMATE RESULTS**

| | PRESSURE (kPa) | AIR MASS (kg) |
|---|---|---|
| **MODEL** | 1448.4 | 0.517 |
| **ESTIMATE** | 1450.0 | 0.517 |

Charging mode is similar to venting; however, in this case the mass loss $\dot{m}_c$ in the charge tank is added to the mass in the VBS tank $m_a$ also increasing the pressure $P_a$. The results of this test can be seen in Figure B.6 where both the pressures and masses of air converge around 26 seconds. Compared to venting in Figure B.5, achieving equilibrium is much faster due to the pressure at the destination $P_a$ increasing as the source $P_c$ decreases. This symbiotic change is the result of the mass transferring from the charge tank and into the VBS tank causing their respective pressures to similarly adjust.

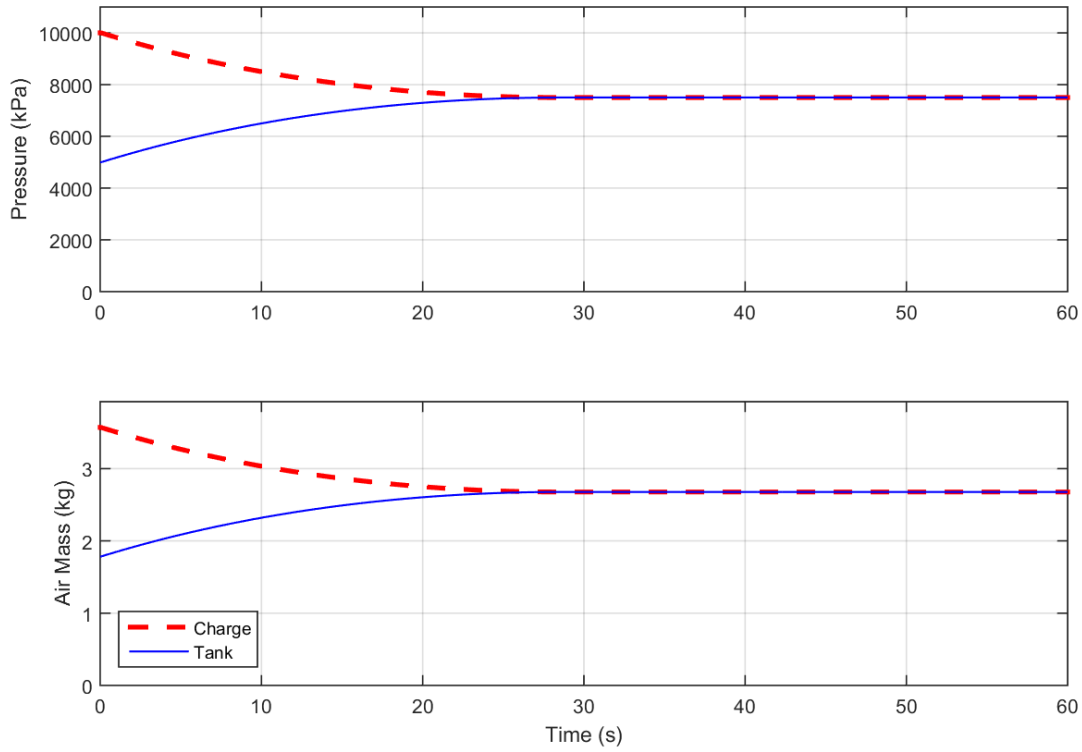


FIGURE B.6 - TANK AIR CHARGING SIMULATION

Once more the results cannot be easily estimated so a numeric simulation is performed first using Equation (4.17) to give the mass flow as:

$$\dot{m}_{c_{k+1}} = CYA_2\sqrt{2\,\rho_{c_k}(P_{c_k} - P_w)}. \tag{B.11}$$

Since mass travels from the charge tank to the VBS tank these two mass values are given as:

$$m_{c_{k+1}} = m_{c_k} - \dot{m}_{c_k}\,T \tag{B.12}$$

$$m_{a_{k+1}} = m_{a_k} + \dot{m}_{c_k}T \tag{B.13}$$

with charge air density given as:

$$\rho_{c_{k+1}} = m_{c_k}/V_a \tag{B.14}$$

Finally, the pressure in the VBS tank given from (B.10) and the pressure in the charge tank as:

$$P_{c_{k+1}} = \frac{m_{c_{k+1}}}{m_{c_k}} P_{a_k}. \quad \text{(B.15)}$$

The results of this numerical estimate are compared to that of the model in Table B.3 which are seen to be in close agreement.

**TABLE B.3 - CHARGE MODE MODEL VS ESTIMATE RESULTS**

| | PRESSURE $P_C$ (kPa) | AIR MASS $m_c$ (kg) |
|---|---|---|
| **MODEL** | 7501.8 | 2.68 |
| **ESTIMATE** | 7501.2 | 2.68 |

With all the air and water modes validated it is now possible to use the model with confidence.